Universität Potsdam

Doctoral Thesis

VERITAS Dark Matter search in dwarf spheroidal galaxies: an extended analysis

Author:
Chiara Giuri

Supervisors:
Dr. Elisa Pueschel
Prof. Dr. Martin Pohl
Dr. Donggeun Tak

A thesis submitted in fulfillment of the requirements
for the degree of "Doctor rerum naturalium" (Dr. rer. nat.)

in the scientific discipline "Astroparticle Physics"

Institut für Physik und Astronomie
Mathematisch-naturwissenschaftliche Fakultät

May 17, 2022

Published online on the
Publication Server of the University of Potsdam:
https://doi.org/10.25932/publishup-57586
https://nbn-resolving.org/urn:nbn:de:kobv:517-opus4-575869

Declaration of Authorship

I, Chiara Giuri, declare that this thesis titled, "VERITAS Dark Matter search in dwarf spheroidal galaxies: an extended analysis" and the work presented in it are my own. I confirm that:

- This work was done wholly or mainly while in candidature for a research degree at this University.
- Where any part of this thesis has previously been submitted for a degree or any other qualification at this University or any other institution, this has been clearly stated.
- Where I have consulted the published work of others, this is always clearly attributed.
- Where I have quoted from the work of others, the source is always given. With the exception of such quotations, this thesis is entirely my own work.
- I have acknowledged all main sources of help.
- Where the thesis is based on work done by myself jointly with others, I have made clear exactly what was done by others and what I have contributed myself.

Signed:

_____

Date:

_____

"*I knew exactly what to do. But in a much more real sense, I had no idea what to do.*"

M. Scott

UNIVERSITÄT POTSDAM

Abstract

Institut für Physik und Astronomie

Mathematisch-naturwissenschaftliche Fakultät

"Doctor rerum naturalium" (Dr. rer. nat.)

VERITAS Dark Matter search in dwarf spheroidal galaxies: an extended analysis

by Chiara Giuri

In the last century, several astronomical measurements have supported that a significant percentage (about 22%) of the total mass of the Universe, on galactic and extragalactic scales, is composed of a mysterious "dark" matter (DM). DM does not interact with the electromagnetic force; in other words it does not reflect, absorb or emit light. It is possible that DM particles are weakly interacting massive particles (WIMPs) that can annihilate (or decay) into Standard Model (SM) particles, and modern very-high-energy (VHE; > 100 GeV) instruments such as imaging atmospheric Cherenkov telescopes (IACTs) can play an important role in constraining the main properties of such DM particles, by detecting these products. One of the most privileged targets where to look for DM signal are dwarf spheroidal galaxies (dSphs), as they are expected to be high DM-dominated objects with a clean, gas-free environment. Some dSphs could be considered as extended sources, considering the angular resolution of IACTs; their angular resolution is adequate to detect extended emission from dSphs. For this reason, we performed an extended-source analysis, by taking into account in the unbinned maximum likelihood estimation both the energy and the angular extension dependency of observed events. The goal was to set more constrained upper limits on the velocity-averaged cross-section annihilation of WIMPs with VERITAS data. VERITAS is an array of four IACTs, able to detect γ-ray photons ranging between 100 GeV and 30 TeV. The results of this extended analysis were compared against the traditional spectral analysis. We found that a 2D analysis may lead to more constrained results, depending on the DM mass, channel, and source. Moreover, in this thesis, the results of a multi-instrument project are presented too. Its goal was to combine already published 20 dSphs data from five different experiments, such as Fermi-LAT, MAGIC, H.E.S.S., VERITAS and HAWC, in order to set upper limits on the WIMP annihilation cross-section in the widest mass range ever reported.

Kurzfassung

Im letzten Jahrhundert haben verschiedene mehrere astronomische Messungen gezeigt, dass ein erheblicher Prozentsatz (etwa 22 %) der Gesamtmasse des Universums auf galaktischer und extragalaktischer Ebene aus einer geheimnisvollen "dunklen" Materie (DM) besteht. DM interagiert nicht mit der elektromagnetischen Kraft und reflektiert, absorbiert oder emittiert daher kein Licht. Es ist möglich, dass es sich bei DM-Teilchen um schwach wechselwirkende massive Teilchen (engl. weakly interacting massive particles, WIMPs) handelt, die in Teilchen des Standardmodells (SM) annihilieren (oder zerfallen) können. Indem sie diese Produkte nachweisen, können moderne Detektoren für sehr hoch energetische (engl. very-high-energy, VHE; 100 GeV) Gammastrahlung, wie zum Beispiel bildgebende atmosphärische Cherenkov-Teleskope (engl. imaging atmospheric Cherenkov telescopes, IACTs), eine wichtige Rolle bei der Bestimmung der Haupteigenschaften solcher DM-Teilchen spielen. Eines der am besten geeignetsten Ziele für die Suche nach DM-Signalen sind sphäroidische Zwerggalaxien (engl. dwarf spheroidal galaxies, dSphs), da diese stark DM-dominierte Objekte mit einer gasfreien Umgebung sind. Die Winkelauflösung von IACTs ist ausreichend, um ausgedehnte Emission von dSphs zu entdecken. Aus diesem Grund haben wir eine Analyse dieser Quellen durchgeführt, indem wir in der unbinned Maximum-Likelihood-Schätzung sowohl die Energie als auch die Abhängigkeit der Winkelausdehnung der beobachteten Gammastrahlung berücksichtigt haben. Das Ziel war es, mit Hilfe der VERITAS-Daten genauere Obergrenzen für den geschwindigkeitsgemittelten Annihilationsquerschnitt von WIMPs zu bestimmen. VERITAS ist eine Anordnung von vier IACTs, die Gammastrahlen im Bereich von 100 GeV bis 30 TeV detektieren können. Die Ergebnisse dieser erweiterten Analyse wurden mit der traditionellen Spektralanalyse verglichen. Es zeigte sich, dass je nach DM-Masse, Kanal und Quelle eine 2D-Analyse zu

aussagekräftigeren Ergebnissen führen kann. Darüber hinaus werden in dieser Arbeit auch die Ergebnisse eines Multi-Instrumenten-Projekts vorgestellt. Das Ziel war es, die bereits veröffentlichte 20 dSphs-Datensätze von Fermi-LAT, MAGIC, H.E.S.S., VERITAS und HAWC zu kombinieren, um obere Grenzwerte für den WIMP-Annihilationsquerschnitt im breitesten jemals veröffentlichten Massenbereich zu bestimmen.

Contents

List of Figures

List of Tables

Chapter 1

Introduction

One of the most fascinating - yet still open - challenges that astrophysicists have been facing for years now is the so-called "Dark Matter question". Dark matter (DM) is believed to constitute an important portion of the matter content of the Universe. In the past decades, there have been different observational evidences supporting that there must be a sort of invisible matter, interacting gravitationally but not electromagnetically, filling in the Universe. Invisible, because it has not been directly detected, so far. We do not even know what the DM is, what particles it is made of, what its properties are, even if we could actually directly detect it. The goal of this thesis is to shed some more light on these thrilling open questions. Astronomical observations can be used to search for DM annihilation or decay products, complementing direct and collider-based searches. For this work, we assumed that DM is composed by Weakly Interacting Massive Particles (WIMPs), which are attractive candidates to explain DM composition. If they exist, their decay or annihilation could generate secondary particles including very-high-energy (VHE: $E > 100$ GeV) γ rays, which could be detected by imaging atmospheric Cherenkov telescopes (IACTs), such as the Very Energetic Radiation Imaging Telescope Array System (VERITAS). It is an array of

four imaging atmospheric Cherenkov telescopes, located in Southern Arizona and sensitive to VHE γ-rays in the 100 GeV - 30 TeV energy range.

One of the most promising targets for DM searches are dwarf spheroidal galaxies (dSphs). Indeed, they are expected to be highly dark matter-dominated objects with a negligible predicted γ-ray emission due to apparent absence of gas and on-going star formation. They are also located at high Galactic latitudes, meaning that no foreground contamination is expected to affect any γ-ray signal coming from them. For this thesis work, we analysed VERITAS data from four dSphs, i.e. Bootes, Draco, Segue1 and Ursa Minor.

IACTs, whose point spread functions (PSFs, defined as 68% containment radius) are typically 0.1° at 1 TeV, have the necessary angular resolution to detect extended emission from some dSphs. Thus, the main goal of this thesis was to perform an extended-source analysis, which can give an improvement to DM sensitivity, compared to a point-source analysis. For this purpose, we tested the effectiveness of performing a maximum likelihood estimation (MLE) analysis incorporating the dSph angular profiles of four dSphs, against the traditional spectral analysis. We used dSphs data collected between 2007 and 2013 (i.e. only already published data were used in this work) to perform an unbinned MLE that contained the angular extension of the four dSphs. No DM signal was detected, thus we put constraints on the annihilation cross-section of DM particles.

As sub-project to the thesis work, I also contributed to a multi-instrument project for performing a joint analysis of set of 20 dSphs. This project included contributions from five different collaborations, i.e. Fermi, MAGIC, H.E.S.S., VERITAS and HAWC. Our goal was to share the already published dSphs data from each collaboration and combine them, for the first time together, in order to set upper limits within the widest mass range ever

considered, i.e. from 5 GeV to 100 TeV. Each collaboration analysed its own dataset, keeping its instruments response functions (IRFs) and analysis reconstruction softwares, but at the same time we used the same J-factor calculations and γ-ray spectra. The preliminary results shown in this thesis demonstrate that the combined limits are 2-3 times more constraining than the limits obtained by the individual instruments.

Chapter 2

The Dark Matter

The Dark Matter (DM) question is still one of the greatest unsolved questions of astronomy. As matter of fact, it can be proved that DM constitutes about the 22% of the mass of the Universe and about the 85% of the total matter content of the Universe. Despite its large portion, its nature and properties are still under investigation.
In this chapter, in Sec. 2.1, we are going to briefly talk about the history of DM and its evidences; Sec. 2.2 will cover the cosmological Standard Model (SM) and its implications, which explain the theoretical grounds of DM and its formation and evolution. In Sec. 2.3, we will see what are the main DM candidates; in Sec. 2.4 we are going to treat the different types of DM searches performed; finally, Sec. 2.5 will inspect the most promising targets where to look for DM.

2.1 Historical notes and observational evidences of DM

One of the biggest - yet still unresolved - astrophysical revelations of the 20th century is that the ordinary baryonic matter, i.e. the one formed by neutrons and protons, is, surprisingly, not the dominant component in the Universe total mass. In fact, it can be proven that

there is a "new" and invisible component that fills the Universe. This mysterious constituent is more or less five times more abundant than the ordinary matter, which the Universe is made of. Astronomers and physicists have called this strange type of matter "Dark Matter". Several cosmological observations have shown, by now, that visible matter is made up of just $\sim 4\%$ of the total mass of the Universe, while $\sim 74\%$ is made up of the so-called Dark Energy (DE), and about $\sim 22\%$ is made up of DM (see Fig. 2.1).

Figure 2.1: Total matter-energy components of the Universe. These values are obtained in an analysis of the fluctuations in the spectrum of the Cosmic Microwave Background radiation. *Image credit*: NASA / WMAP Science Team

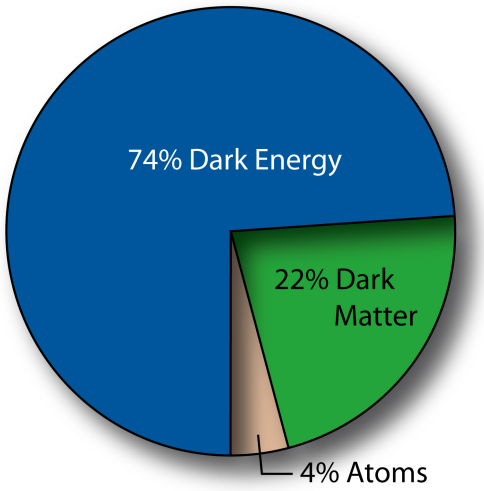

But the history of DM search starts long time ago.

As a matter of fact, astronomers have observed the Universe for centuries through the light produced by astronomical sources, such as stars or galaxies of various types. Our

understanding of the Universe, therefore, comes from photons that can be detected[1]. For years, photometry has been used by astronomers to estimate the amount of mass. In fact, by evaluating the light coming from objects like galaxies as well as galaxy clusters, it is possible to infer their mass by using well defined M/L ratios [1].

It was in 1930 that J.H. Oort studied the Doppler shifts of the stars in the Milky Way moving near the galactic plane. He calculated their velocities and he found that there was a sort of excess of mass, about three times higher than the bright mass, preventing those stars from moving away from the center. In the same year, the astronomer K. Lundmark [2] and three years later F. Zwicky [3] discovered that a large part of matter does not emit or absorb light, so it can only be observed by its gravitational interaction. Thus, many scientists started to speak for the first time about the so-called "missing mass" question, i.e. there was a need for more mass than observed to understand the dynamics of stars and galaxies. This mass was called "Dark Matter".

In 1933 Zwicky, for the first time, measured the velocity dispersion of individual galaxies in one of the largest galaxy clusters known, i.e. the Coma Cluster [3]. Let's remind that galaxy clusters are composed by hundreds to thousands of galaxies bound together by gravity, with a mass range of 10^{14} to $10^{15} M_{\odot}$, which makes them the largest gravitationally bound objects in the Universe. Thus, he demonstrated that there was an evidence of an invisible mass on extragalactic scales. By using the viral theorem[2], he found that the gravitational potential was not sufficient to explain the rotational curves for multiple galaxies within the galaxy cluster. In fact, he concluded that the total measured mass values were 400 times

[1] Of course, it must be mentioned that nowadays we reached a state such that we can learn about Universe from Neutrinos and Gravitational Waves as well.

[2] In mechanics, the virial theorem links the total kinetic energy T of a stable system of discrete particles, bound by potential forces, to the total potential energy U of the system. The relation is the following: $T = -1/2U$.

higher than the mass estimated by the luminosity of the galaxies. In other words, their mass-to-light ratios were much higher than expected. Consequently, in 1937 Zwicky, in his well-known article on galaxy clusters [4], stated again that:

> *It is not possible to derive the masses of [galaxies] from observed rotations, without the use of additional information.*

It would be worth mentioning, also, that subsequent measurements showed that DM can make up to 85% of the total mass of the Coma Cluster; about 2% is contained in galaxies and about $\sim 12\%$ in gas. Since the Coma Cluster contains a significant amount of hot, X-ray, intergalactic gas [5], this does not contradict what Zwicky found out, i.e. that most of the mass in galaxies is dark [6]. Similar conclusions have been reached from studies on other clusters later on.

DM evidences were also claimed at galactic scales few years later. In fact, in 1939, in his PhD work [7], H. Babcock presented the rotation curve of M31 up to 20 kpc from its center. It revealed that the outer parts of the disk were moving at a higher velocity than expected, staying stable for a large range of r [8] (see Fig. 2.2).

Figure 2.2: Rotation curve for M31 from [9]. The solid line is the best fit to the data. Each mass component is identified.

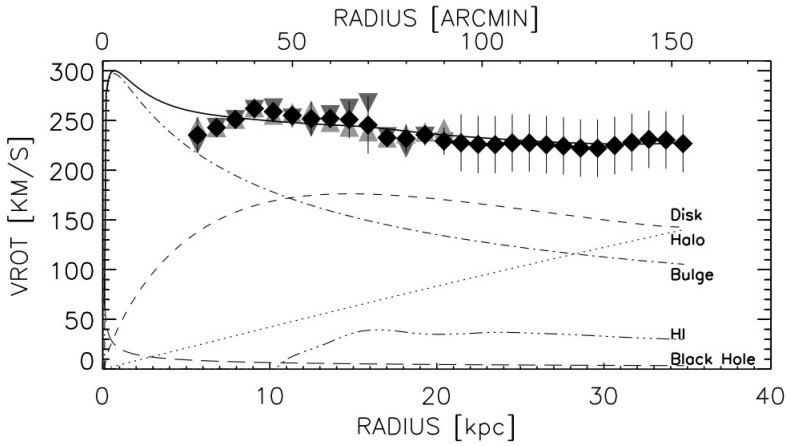

This was completely contradictory to the so-called "Keplerian fall", where visible matter is expected to show a downward rotational curve; i.e. the velocity v of matter behaves like:

$$v \propto 1/\sqrt{r}, \tag{2.1}$$

deduced by taking the balance between gravitational and centrifugal forces into consideration. Subsequently, more than a thousand rotation curves of spiral galaxies have been observed until today, and all of them have shown such a flattening in their peripheral areas. The same behavior has been as well observed 40 years later for other galaxy types (including the MW) [10], regardless of their morphology (spiral or elliptical) or their size.
Thus, under the simplifying assumption that it is possible to estimate the mass distribution of galaxies by using their rotation curves, one can conclude that the observed and

theoretical curves agree well with each other only if an additional "invisible" mass budget is introduced to the baryonic disk mass [11]. This unknown component must be a halo composed of dark matter, with mass $M \propto r$ and density $\rho \propto 1/r^2$ [12]. Even though there is quite a consensus about the shape of DM halos at large distances from the center of galaxies, literature is still not quite on agreement about whether the DM profile is more cuspy rather than shallow in galaxies innermost regions [13].

In the 1970s, another method to prove the existence of the DM and to measure its content and distribution, besides dynamical measurements, was tested, i.e. the gravitational lensing. It is, even nowadays, one of the most effective methods for mapping large-scale DM distributions [14, 15]. Essentially, light coming from a background source and passing by a massive and/or dense body is deflected by this one behaving as a gravitational lens (due to space-time curvature). It results to a multiplication of the source image for the observer [16]. If the source of the background is exactly behind a gravitating spherical mass, the so called "Einstein's ring" [17] would appear as the light passes around the mass (see Fig. 2.3), with its radius being proportional to the square root of the projected mass within it.

Figure 2.3: Left: Einstein's ring induced by the luminous red galaxy LRG 3-757. Right: galaxy cluster CL0024+1654 from the Hubble Space Telescope taken in November 2004. Images by: ESA/Hubble & NASA, H. Lee & H. Ford (Johns Hopkins U.)

In any other scenario, i.e. if the source is slightly offset from the objector or the lens has a specific shape, the source of the background appears at multiple positions.
The strength of gravitational lensing can be classified into strong, weak and micro, depending on the power of the deflection. In strong lensing [18], a huge mass acts as lens and the observer can see two (or even more) distinct images of the source. This can be used to map the mass distribution in the core regions of galaxy clusters and also, sometimes, large single galaxies. In weak lensing [19], the source image is mildly distorted, smearing into an arc centred on the centre of the lens, generally constituted by a huge mass. This is known as "shear effect". Weak gravitational lensing has provided some of the strongest evidences for DM and it can be used to map the mass distribution throughout galaxy clusters. The case of cluster 1E0657-56, known as "Bullet Cluster" [20, 21] (showed in Fig. 2.4) is one of the most famous evidences claiming for the DM existence [22].

Figure 2.4: An image of the Bullet Cluster, seen by the Hubble and Magellan optical telescopes. Credit: X-ray: NASA/CXC/CfA/.

This cluster is known to emerge from the merging of two sub-clusters, in which the different components (gas, stars and DM) behave - and interact - differently. In fact, the stars (observable in visible light) are not greatly affected by the collision and they just passed through, gravitationally slowed. On the other hand, hot gas clouds from both merging parts (observable by X-ray emission), containing most of the baryonic matter, interact electromagnetically, they lose momentum and slow down much more than the stars. However, weak lensing observations, by mapping the mass potential, showed that the center of the total mass distribution does not overlap with the gas cloud, i.e. the center of the total mass was moved from that of the visible baryonic part of the cluster (due to

the collisionless nature of DM). This indicates that the major component of the mass in these clusters is non-baryonic and not luminous, i.e. it is made of a "dark matter". It also should be collisionless and with a small self-interaction cross-section. In microlensing, the lens is a small mass (usually a star or a planet). Source, lens and observer are positioned in a straight line. However, the distortion and multiple images caused by lensing cannot be individually resolved. It can be mainly used to detect exoplanets, to study the binary star population and the structure of the disk of the Milky Way, to measure the stellar rotation and to probe quasars.

To conclude, we can say that a multitude of different observations on various cosmological scales have been made today, and all of them support the existence of such DM.

2.2 The Standard Model of Cosmology

In order to better understand what could be the DM nature, how its particle[3] could have been created and evolved by time and its main properties, at this point it may be important to give a brief review, showing also its strengths as well as its inconsistencies, of the most prevailing model explaining the evolution of the Universe, i.e. the *Standard Model of Cosmology* or *Hot Big Bang Model* (or ΛCDM). It gives a satisfactory explanation of existence of the observed Universe, from its origin about 13.7 billion years ago, when it was extremely hot and dense. It describes how it later on evolved and expanded (cooling down), how the light elements formed, how the relic background radiation and the large scale structures that we observe were generated.

The *Hot Big Bang Model* considers that, at the early stage, the Universe was as a very

[3] Assuming DM is composed by particles.

hot and dense plasma system that emerged from a highly compressed state that existed, around 10^{10} years ago. In order to describe its state, the equations of General Relativity can be used. They were introduced by A. Einstein in 1915 and published in 1916 [23] in order to explain the geometry of the Universe. They link the energy content of the Universe with its matter content. To solve them, the Friedmann-Lemaitre-Robertson-Walker (FLRW) metric [24] is also applied, assuming that the Universe is isotropic, homogeneous and (exponentially) expanding ("inflationary state") [25].

Thus, the Friedmann's equations, which model the expansion of the Universe, can be obtained [26]:

$$\left(\frac{\dot{a}}{a}\right) + \frac{k}{a^2} = \frac{8\pi G}{3}\rho, \tag{2.2}$$

and

$$\frac{\ddot{a}}{a} = -\frac{4\pi G}{3}\left(\rho + \frac{3p}{c^2}\right) + \frac{\Lambda c^2}{3}, \tag{2.3}$$

where a(t) is the so called "scale factor" (which gives the relative size of the Universe and it is 1 at present and 0 at the Big Bang moment), k is the spatial curvature of the Universe (e.g., for k=0 the Universe is called "flat" and it is an Euclidean space), G is the Newton's constant of gravity, $\dot{a(t)}/a(t) = H(t)$ is the Hubble factor (a recent estimate [27] of H_0 is $H_0 = 73 \pm 3 kms^{-1}Mpc^{-1}$), Λ is the so called "cosmological constant" and it refers to the "dark energy" enabling the accelerated expansion of the Universe [28] and p and ρ are, respectively, the total (i.e. matter and radiation) pressure and energy density of the Universe. From CMB measurements (see next Sec.), it has been found out that the Universe is flat, having a density equal to the critical one, i.e. $\Omega_{tot} = \rho_{tot}/\rho_{crit} = 1$, with

$\rho_{crit} = 3H^2/8\pi G$.

Moreover, it is possible to rewrite the first Friedaman's equation in terms of density parameters, i.e. the relic density of radiation, matter and dark energy:

$$\frac{H^2(z)}{H_0^2} = \Omega_r(1+z)^4 + \Omega_m(1+z)^3 + \Omega_k(1+z)^2 + \Omega_\Lambda, \tag{2.4}$$

where $\Omega_k = -k/H_0^2$ and the redshift, z, is related to the scale factor via the following relation $a(t) = 1/(1+z)$. As we already said in Sec. 2.1, cosmological measurements have pointed out that most of the matter is made of DM, i.e. it is $\Omega_m = \Omega_b + \Omega_{DM}$, with $\Omega_{DM} \gg \Omega_b$.

2.2.1 Pillars of Modern Cosmology and their measurements

Cosmic Microwave Background

We already saw that, from both galactic and extragalactic scales, the presence of DM is provable. However, those observations do not allow us to calculate the *total* amount of DM in the Universe. With this purpose, the analysis of the Cosmic Microwave Background (CMB), which constitutes a big part of the modern cosmology, plays a key role.

The CMB was firstly predicted in 1940 by [29] and then accidentally discovered by [30] in 1965. It is promptly interpreted as the primordial background radiation formed in the following way. Immediately after the Big Bang (approximately 10^{-12} s after), the Universe was a hot, dense plasma made of photons, leptons, and quarks, in which free electrons could move around: this is called "the quark epoch". This plasma was a tightly coupled photon-baryon fluid. In other words, it was opaque to electromagnetic radiation due to Thomson scattering by free electrons, as the photon mean free path before encountering an electron

was very short. At the recombination epoch (i.e. 370000 years after the Big Bang), the Universe cooled down to a temperature ($\sim 3000K$) allowing the binding of electrons with protons to form neutral hydrogen in a high energy state. During the transition of these electrons to the lowest energy state, photons were emitted. Then, the Universe became transparent, photons began to flow freely without interacting with matter. This is called the "era of decoupling", and these emitted photons constitute what is observed today as the CMB [31]. It has been found that the CMB radiation is (almost) isotropic and it follows the spectrum of a black body with a temperature of T = 2.726 K.

CMB is crucial in determining cosmological models and parameters. In fact, it is believed that the matter perturbations from which cosmological structures may have formed, could have left a sort of "imprint" on the CMB radiation, as before recombination the baryons and photons were tightly coupled, as we just saw. These imprints, firstly predicted in 70's by [31] and later observed by COBE in 1992 [32], appear in form of temperature anisotropies (or fluctuations), visible in the CMB temperature power spectrum in form of acoustic peaks (Fig. 2.5). These ones can be explained in the following way: in the primordial plasma, there were initial overdense regions containing DM, baryons and photons, all tightly coupled. Then, baryons experienced at the same time two opposite pressures: on one hand baryons felt into the potential wells created by the overdensity, which gravitationally attracted matter towards it (compressions), but on the other hand the radiation (photonic) pressure pushed the baryons outwards (decompressions), in an expanding spherical shell with the speed of light. In other words, it created sound waves. However, DM stayed at the center of the sound wave, as it interacts only gravitationally. When the recombination occurred and the photons and matter decoupled, baryons were "frozen" in a shell surrounding the DM perturbation. These acoustic oscillations appear today as "oscillatory features" in the

CMB temperature power spectrum. This spectrum, as a function of multiple moments l, [4] is shown in Fig. 2.5. The peaks contain interesting physical signatures too. Indeed, odd peaks correspond to the compression phase, while the even ones correspond to the decompression phase. Other key information inferred from the CMB spectrum are: the curvature of the Universe from the angular scale of the first peak; the baryon density Ω_b from the next peak-ratio of the odd peaks to the even peaks; the dark-matter density Ω_{DM} from the third peak.

Acoustic perturbations made some regions of the Universe hotter and denser than others, i.e. they produce temperature anisotropies on the sky, as shown in Fig. 2.6.

[4] The multipole l is related to the inverse angular size on the CMB, i.e. the angular scale at which the oscillation takes place.

Figure 2.5: Planck 2018 temperature power spectrum. The ΛCDM theoretical predicted spectrum best fit is plotted in light blue in the upper panel. Residuals with respect to this model are shown in the lower panel [33].

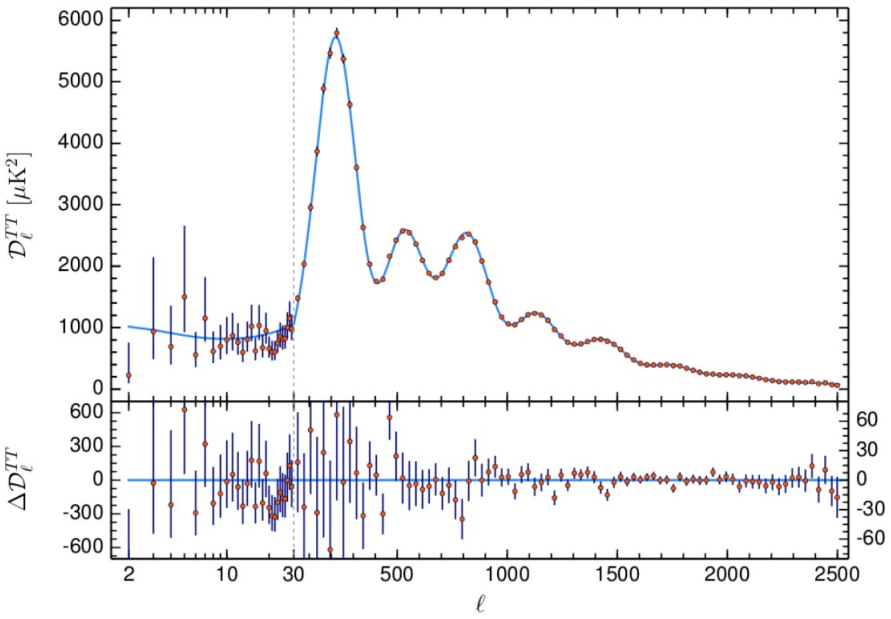

Figure 2.6: CMB Temperature fluctuations: a comparison between COBE (1992), WMAP (2003) and Planck (2013) map. Image taken from [34].

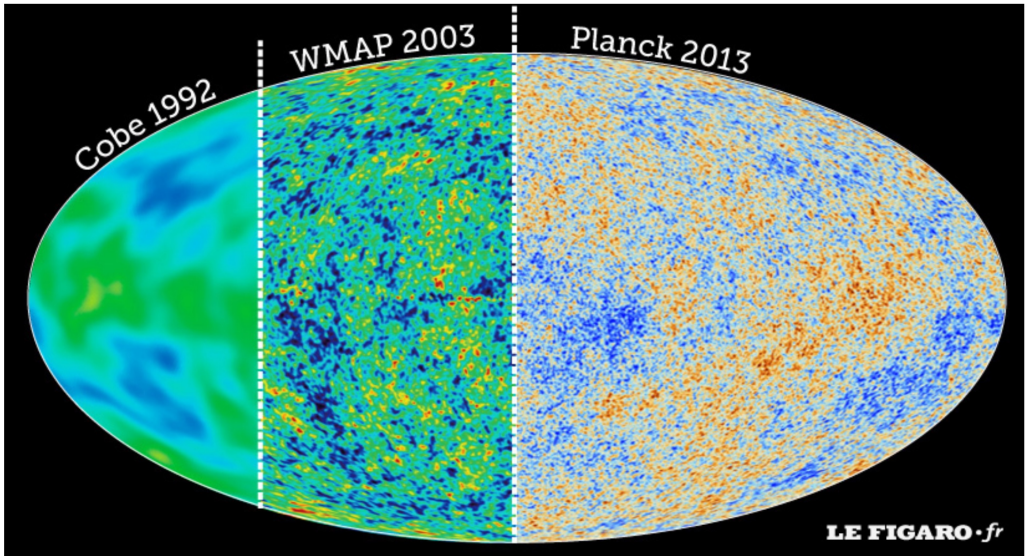

The existence of baryonic acoustic oscillations in the CMB is an important evidence that the Universe contains also non-interacting (i.e. dark) matter. In fact without this DM, radiation pressure would have canceled the perturbations, according to the Silk effect [35]. This effect occurs because the coupling between baryons and photons is not perfect as we approach the epoch of decoupling: as the mean free path of photons increases, it allows them to escape the potential wells, so they can diffuse and smooth out temperature anisotropies. As a result, the acoustic oscillations would be damped on scales smaller than the photon-random-walk length during the epochs of recombination and decoupling. In conclusion, if *all* matter was interacting with photons, the peaks in the CMB spectrum would not be visible. Therefore, since we observe these peaks, we conclude that there is a portion of matter that does not interact with photons.

Most recent Planck studies [33] constrained the matter density in the Universe to be: $\Omega_{mat}h^2 = 0.1430 \pm 0.0011$ [5].

Big Bang Nucleosynthesis

Another pillar of modern cosmology is the Big Bang nucleosynthesis (BBN). It consists in the creation of light elements (i.e., ^4He, D, ^3He and ^7Li)[6] during the first twenty minutes after the Big Bang, when the Universe temperature was $T < 1$ MeV. There is a good agreement of estimates of the predicted primordial abundance of light elements with the observed abundance [36, 37] [7]. Moreover, the abundance of the light elements is related to the baryon-to-photon ratio [39, 40], providing a measure of the baryon content of the Universe. This ratio is also in good agreement with independent CMB measurements [13], such that some cosmologists usually refer to this triumph as "precision cosmology". This is a further support to the Big Bang cosmological model.

Formation of large structures

According to the Big Bang model, it is believed that large scale structures (LSS) in our Universe originated from DM "seeds", i.e. overdensities of matter believed to have derived from primordial (quantum) fluctuations during the inflationary epoch (started from 10^{-36} to 10^{-33} s after the Big Bang singularity) [41, 42, 43, 44]. The analysis of these large scale structures gives essential evidences for DM existence too, as there is a strong agreement between CMB and BBN data with LSS observations. Indeed, N-body simulations starting

[5] h is the Hubble constant in units of 100 km s^{-1} Mpc^{-1}.

[6] Heavier elements than lithium are formed within the stars.

[7] Except for ^7Li, whose calculated abundance is much higher than the observed one. This discrepancy remains an open question [38].

with CMB-like initial conditions (i.e. equations regulating the expansion of the Universe, matter - baryon plus DM - gravity, baryonic gas pressure and dark energy are included) reproduce well the observed large-scale distribution of galaxies, mapped by surveys that combine the redshift measurement and the angular location of astronomical objects up to redshift $z < 0.2$ [45]. Fig. 2.7 shows the consistent comparison between the observed map of a portion of the sky, produced by 2dF Galaxy Redshift Survey and Sloan Digital Sky (which is the most accurate 3D map of the Universe ever produced) with the simulated portion of the sky. These N-body simulations (such as the *Millenium* [46]) reproduce well the hierarchical "bottom-up" formation of the structures. In fact, the system evolves and lets the fluctuations evolve with gravity. Material collapses in regions of high initial density, leading to the creation of DM halos and galaxies. Over time, filaments become more dominant and clusters form at the filament intersections. In other words, firstly low mass objects were formed and subsequently they merged to form higher-mass objects. Structure production slows down about z = 1, because gravity becomes sub-dominant and dark energy dominates the acceleration. Such bottom-up structure formation requires "cold" dark matter[8]. In fact, for hot DM[9], small-scale collapse occurs too late to produce the observed present-day structure.

[8]This type of DM assumes that it moves slower than light.

[9]Hot DM particles decoupled while they were relativistic, differently than cold DM particles.

Figure 2.7: Portion of the sky observed by the 2dF Galaxy Redshift Survey (2dFGRS) (left panel) and Sloan Digital Sky Survey (SDSS) (top panel), compared to the simulated same portion of sky obtained with the Millennium simulations (right and bottom panels, respectively) [47].

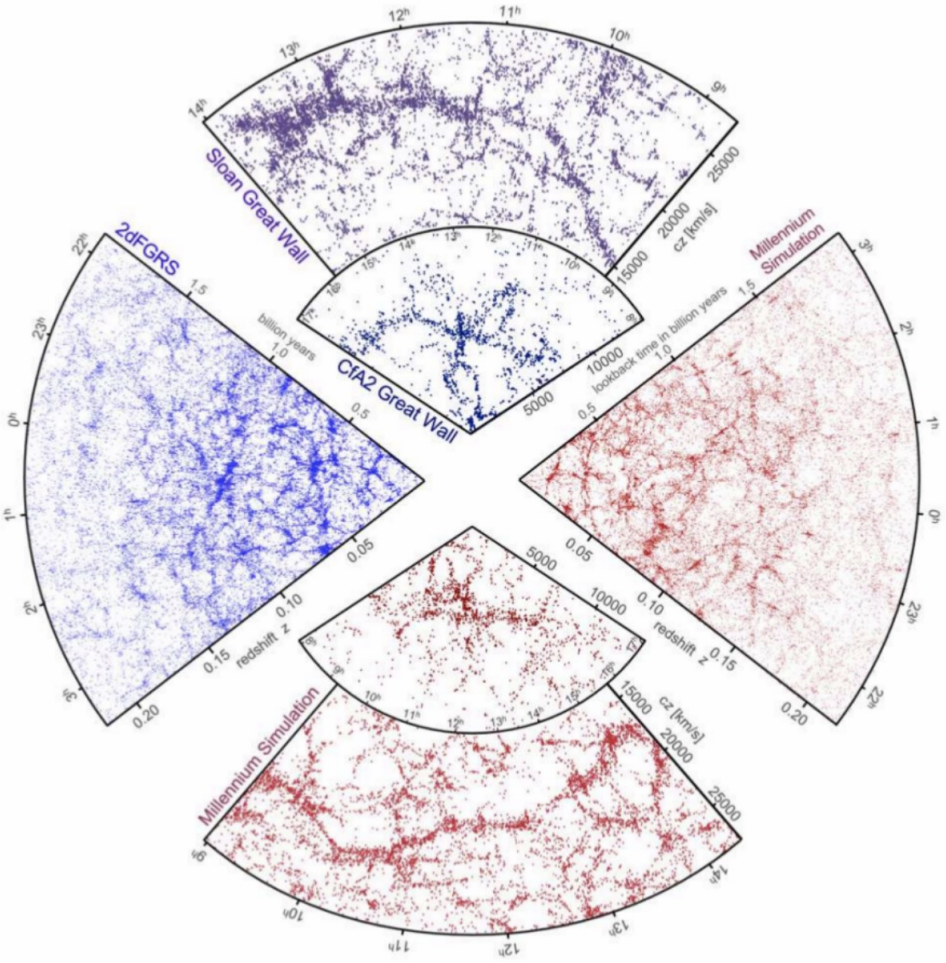

2.3 Dark Matter candidates

We have just seen that there are several evidences of the existence of DM, supported by the current model of cosmology. However, its nature and formation are still under investigation. Nonetheless, there some properties, inferred by experimental observations, that DM candidates must have.

It has been observed that DM particles do not bear any electric charge and interact with ordinary matter only weakly. It must also be massive and "cold", i.e. it should have non-relativistic velocity. Eventually, it also must have a long-stable existence, exceeding the age of the Universe [48], so that they can be seen until now.

The "DM zoo" is populated by different candidates that may satisfy these requirements, as shown in Fig. 2.8. Let's now briefly discuss the main ones in more detail, divided into three categories: non-luminous massive astrophysical compact halo objects (MACHOs), non-WIMP particle candidates and Weakly Interacting Massive Particles (WIMPs).

Figure 2.8: Various DM candidate particles on a mass versus interaction cross-section plot [49].

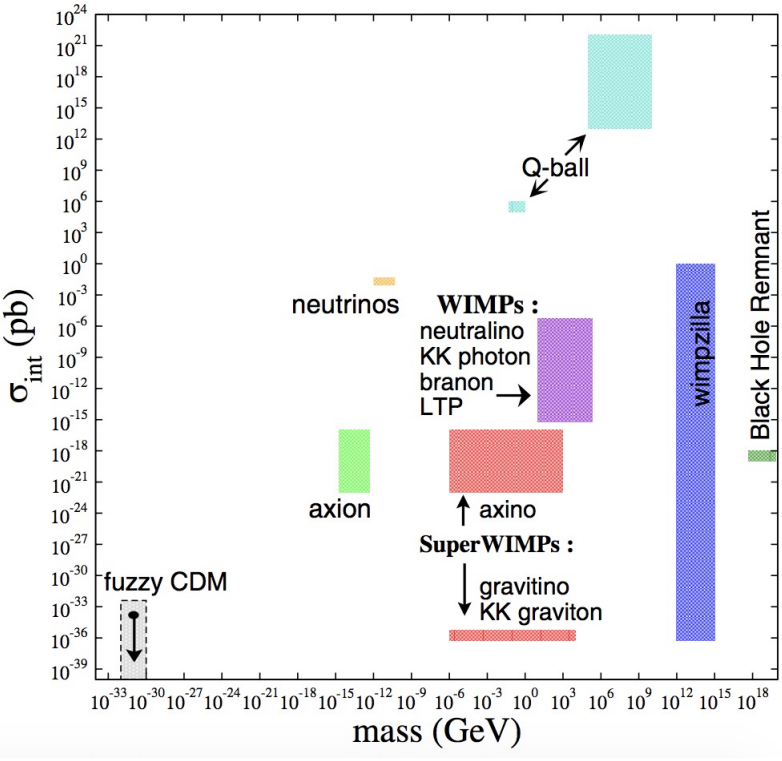

2.3.1 MACHOs

MACHOs (Massive Astrophysical Compact Halo Objects) are objects that emit very low (almost none) radiation, e.g. brown dwarf stars and primordial black holes [50]. However, they would not form the quantity of DM [51] constrained by CMB and BBN. Gravitational microlensing is a good method to look for DM subhalos in MW, however optical surveys for microlensing studies ruled out that MACHOs can form the main contribution to MW DM halo [52]. For example, microlensing measurements in the Large Magellanic Cloud

concluded that MACHOs could not contribute to DM mass for more than $10-20$ % of the total DM amount in galactic halos [53].

2.3.2 Non-WIMPs particles

SM Neutrinos Neutrinos were considered suitable candidates for hot DM, which implies a "top-down" formation scenario (i.e., superclusters formed first and then they fragmented into lower-mass structures). However, this scenario is now obsolete because it has been demonstrated that neutrinos do not reproduce the observed distribution of galaxies [13], as shown in Fig. 2.9.

Figure 2.9: Comparison of observed galaxy distribution with the simulated one with hot dark matter (left) and cold dark matter (right), taken from [54].

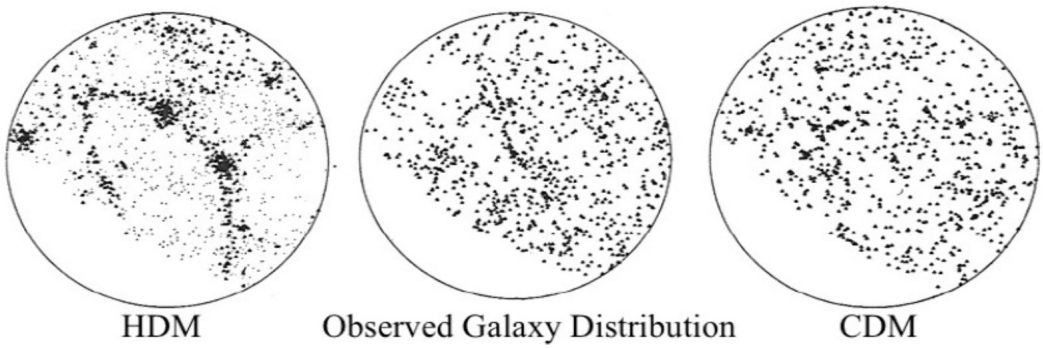

Sterile Neutrinos Sterile neutrinos are SM neutrinos interacting only gravitationally. So, no weak interactions take place, thus the name "sterile". The mass of the sterile neutrinos is not known and could be within the range of 1 eV - 10^{15} GeV [55]. However, sterile neutrinos with a few keV mass are a good candidates for warm DM (i.e. their velocity falls in between hot and cold DM), and on the keV scale, they would be able to produce the structure of the Universe observed today. They also can have a lifetime longer than the age

of the Universe [56], but they are considered unstable. Lastly and unfortunately, it has yet to be confirmed to exist.

Axions Axions were postulated in 1977 as a solution to the strong CP problem in particle physics [57]. Later, they have also often been studied as cold DM candidates [58]. If their mass is within the range of 10^{-12} eV $< m_{axions} < 10^{-3}$ eV, they are expected to weakly interact with ordinary particles [59]. However, the estimation of the their relic density is still uncertain, as it depends on their production mechanism, which is still under debate [60, 61].

2.3.3 WIMPs particles

The Weakly Interacting Massive Particles [62, 63], also known as WIMPs, are currently considered to be the most promising cold DM particle candidates, fulfilling all the DM requirements we mentioned at the beginning. However, they are part of an extension of the Standard Model, such as SUSY [64]). Their mass is in the range GeV-TeV range and, alone, they can constitute the Universe's total DM quantity. Their creation and evolution processes in the early Universe are also very easy to be explained [65]. Let's now briefly describe these processes.

At about 10^{-12} s after the Big Bang, i.e. at temperatures $T \gg M_\chi = 100$ GeV (where M_χ is the mass of the WIMP particle), WIMPs are in thermal equilibrium, with a Maxwell-Boltzmann velocity distribution. They are almost abundant as lighter particles, such as leptons photons, quarks, etc. The WIMPs particle-antiparticle pairs are constantly created - and destroyed - by annihilation into some other particle-antiparticle pairs of SM particles. When the Universe temperature falls below the WIMP mass due to Universe expansion,

i.e. the annihilation rate is lower than the expansion rate, the WIMPs abundance starts to decrease exponentially. Thus, WIMPs can no longer annihilate as they ca no longer find each other. At this point, the WIMPs particles decouple from the thermal bath and the density of the particle remains almost constant. This decoupling phenomenon is called the "freeze-out" [66]. The remaining WIMPs density, which still exists today, is called "relic density" and the aim of different high-energy (> 10 GeV) instruments is, obviously, to detect it.

The relic density has the following value [67] :

$$\langle \sigma_{WIMP} \rangle \approx 3 \times 10^{-26} \frac{cm^3}{s}, \tag{2.5}$$

which is the order of magnitude of an electroweak cross-section (for its precise calculation, see [67, 68]). Fig. 2.10 shows the evolution of the DM density for a constant annihilation cross-section. The DM abundance does not depend explicitly on its mass, but it is interesting to note that the higher the cross-section is, the later the decoupling occurs and the lower the abundance turns out to be.

For all these reasons, the so-called "WIMPS miracle" truly exists and this is one of the main reasons why WIMPs are considered the most promising cold DM candidates: in fact, massive particles with electroweak scale interactions (such as WIMPs) reproduce naturally the today relic DM abundance, which is fixed by the annihilation cross-section.

Figure 2.10: Evolution of the WIMP number density during chemical decoupling (or "freeze-out"), as a function of the universal photon temperature T [67].

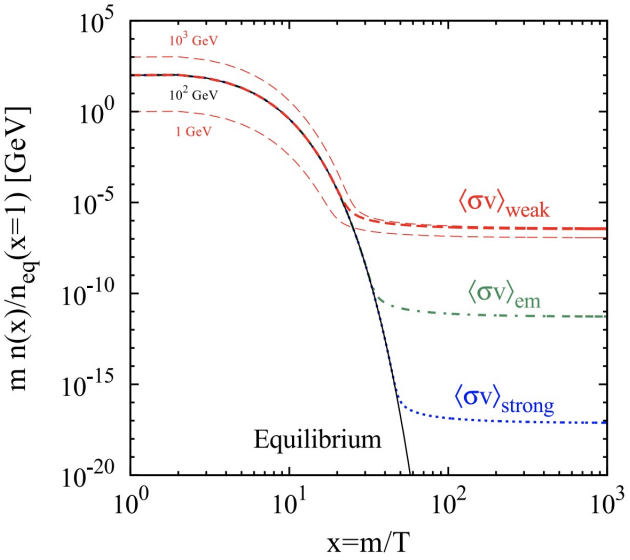

In conclusion, WIMPs could be detected by production at particle colliders, directly from scattering off SM particles and indirectly by annihilation (or decay) into SM particles (as we will see in the next section). The goal of this thesis was, precisely, to indirectly detect any DM signal assuming that WIMPs annihilates into SM particles, such as γ-rays.

2.4 Different types of DM searches

DM search methods are classified into three categories, complementary to one another: direct searches have the goal to observe DM particles themselves, scattering them with SM target particles; indirect DM searches aim at observing the secondary SM annihilation

products of the relic DM annihilation; collider searches involve the production of DM particles by interaction between accelerated SM particles. Fig. 2.11 shows the complementary relation of these methods.

Unfortunately, with none of these techniques, any sign of DM has been detected so far. But now let's review in more detail all these detection methods.

Figure 2.11: Schematic representation of all the possible DM couplings (direct, indirect and production al colliders detection) from DM particle χ to a particle P of ordinary matter [69].

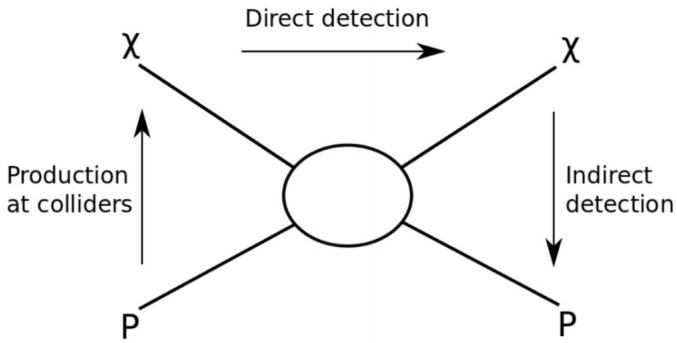

2.4.1 Direct detection

DM direct experiments goal is to measure, in a laboratory, the rate, R, and recoil energy, E_R, of the induced nuclear recoils, and possibly (in directional experiments), the direction of DM particles χ interacting with SM particles X in a process like $\chi X \rightarrow \chi X$ [70, 71]. The rate depends on different variables: the DM mass, the interaction cross-section between the DM particle and the SM particles and also on the local density and velocity distribution of DM in the MW. For a fixed m_{DM}, it is also possible to set limits on the DM-nucleons scattering cross-section.

The expected energy of nuclear recoils induced by WIMP interactions is in the range from several keV to several hundreds of keV, depending on the DM mass and type of nuclei in the detector. So far, no recoil signal that can be attributed to DM has been observed. However, it is worth mentioning the modulated signal detected by DAMA experiment [72]. Usually, direct detection experiments in the 5 - 100 GeV mass range are the most sensitive to DM.

In order to reduce the background noise (like cosmic ray muons and radioactivity), direct search detectors are situated underground (e.g., DAMA/LIBRA is situated at Gran Sasso in Italy [73]), where the flux of cosmic ray muons is largely suppressed and the natural level of radioactivity is lower than on Earth's surface. They usually consist either in large blocks of supercooled scintillator crystal or a large tank of a liquified, heavy noble gas, which offer excellent sensitivity to WIMP-nucleon interactions.

The recoil energy needs be transformed into a measurable signal, such as scintillation light, charge, or phonons (heat). Thus, the most used techniques in direct detection experiments used scintillation, ionization or low temperature phonon techniques. For example, the XENON experiment uses a combination of them [74].

Fig. 2.12 summarizes the most recent results on the WIMP-nucleon scattering cross-section from the main DM direct search experiments. It shows also the irreducible background for direct DM detection, called the neutrino floor [75]. But some models below the neutrino floor can be probed by indirect detection.

Figure 2.12: Summary of direct detection results on the WIMP-nucleon elastic cross section. The orange line at the bottom represents the neutrino floor [71].

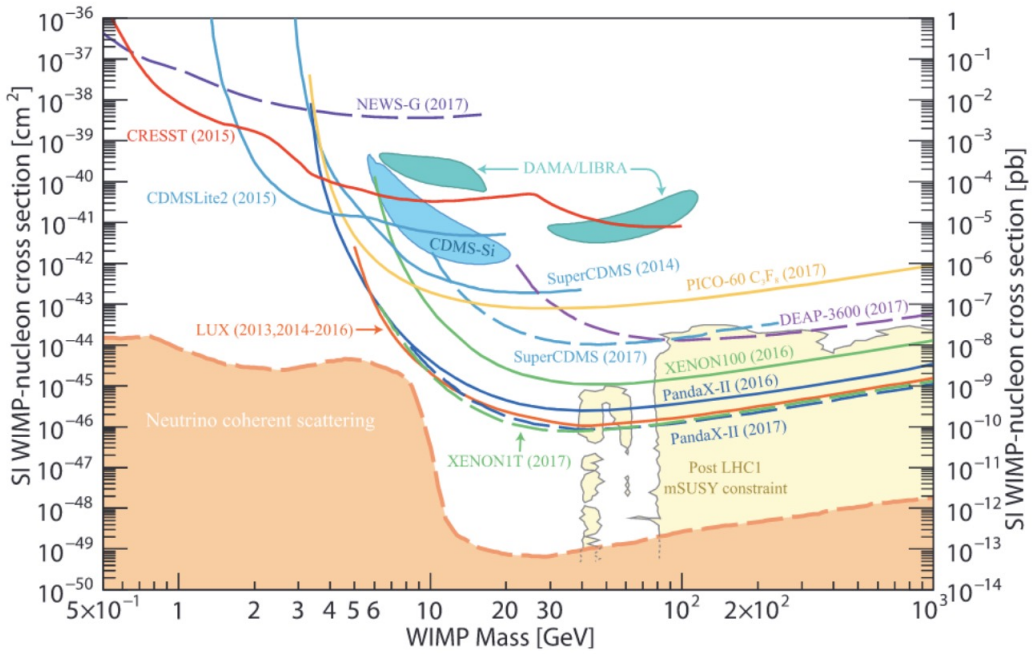

2.4.2 Searches at colliders

The goal of DM searches at colliders is the production, in controlled laboratory conditions, of DM particles χ, which interact with accelerated SM particles, in a process like $XX \rightarrow \chi\chi$ [76, 77]. In collider experiments, the stability of DM particles would need to be established up to timescales necessary to pass through the detector, differently than direct and indirect searches. As DM particles are expected to weakly interact with SM particles, they should not produce a visible signal in collider experiments. Their goal is, then, to detect the

missing transverse momentum of the DM particle. In fact, using the transverse momentum conservation, it is expected that the total momentum in the plane perpendicular to the colliding beams should be zero, also after the collision. Thus, it should be observed a negative vector sum of the transverse momenta of all detected particles.

There are several colliders carrying out DM searches, such as the LHC at CERN [78]. The latter one, situated in Geneva (Switzerland), is the largest operating particle collider in the world. At the LHC, some benchmark channels for DM search are investigated, i.e. simplified models modelling generic features of possible DM signals [79]. We note that colliders themselves need confirmation from direct or indirect searches in order to claim DM discovery. On the other hand, they can discover the existence of new particles that do not belong to SM [80].

2.4.3 Indirect DM searches

The goal of indirect searches of DM is the detection of secondary SM particles produced by DM annihilation (or decay) with a process like $\chi\chi \rightarrow XX$, where X is a SM product and it could be a quark (which then hadronizes), or a boson (i.e., Z, W), as shown in Fig. 2.13. Even though DM was frozen-out, in high clustered DM regions annihilation is still expected at a considerable rate, after propagation through the Galactic or extra-galactic medium.

Photons are the easiest to detect, being their propagation mostly unaffected by the inter-stellar medium and magnetic fields [35, 81, 82].

Figure 2.13: Schematic representation of SM products obtained after WIMP annihilation [83].

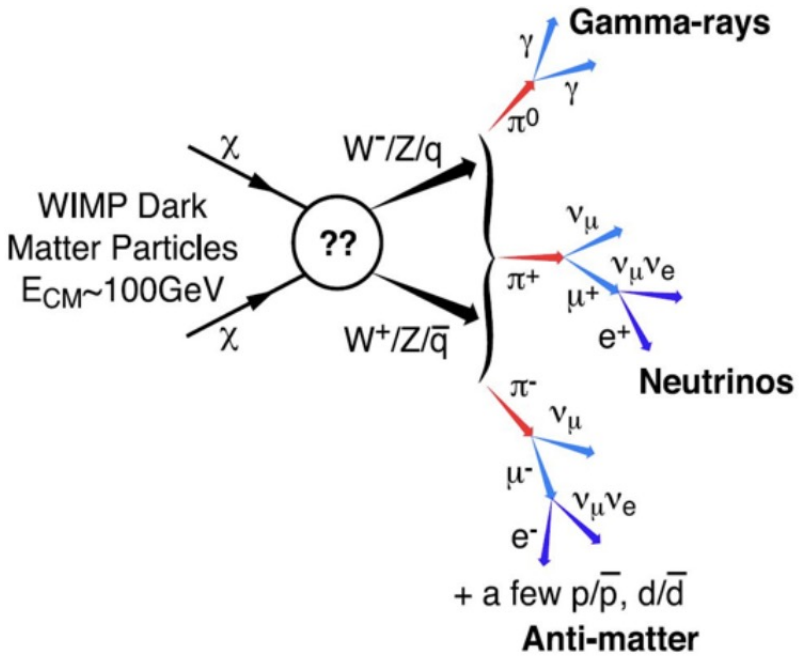

Thus, they point back to their source. They suffer, however, from the significant astrophysical background (e.g., the zodiacal light[10], faint stars..) [84]. Moreover, the γ-ray spectrum is attenuated by the extragalactic background light (EBL)[11]. For this reason, it is not possible to go beyond redshift z=1 with γ rays.

In principle, observations need to be made from space to directly detect cosmic γ rays. This is because photons interact with matter through e^+e^- pair in the energy range we

[10]It is a faint, diffuse glow that is visible in the night sky and appears to extend from the Sun's direction and along the zodiac. It is caused by sunlight scattered by interplanetary dust.

[11]It is the accumulated radiation in the Universe due to star formation processes, plus a contribution from active galactic nuclei.

are most interested in (i.e., GeV to TeV), which results to an interaction length of approximately 38 g cm^{-2}. This is much shorter than the thickness of the atmosphere of the Earth ($1030 g cm^{-2}$). Thus, at VHE, γ rays cannot reach ground based telescopes. In Chap. 5 we will describe in more detail what is the expected γ-ray flux from a DM source.
Different instruments have been designed to detect SM particles, depending on the final state. Experiments that perform indirect DM searches looking for γ rays as secondary SM products are Imaging Atmospheric Cherenkov Telescopes in the VHE regime (IACTs, see Chap. 3) such as MAGIC, H.E.S.S. and VERITAS (about which we are going to discuss in more detail in Chap. 4).
The neutrinos also have a mostly unaffected propagation. Indeed during the path, they interact little, thus reaching long distances. But they interact weakly, therefore, they can be detected by neutrino telescopes, such as ANTARES and IceCube. These experiments are both characterized by huge detector volumes, allowing them to detect neutrinos interactions in spite of these events being rare. Also, ANTARES is an underwater experiment, and this guarantees the elimination of the background composed by cosmic-ray muons, as the Earth acts as a filter.

DM signal enhancement

DM signal can be enhanced by some effects, producing additional photons. The main effects are the so called electroweak (EW) corrections and the Sommerfeld enhancement/effect. Let's briefly discuss them:

- Electroweak corrections: with increasing of DM mass, i.e. at masses greater than the EW scale (> 100 GeV), the intensity of the annihilation emissions increases. So, a release of more radiation follows. Indeed, the emission of W's and Z's leads to

generation of further hadrons in the final state, and therefore it significantly modifies the flux of $\gamma's$ and e^+e^- [85];

- The Sommerfeld effect: it is a non-relativistic quantum effect that takes place when two DM particles with too low kinetic energy (i.e. the relative velocity between DM particles is of order of $\beta = v/c = 10^{-5}$, where $v = 10kms^{-1}$) interact. Thus, their wave function can be distorted by a potential (Yukawa potential) [86, 87]. Therefore, the actual annihilation cross-section times velocity is enhanced by the "Sommerfeld boost" (or enhancement) S, with the following relation: $\sigma v = S \times \sigma v_0$, where σv_0 is referred at the tree level. For very small relative velocities, the thermal relic cross-section can be enahnced up to a factor 10^5. The enhancement also strongly depends on the particle mass. In fact, the largest resonances are obtained for small DM masses, as shown in Fig. 2.4.3 [88].

Figure 2.14: This plot shows the Sommerfeld boost S as a function of the m_{DM}, for different values of velocity β. Fig. taken from [88].

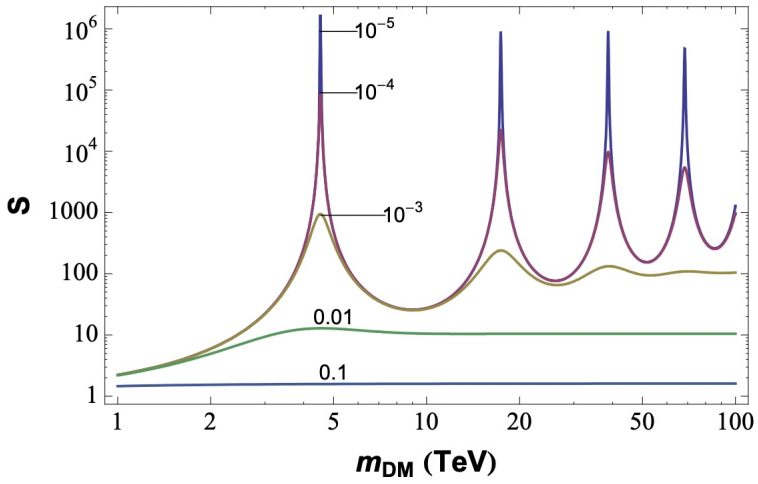

2.5 DM targets for indirect γ-ray searches

At Earth, for a canonical cross-section and $m_{DM} > 1$ GeV, 10^{-26} annihilations per second and cubic centimeter are expected. This leads to less than one annihilation every 1000 years, even for a detector of a cubic kilometer in size. This suggests that ideal DM targets must be relatively close and must have a low common astrophysical background. Good targets for indirect DM searches are:

- The Galactic Center (GC): it is located around 8.5 kpc from the Sun, so it is the nearest target for DM. It is predicted to store a very large density of DM. Its J-factor (for its definition, see Sec. 5.1), integrated in a region of 1°, is $\log_{10}(J/GeV^2cm^{-5}) = 21.0$. For this reason, it may be the region that provides the largest DM signal [35]. However, GC is not a clean environment: it has many standard astrophysical sources emitting in the VHE band, which represent a background for DM search. Thus, it is complicated to assign the origins of the γ-ray radiation observed.

- The Galactic Halo: it is a cleaner environment than the internal part of the Milky Way [52], as the expected DM signal seems to peak at the center of GC. Moreover, it has less VHE γ-ray sources that in the GeV-TeV energy range. Its expected annihilation signal is much lower than the GC one, but the systematic uncertainty of the DM profile is lowered, as the various halo models begin to converge beyond several kpc distance from the GC.

- Dwarf Spheroidal galaxies (dSphs): they belong to the Milky Way Local Group of Satellites. They are one of the most DM-dominated objects in the Universe and they are located at nearby distances from Earth (25-250 kpc). So far, 56 dSphs satellites have been detected [89] but more dSphs are expected to be observed with

future optical surveys (a 3-4 times greater factor) [90]. Since dSphs do not primarily host star formation regions and are almost gas-free, they have a clean γ-ray environment, and DM annihilation could easily be correlated with a potential γ-ray emission. DSphs have a J-factor, integrated in a region of radius 0.5°, of the order of $\log_{10}(J/GeV^2cm^{-5}) = 18 - 19$. They are primary observation targets for IACTs.

- Galaxy Clusters: they are the largest DM-dominated gravitationally-bound systems. The 80% of their mass is believed to be constituted by DM.[91]. However, they lie at large distances from the solar system. Galaxy Clusters have a J-factor, integrated in a region of radius 1°, of the order of $\log_{10}(J/GeV^2cm^{-5}) = 16 - 17$.

- DM clumps: those within the MW DM halo could be observable from Earth. However they are hard to localize, so they are not useful for pointed observations.

Chapter 3

VHE γ-ray astronomy and IACTs

VHE γ-ray astronomy is based on the detection of γ-ray photons with energy ranging from 100 GeV to 100 TeV. Luckily, this energy range will be extended to around 300 TeV thanks to the next generation of Cherenkov telescopes, such as CTA [92]. Due to the fast decreasing photon flux with increasing energy and the small area ($\sim 1\ m^2$) of space-based detectors, detection of γ-ray photons in this energy range is beyond the capability of this type of instruments. For example, from Crab Nebula, which is one of the strongest VHE sources detected so far, above 1 TeV we can collect $2.2 \times 10^{-7} m^{-2} s^{-1}$. Thus, we need very large ground-based detectors in order to detect few photons every hour. In this context, ground-based telescopes such as Imaging Array Cherenkov Telescopes (IACTs), like VERITAS, MAGIC and H.E.S.S. or water Cherenkov detectors (WCD, e.g. HAWC) play a key role. An image of IACTs is shown in Fig. 3.1.

Figure 3.1: An image of VERITAS, MAGIC and H.E.S.S. observatories.

With IACTs, photons are not detected directly as they need to first interact with matter (i.e. the Earth's atmosphere). In fact, they create an electromagnetic cascade and, hence, a shower of secondary particles. Consequently, ground-based telescopes indirectly observe γ rays by detecting these secondary particles and Cherenkov light resulting from their transit through the atmosphere of the Earth. These are very efficient instruments with extremely large effective areas. However, they have a limited field of view (FoV) and a low energy threshold, because they have to discriminate photons from the background (we will see all these details in Chap. 4).

This thesis used data observed by the imaging Cherenkov Telescope VERITAS. Therefore, in the next section we are going to talk about the basic principles of Cherenkov radiation and the IACTs technique.

3.1 Cherenkov Radiation

Many years before P. Cherenkov was even a physics student, first in 1888 the English polymath O. Heavisid [93] and later in 1904 A. Sommerfeld, they both predicted theoretically the Cherenkov radiation as conical wave. In 1910, M. Curie saw a blue-ish light in a highly concentrated radium solution, but she did not investigate further. Only in 1934 P. Cherenkov detected the radiation experimentally under the supervision of S. Vavilov [94]. For his doctorate thesis, he studied the luminescence of uranium salt solutions excited by γ rays. In his underwater experiments, he saw a faint light blue light around a radioactive preparation. He discovered that if a charged particle, most commonly an electron, moves within a transparent and dielectric[1] medium with a velocity which is higher than the speed of light has in it (however always lower than the speed of the light on a vacuum, c)[2], it generates a blue radiation called "Cherenkov radiation" (see Fig. 3.2) [95]. This effect can be described in the following way.

[1] I.e. that can be polarized electrically.

[2] In vacuum it is known that the speed of light is an universal constant (c=299792458 m/s), but in a medium it can be perceived to be slowed by it. For example in water the speed of light is 0.75 c.

Figure 3.2: The blue glow of Cherenkov radiation, seen here at a nuclear-reactor core. Credit: US Department of Energy/SPL [96].

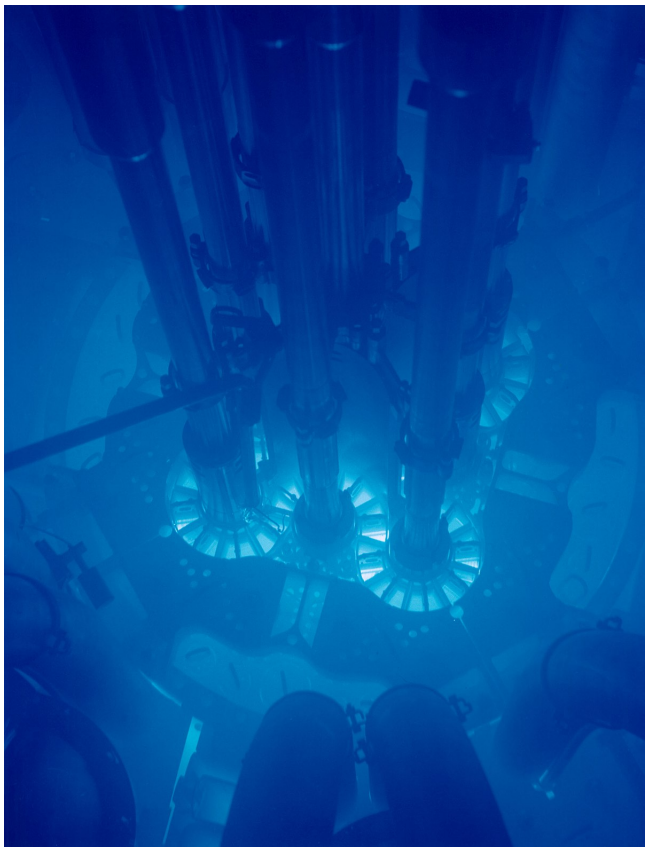

From classical physics (so with a slow speed, i.e. if $v < c/n$[3]), we know that charged particles emit electromagnetic (EM) waves, which form spherical wavefronts propagating with the phase velocity of that medium ("Huygens' principle") [97]. In response, the particles of the medium will polarize. That is, the molecules in the polarizable medium get excited by the EM waves from the charges particle and, on returning to their ground-state, they

[3] n is the refractive index of the medium.

will re-emit, as photons, the energy required to achieve the excitation. These photons form the spherical wavefronts. However, when $v < c/n$, the polarization field is symmetric and it does not lead to any radiation field at large distance, so the generated wavefronts do not interfere (see Fig. 3.3, a).

Figure 3.3: Polarization phenomenon produced in a dielectric medium by a charged particle passing through, for: a) $\beta < 1$ and b) $\beta \sim 1$ [98].

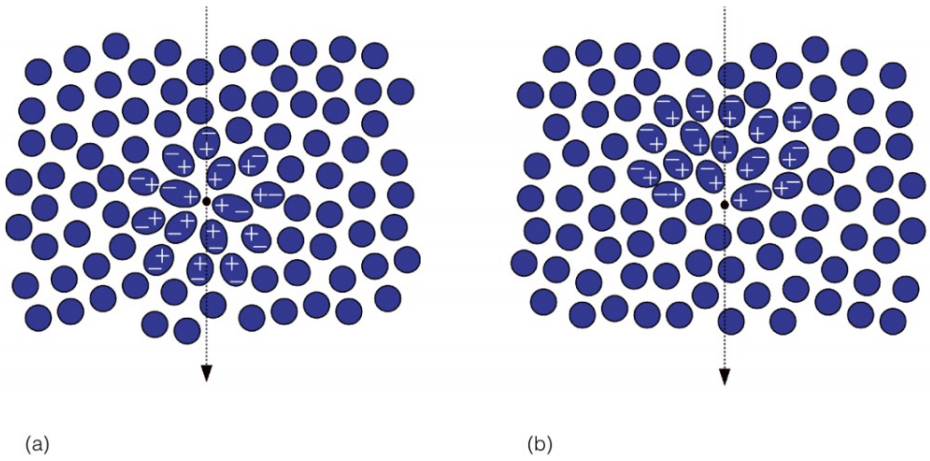

But if a charged particle has a speed higher than the speed of light in the medium, the wavefronts will constructively interfere (see Fig. 3.3, b), and cone-like light signal (the Cherenkov light) occurs at a particular angle, called the Cherenkov angle θ_C[4], defined as (referring to Fig. 3.4) [99]:

$$\cos(\theta_C) = \frac{AC}{AB} = \frac{1}{\beta n}, \tag{3.1}$$

[4]This refers to half angle.

Figure 3.4: Schematic representation of Cherenkov radiation propagation phenomenon [98].

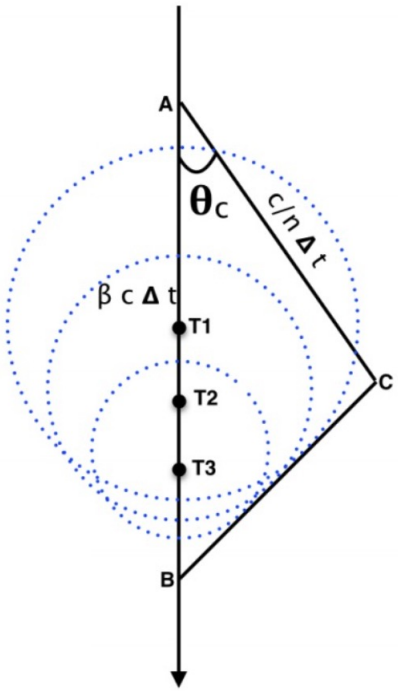

where n is the refractive index (depending on the altitude) of the medium and β represents the velocity of the particle ($\beta = v/c$). The Cherenkov angle increases as one goes lower in the atmosphere. The Cherenkov light is emitted in an opening angle of $2\theta_C$, which forms a circular ring around the particle trajectory of radius $R_C = (h - h_{obs}) \tan \theta_C$, where h_{obs} is the altitude of the observation site. At the VERITAS site ($h_{obs} = 1.26$ km), the radius of circular ring formed on the ground for an emission height of 10 km is about 100 m. This light arrives homogeneously within a time interval of few nanoseconds (2 ns up to 5 ns).

The minimum energy required to emit Cherenkov radiation depends also on the mass of

the particle, which is given by:

$$E_{min} = \frac{mc^2}{\sqrt{1-\beta^2}} = \frac{mc^2}{\sqrt{1-n^{-2}}}. \tag{3.2}$$

For this reason, light particles, such as electrons and positrons, dominate the Cherenkov emission in air showers. Above the minimum energy, the number of Cherenkov photons, N_{ph}, emitted per unit of wavelength, λ, and path length at the Cherenkov angle, θ_C, is given by the Franck-Tamm relation [100]:

$$\frac{d^2N_{ph}}{dxd\lambda} = \frac{2\pi\alpha}{\lambda^2}\sin^2(\theta_C), \tag{3.3}$$

where $\alpha \approx 1/137$ is the fine structure constant. From Eq. 3.3 it can be inferred that the Cherenkov light distribution peaks at short wavelengths (UV-blue).
Cherenkov photons interact with atmosphere via scattering and absorption, generating particle showers (see next Sec. 3.2). This leads to a decrease of number density of photons reaching the observation level.

3.2 Extensive Air Showers

Cosmic rays (CRs) are defined as relativistic charged particles accelerated both in Galactic and extragalactic objects. They are composed primarily of nuclei (99%, among protons, helium nuclei and heavier nuclei) and leptons (1%, among electrons and positrons)[101]. The origin and acceleration of CRs are still debated. But we know that when high-energy CRs enter the Earth's atmosphere, they produce secondary particles and thus an extensive air shower (EAS) is initiated [102] (Fig. 3.5).

Figure 3.5: Example of photon shower simulated with the simulator package CORSIKA by [103, 104] (see next section about it).

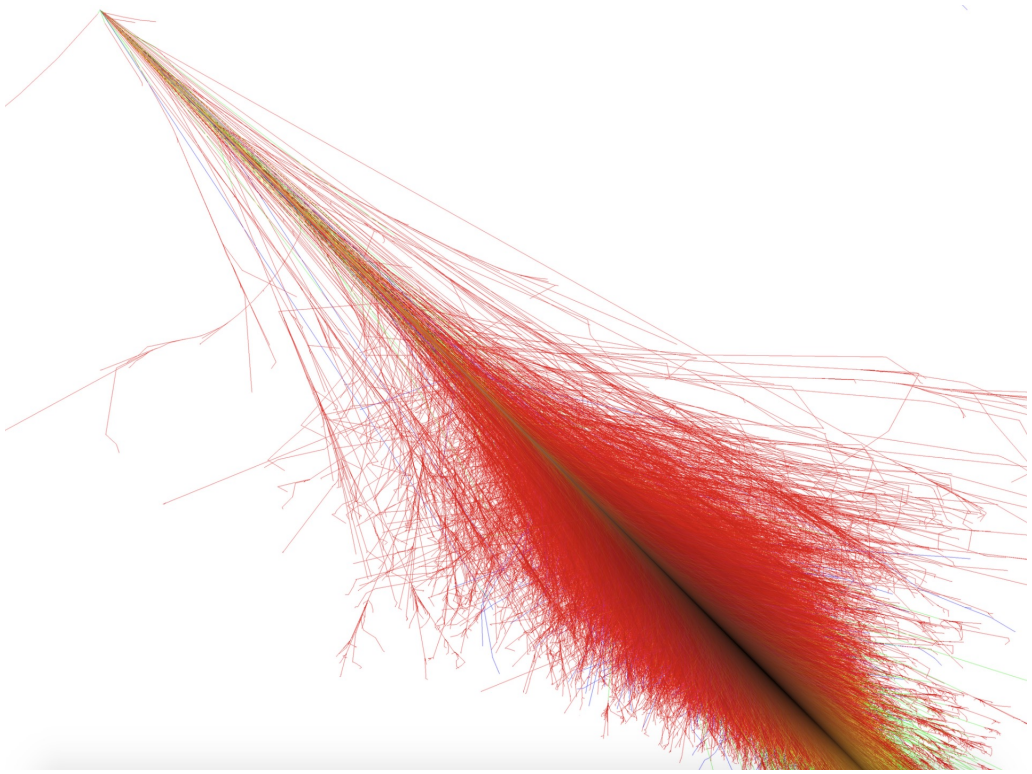

The number of secondary particles produced depends on the energy of the primary particle interacting with the atmospheric nuclei: the number of secondary particles increases, while the energy of the primary particle is divided among the secondary ones[5]. In this way, the ground-based telescopes, such as IACTs and WCDs, can collect and detect the Cherenkov light generated by these particles and reconstruct the main properties of the primary γ-ray photon.

[5] In case of γ-ray photon hitting the atmospheric nuclei, its the energy must be at least 50 TeV in order to generate a sufficient number of secondary particles reaching the ground.

The type of shower depends on the nature of the hitting particle. In case of a photon or electron/positron as primary particle, an electromagnetic shower begins, as most of the interactions are electromagnetic. If instead the primary particle is a hadron, then the hadronic shower is generated. This type of shower is more complex and strong and weak interactions occur.
In the following, such difference will be illustrated in more detail.

3.2.1 Electromagnetic showers

Electromagnetic showers are generated by γ-ray photon interacting with the atmospheric nuclei [105]. The first interaction that takes place is the electron-positron pair production ($\gamma \rightarrow e^+ + e^-$). Afterwards, the electron and positron interact between each other via bremsstrahlung process ($e^{\pm} \rightarrow \gamma + e^{\pm}$), where the electron (or positron) path is deflected in the electric field of atomic nuclei and generates an electron (or positron) and a photon. In this way, a cascade of these particles (photons, electrons and positrons) is generated. In fact, if the energy of the previously photon produced via bremsstrahlung process is high enough, then a pair production occurs again which, later on, produces again photons via bremsstrahlung and so on. This type of cascade is called electromagnetic cascade, as the energy loss processes involved are electromagnetic. Every time the secondary particles produce further particles, the number of particles increases and the energy per particle decreases, getting these deeper and deeper into the atmosphere. At the same time, the energy is equally split between newborn particles. The propagation of the cascade stops when the final particles reach the so called "critical energy" ($\sim$ 85 MeV), after which electrons lose their energy due to ionisation becoming dominant over bremsstrahlung. The photon density on the ground appears also quite uniform up to a distance of about 120 m, which

is called "Cherenkov light pool" of the shower. Beyond this radius, the number of photons exponentially decreases.

Fig 3.6 illustrates an example of electromagnetic cascade, whose variables are based on the model proposed by [106]. Let's describe it in more detail.

Figure 3.6: Schematic representation of electromagnetic cascade after a γ-ray photon interacts with the atmospheric nuclei [106].

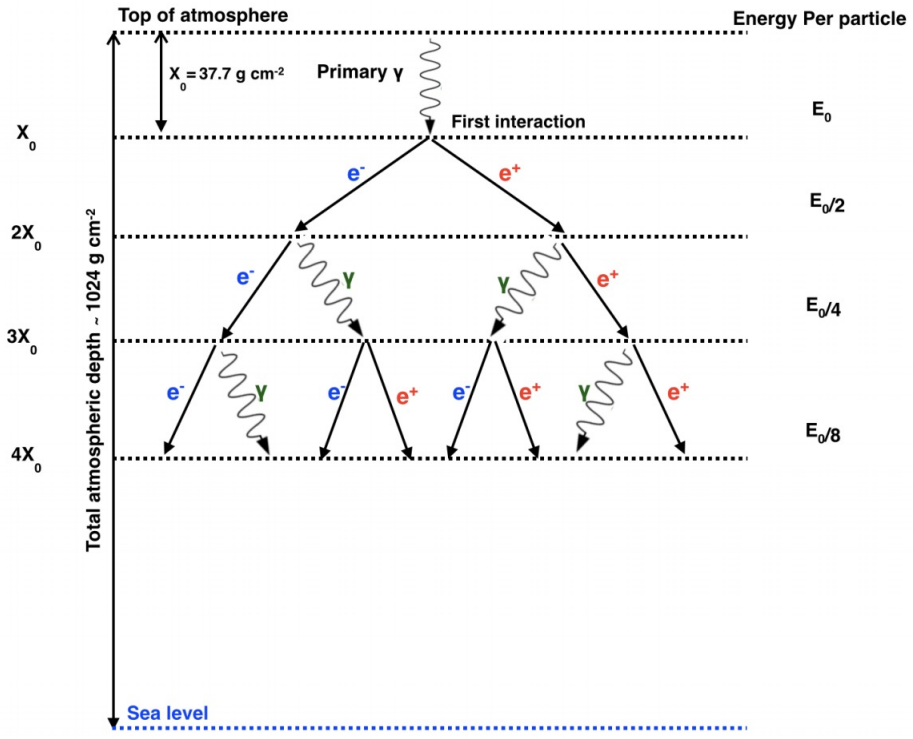

After n radiation lengths[6], the total number of particles produced is:

$$N = 2^n, \tag{3.4}$$

and the energy of the shower is:

$$E = E_0 2^{-n}, \tag{3.5}$$

where E_0 is the initial energy. After reaching the critical energy defined before, the maximum number of radiation lengths is:

$$n_{max} = (ln2)^{-1} ln(\frac{E_0}{E_C}). \tag{3.6}$$

Following this, the maximum number of reproduceable particles is given by:

$$N_{max} = 2^{n_{max}} = \frac{E_0}{E_C}. \tag{3.7}$$

The longitudinal development of the electromagnetic shower was modeled by Hillas [107]. He calculated N_e, i.e. the total number of secondary electrons and positrons as function of the primary energy E_0 and of the atmospheric depth t (expressed in radiation length). Fig. 3.7 shows the relation between N_e and the atmospheric depth, for different initial energies. It illustrates the main properties of the electromagnetic shower development: i) the number of the particles increases exponentially in the initial phase, ii) the maximum number of particles is proportional to the energy of the primary particle and iii) the depth

[6]The radiation length is defined as the mean distance over which a particle reduces its initial energy of $1/e$.

of the shower maximum grows logarithmically with the primary energy. For lower energies primaries, the shower develops at high altitudes in the atmosphere and then it dies relatively soon.

Figure 3.7: Longitudinal development of electromagnetic cascade as function of the atmospheric depth [108].

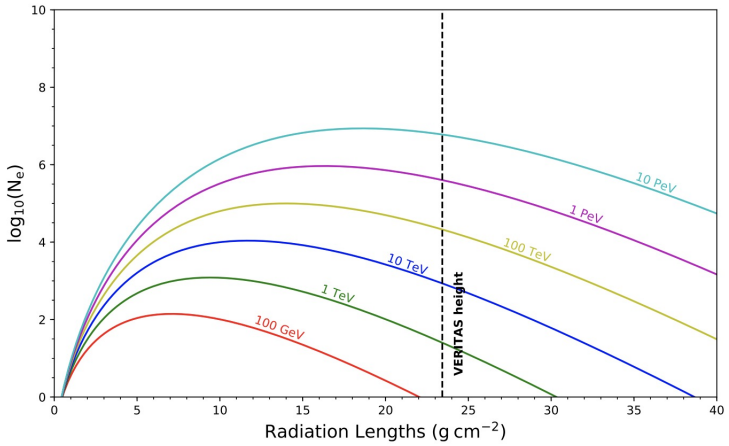

The electromagnetic cascades are quite beamed along the direction of the primary photon due to small transverse momentum. However it is also slightly spread laterally, due to multiple Coulomb scattering of electrons in the air. This spreading scales with another quantity known as the "Moliere radius", which is the radius of a cylinder containing about 90% of the shower energy. On the contrary the hadronic shower appears to be much wider (see Fig. 3.8 for a comparison), but let's discuss this in the next section.

Figure 3.8: An electromagnetic cascade after a 300 GeV γ-ray photon interacts with the atmospheric nuclei, compared to an hadronic one triggered by a 1 TeV proton [108].

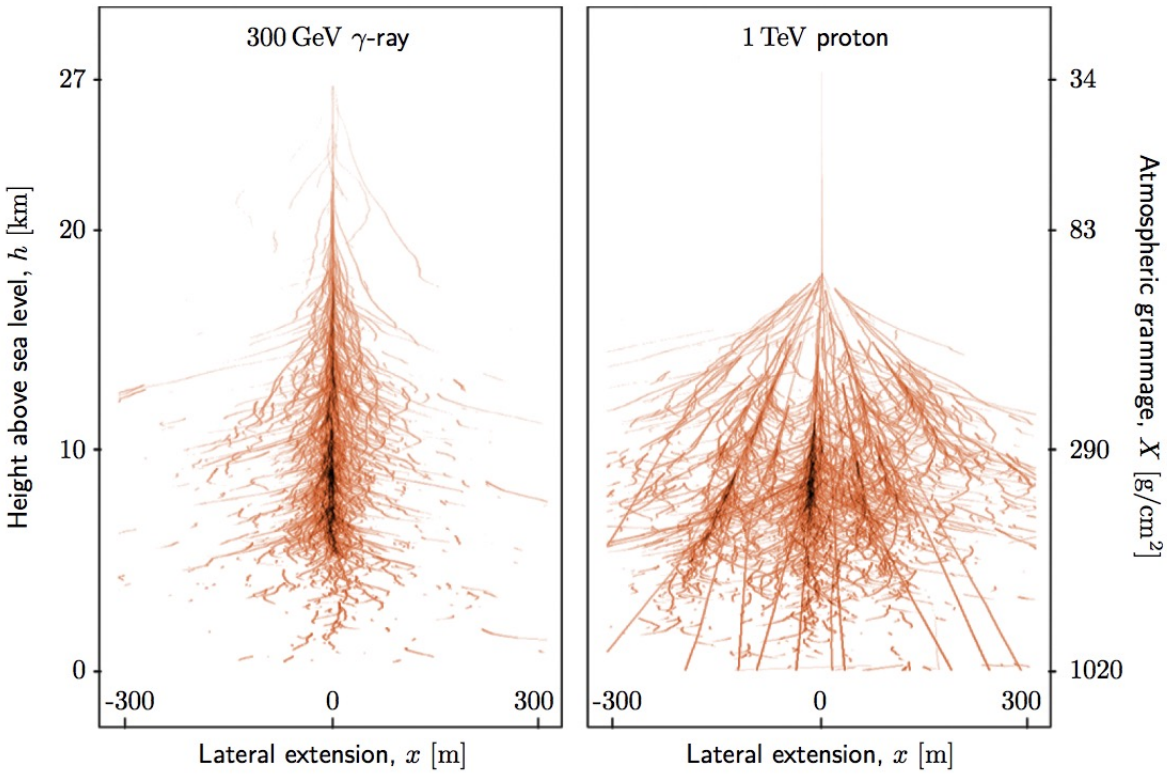

3.2.2 Hadronic showers

When a high-energy cosmic ray particle like protons (or heavier nuclei such as helium or iron) interacts with the Earth's atmosphere, it initiates an hadronic air shower [109]. In this case, the shower develops as a composition of electromagnetic sub-showers and production of hadronic multi-particles. This type of cascade penetrates deeper into the atmosphere with respect to an electromagnetic cascade, since the mean free path for interaction of a

proton of energy of 1 TeV is twice the electromagnetic radiation length (i.e. it is $\sim$ 85 g cm^{-2}). The secondary particles produced have higher transverse momentum (by inelastic scattering and decays processes), and for this reason the hadronic cascade is much larger than the electromagnetic one. Fig. 3.9 shows the structure of an hadronic shower. It is constituted by a nuclear core and pions (π^+, π^-, π^0). Pions π^0 immediately decay after $1.78{\times}10^{-16}$ s into two γ-photons which initiate electromagnetic showers. In the meantime, charged pions with longer lifetime (2.55×10^{-8} s) decay into charged muons, according to $\pi^{\pm} \rightarrow \mu^{\pm} + \nu_{\mu}$. These muons with very high energy can be observed on the ground and constitute the muonic component of the showers, with a life time of 2.2×10^{-6} s before they decay. Also there are low-energy muons that decay according to $\mu^{\pm} \rightarrow e^{\pm} + \nu_{\mu} + \nu_{e}$, and the electrons/positrons produced can either start an electromagnetic shower or be absorbed in the atmosphere.

Figure 3.9: Sketch showing the structure of an hadronic shower [110].

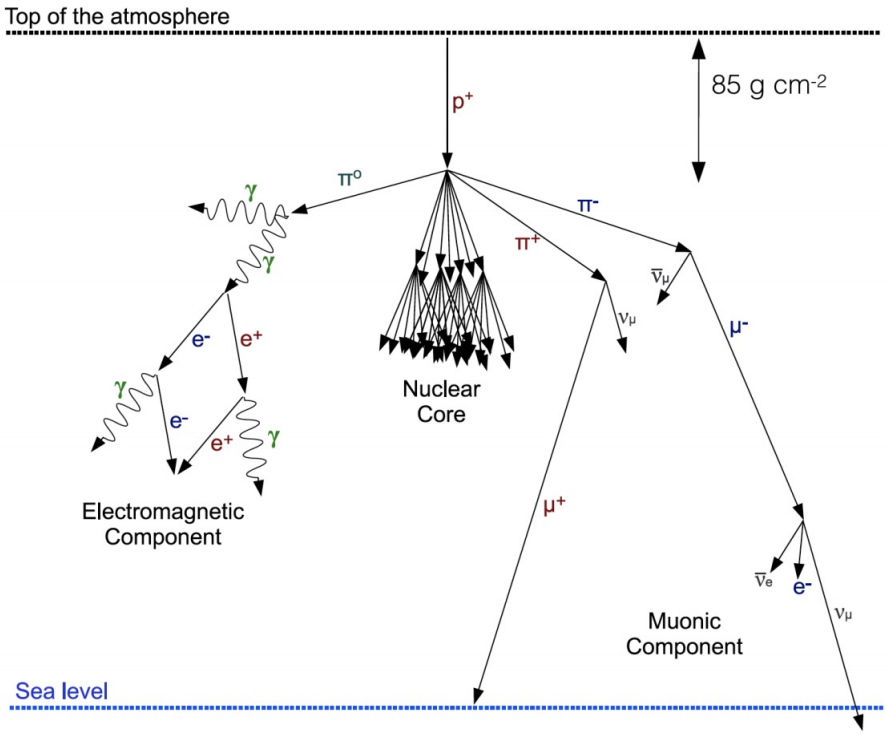

3.2.3 Distinguishing Electromagnetic and Hadronic showers

One of the challenges of VHE γ-ray detection is to distinguish between γ-ray initiating an electromagnetic shower and what we can refer to as background constituted by cosmic hadrons (protons and helium nuclei), and is the most prominent component in number with respect to γ rays. As a matter of fact, we expect that the event rate from a typical γ-ray source above 100 GeV is $\sim 0.01\ s^{-1}$, five orders of magnitude lower than the cosmic ray

background rate ($\sim 2400\ s^{-1}$)[7].

The distinction is made based on different properties of electromagnetic and hadronic showers. For example, we already said that hadronic showers are wider, more irregular and longer, while electromagnetic showers appear to be more compact than the hadronic ones, due to their lower transverse momentum. Indeed, the secondary particles of hadronic showers have high transverse momentum due to inelastic scattering and decay processes. This leads to a much wider lateral extension than electromagnetic showers, in which the lateral spread is determined by elastic multiple Coulomb scattering. In this one, the mean scattering angle for high energy photons is very small, indeed (see Fig. 3.10).

Another criterium to use to distinguish different types of showers comes from the arrival direction. In fact, hadrons arrive isotropically on Earth as they are deflected by the interstellar magnetic fields (being charged particles).

Also, the arrival time of photons in the hadronic shower (10 - 15 ns) is longer than the electromagnetic shower (2 - 5 ns) due to the development of sub-showers.

[7]With respect to the area of the Cherenkov light pool on the ground (about $3 \times 10^8 cm^2$) and to the solid angle ($4 \times 10^{-3} sr$) corresponding to the FoV of the Cherenkov telescope (~ 4 deg).

Figure 3.10: Vertical propagation comparison between the electromagnetic and hadronic showers. Difference of the two showers on the ground too [104].

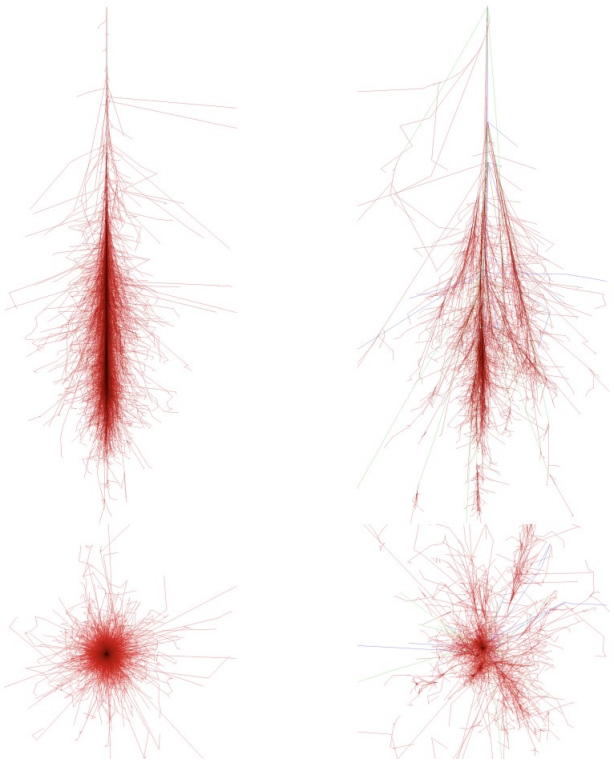

3.2.4 Simulating air showers

There are two methods describing the propagation of particles through the atmosphere: analytical and numerical. The first ones are efficient to predict the correct average values of the observables, however the numerical methods via Monte Carlo (MC) simulations are essential to describe the so called "shower to shower fluctuations"[8] [111].

[8] Primary particles with the same energy, mass and direction produce secondary particles with parameters that are different in different shower.

One of the most used air showers simulations is (COsmic Ray SImulations for KAscade (CORSIKA) (used in this thesis too) [112]. CORSIKA simulates decays and interactions of muons, hadrons, nuclei and photons up to primary particle energies of $\sim 10^{20}$ eV. This is done by simulating the trace of the single particles through the atmosphere. It also takes into account the atmospheric density, its chemical composition and the geo-magnetic field. Also a good knowledge of the local atmosphere is important.

Fig. 3.11 shows the difference in the Cherenkov photon density on the ground from simulated hadronic and electromagnetic air showers.

Figure 3.11: Difference in the Cherenkov photon density on the ground from simulated hadronic and electromagnetic air showers. Figure courtesy of G. Maier.

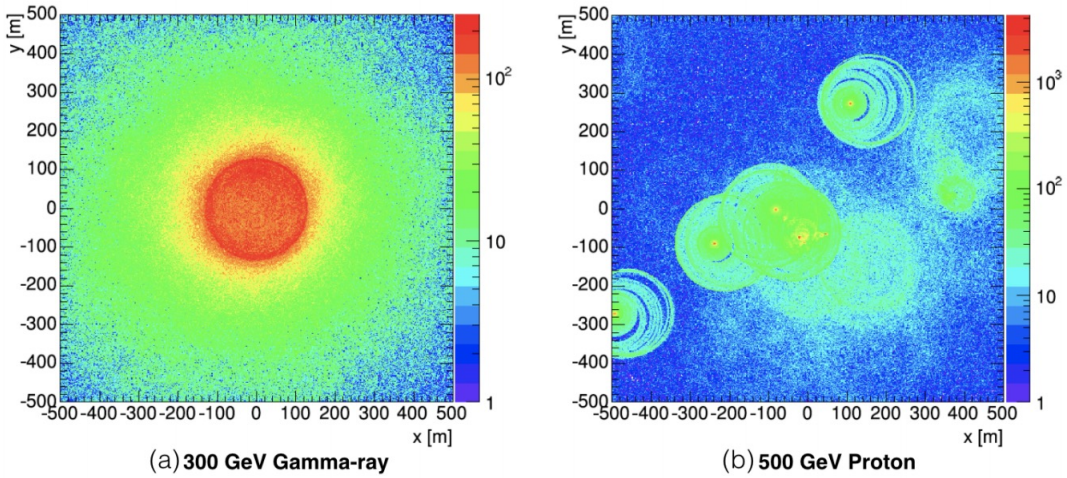

3.2.5 Imaging Atmospheric Cherenkov Technique

The concept

The basic principle of Imaging Cherenkov Telescopes is shown in Fig. 3.12.

Figure 3.12: Cherenkov light pool, generated by an electromagnetic shower due to a photon (primary particle) entering the Earth's atmosphere and detected by an IACT [113].

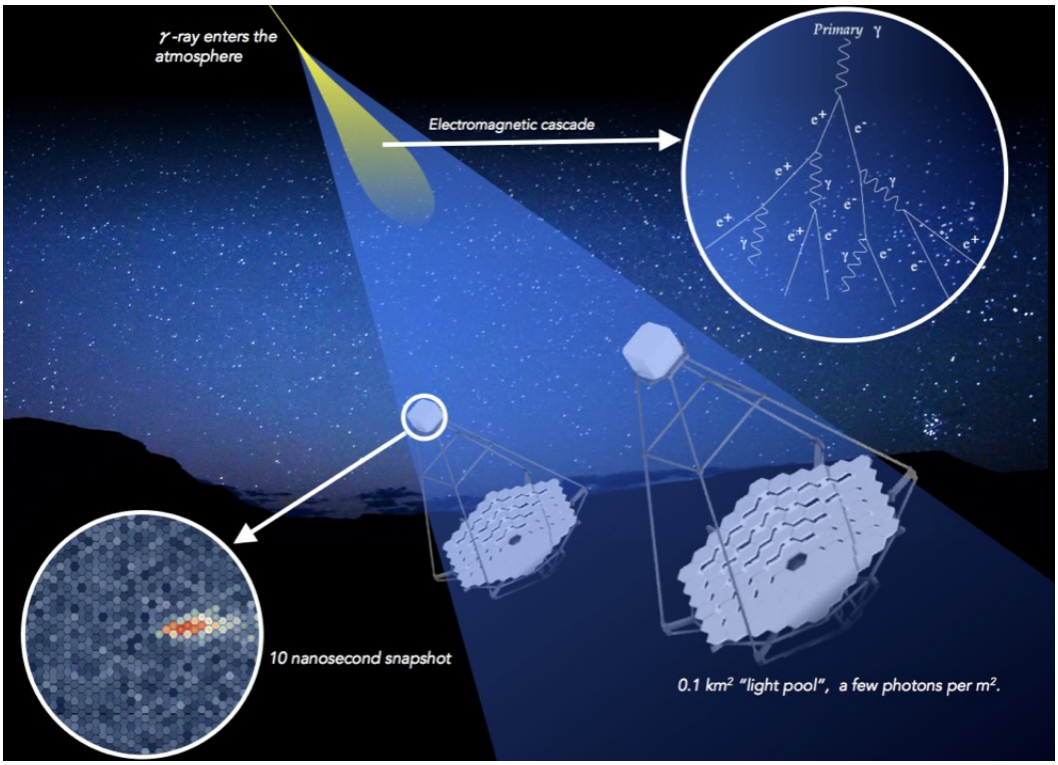

The Cherenkov light, produced by the EAS, is reflected onto a camera which is located in the focal place of the telescope. The camera is constituted by hundreds of light-sensitive detectors, such as photo-multiplier-tubes (PMTs). These type of camera are very rapid in detecting fast (nano-seconds) Cherenkov pulses emitted by EAS. IACTs have typically a FoV of about $3° - 5°$ and an effective collection area of about 10^5 m^2.

As the γ-ray shower has typically a longitudinal extension of 10 km and a transversal extension of 50 m at E = 1 TeV, for a total light pool with a radius of about 100 m, the

image will appear on the camera with an elliptical shape. The light content of the image and its shape is used to infer information on the initial energy, as the number of Cherenkov photons on the ground is proportional to the energy of the initial particle, as we saw. Also, the direction of the initial particle is determined from the orientation of the image.

IACTs usually perform in stereoscopic mode, meaning that the Cherenkov radiation of the air shower is detected at the same time by multiple telescopes and from different angles. This is done to better reconstruct the shower image and properties. Also in this way, it is possible to increase the effective collection area in order to boost the sensitivity.

IACTs require large reflectors to collect as much light as possible since the Cherenkov radiation is very faint. As we said, beyond 120 m, the number of photons starts to decrease. For this reason, IACTs need to place their telescopes within this light pool to record the shower image. This means that the effective collection area depends on the size of the Cherenkov light pool generated on the ground and not on the size of the telescope mirror. All these information will be further discussed in Chap. 4.

It is worth mentioning also that another type of ground-based γ-ray detectors detecting Cherenkov radiation, i.e. the so called "water-Cherenkov" detectors (WCD, like HAWC). This type of instrument uses pools of water where the Cherenkov radiation is generated. They have a wider FoV, i.e. 1.5 str, but lower sensitivity than IACTs. As they do not require pointed observations, they can monitor a large number of sources, making them ideal for unbiased surveys.

The background for IACTs

As we already mentioned, one of the greatest challenges for VHE astronomy is to distinguish between γ-ray induced showers and the rest, i.e. the background, formed by particles

imitating γ-ray showers such as cosmic hadrons (mostly helium nuclei and protons), muons and cosmic electrons.

Hadrons are the most important component in the background contribution, as they are more numerous (about one thousand times) than γ rays.

Below $\sim$ 300 GeV, muons generating Cherenkov light produce images similar to the γ-ray ones. For this reason, it is very challenging to discriminate between muon showers and γ-ray showers. Indeed, at low energies we can say that muons are the irreducible component of IACTs background. The stereoscopic technique helps in eliminating the muonic component, allowing the study of low energy γ-ray showers.

Among background, one must also to take into account the night sky background (NSB), which has a big impact on the performance of IACTs. It is composed by light coming from the night sky, such as air glow[9], zodiacal light, starlight, man-made light, light from the Moon (see Fig 3.13).

[9]Light emitted by atoms and molecules in the upper atmosphere.

Figure 3.13: Summary of the main components of the total night sky background at high galactic and ecliptic latitudes: the Zodiacal Inter-Planetary Dust emission, Zodiacal scattered light, interstellar Galactic (cirrus) emission, starlight, atmospheric O_2 air glow and OH emissions in the near-IR, as well as the CMB, as indicated [114].

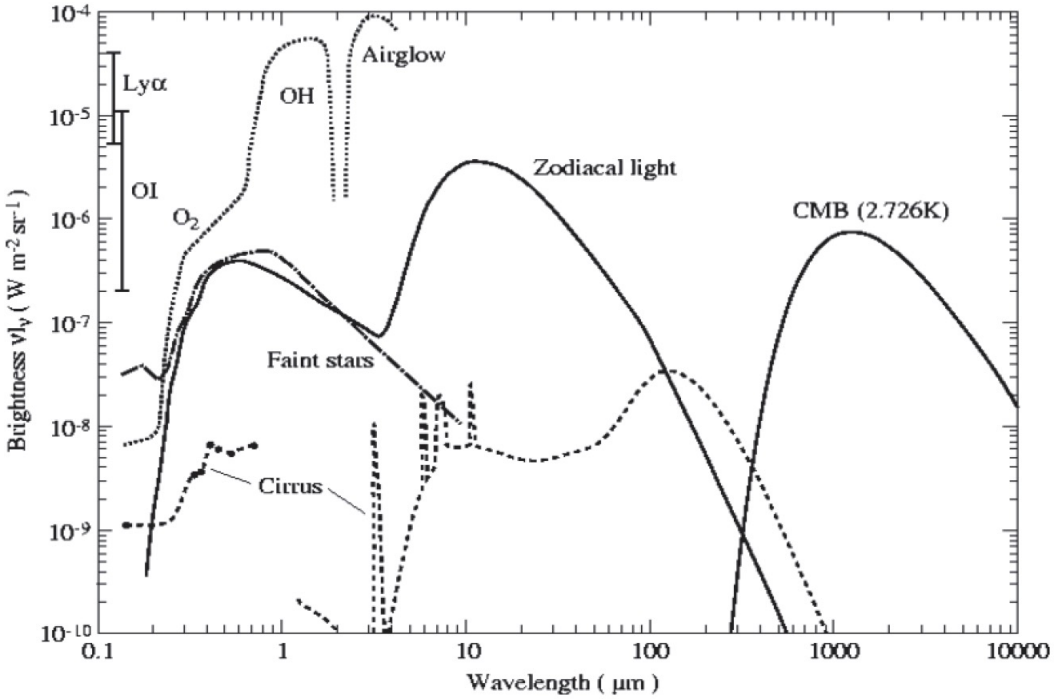

Chapter 4

The VERITAS observatory

4.1 The VERITAS array

4.1.1 Overview

VERITAS (**V**ery **E**nergetic **R**adiation **I**maging **T**elescope **A**rray **S**ystem) is a ground-based observatory that detects γ-ray photons with energies ranging from 85 GeV to 30 TeV. It is located at the Fred Lawrence Whipple observatory in southern Arizona (111° W and longitude 32° N) at an elevation of 1270 meters above the sea level (see Fig. 4.1).

Figure 4.1: The VERITAS array at the Fred Lawrence Whipple observatory in southern Arizona [115].

It is composed by four 12-meter telescopes that are spaced 100 meters apart, on average. Each telescope has a 3.5° FoV. Every telescope's reflector is made up of 350 hexagonal mirrors placed according to Davies-Cotton design [116], and the camera is made up of 499 photomultiplier tubes (PMTs)[1]. The sensitivity of the detector is such that a γ-ray point source with a flux of 1% the Crab Nebula can be detected within 25 hrs [49]. VERITAS can detect γ rays within the energy range of 85 GeV - 30 TeV, with an energy resolution of 15-25% for 1 TeV photon. The angular resolution (i.e. the PSF, defined as 68% containment radius) is about 0.1° for a 1 TeV photon [110]. The effective collection area, fot the same photon, is about $10^5 m^2$.

VERITAS has been fully operational since 2007, but it faced two main upgrades, which improved the efficiency of the VERITAS detection system: in 2009 the telescope T1 was moved

[1]PMTs have proved to be one of the best tools to detect Cherenkov light thanks for its fast response and high gain. Briefly, it consists of a glass box containing a photocathode, multiple dynodes and an anode. Incoming photons hit the photocathode which releases electrons due to the photoelectric effect. These electrons are then multiplied by the dynodes and then focused onto the anode, resulting into a detectable current.

to a new location, and in 2012 the camera's old photo-multiplier tubes were replaced with new ones with higher quantum performance. So we differentiate between epoch V4 (original configuration, 2007-2009), V5 (after T1 relocation but before PMT upgrade, 2009-2012) and V6 (after PMT upgrade, 2013-today). VERITAS observations are conducted at night throughout the year, but they are stopped from July to early September, due to monsoon season. Every year, approximately 1200 hours of good weather data are collected under dark and low illumination moonlight conditions (illumination less than 35%). However in 2012, VERITAS started taking data also under bright moonlight conditions (illumination 35% - 65%), resulting in an additional 200 hours of data in the annual VERITAS dataset. To do so under bright moon conditions, data is collected by running the camera's PMTs at lower high voltages (RHV), i.e. the voltage used in a PMT is 81% of the voltage used in normal operation.

4.1.2 The telescopes

Mechanical structure

Each VERITAS telescope structure is constituted by an altitude/azimuth positioner and a tubular steel optical support structure (OSS). The camera is mounted onto a quadrupod, and the camera load is balanced by counter-weights at the back of the OSS [115]. The reflector is mounted on the OSS as well and is composed by hexagonal mirrors. During regular operations, the positioner speed is $1^{\circ}s^{-1}$ but for safety reasons during operations its speed is slowed down to $0.3 - 0.5^{\circ}s^{-1}$. Its accuracy is of $\pm 0.01^{\circ}$. The telescope pointing information, which is controlled remotely, is passed to the database at a rate of 4Hz. The mechanical pointing accuracy of a VERITAS telescope is typically better than $\pm 0.01^{\circ}$.

Telescope reflector

Each VERITAS reflector follows the Davies-Cotton design [116]. Two of the advantages that the Davies-Cotton design brings in are the cheapness of having mirrors with identical focal length and having smaller off-axis aberrations compared to the ones obtained with the parabolic design. However, one of the disadvantages is that the photons hitting the camera arrive with a time-delay of few nanoseconds.

The reflector is made up of 350 similar hexagonal mirror facets (see Fig 4.3) made of glass and coated with anodized aluminium. Hexagonal shape was preferred over a circular one because it allows the mirrors to be closer/more packed to each other. The reflector has a 12 m mirror aperture and a total area of around 110 m^2. Within the Cherenkov light wavelength range, i.e. between 280 nm and 450 nm, the mirror reflectivity is 85%, with reflectivities usually $\geq$ 90% at 320 nm (see fig. 4.2).

Figure 4.2: VERITAS telescope reflectivity as function of the wavelength, from [117].

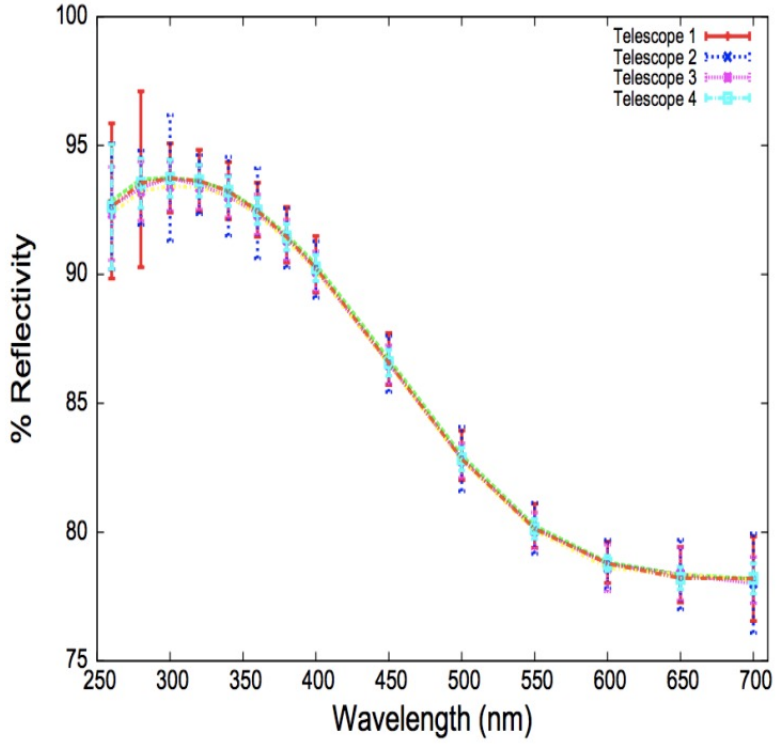

Mirrors are re-coated, checked and washed on a regular basis to maintain their high reflectivity [117], which may be affected by the dust of the Arizona desert. They are as well manually aligned (and the old ones even replaced) with adjustable nuts, so that the optical VERITAS PSF 80% containment radius[2] is less than $\sim 0.05°$ at operational elevations.

[2]PSF describes how the instrument detects a point-like source at infinity.

Figure 4.3: The 350 hexagonal mirrors on VERITAS reflector of one telescope.

Finally, the mirrors focus the collected image onto the camera, placed at the focal plane of the reflector, i.e. at 12 m from the mirrors.

Telescope camera

The camera consists of 499 UV-sensitive PMTs with a rise-time of 1.9 ns and a quantum efficiency of $\sim$ 20% at 320 nm (see Fig. 4.4). Originally the photon model used was Photonis XP2970/02, then upgraded in 2012 to Hamamatsu R10560-100-20 MOD, with higher (35%) quantum efficiency (see Fig. 4.5 for an image comparison of the two PMTs models).

Figure 4.4: VERITAS camera composed by 499 PMTs [110].

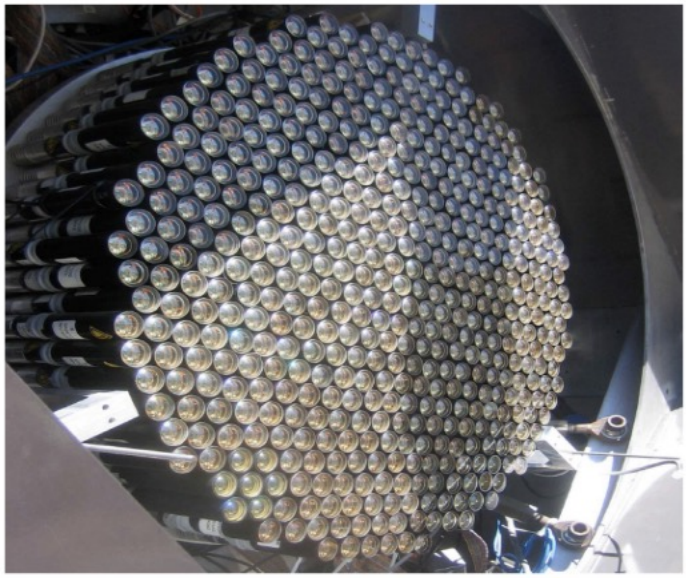

Figure 4.5: Photograph of the Photonis XP2970 PMT (right), replaced with the Hamamatsu R1056010020 (left) in 2012 [118].

The angular FoV of each pixel is 0.15°, for a total FoV of 3.5° per camera. A light concentrator is placed in front of each PMT, reducing dead space between them. It is composed by plastic cones called "Winston cones" (see Fig. 4.6), having the exit smaller than the entrance in order to concentrate the light on the center of the PMT photocatode, where it is more active.

Figure 4.6: An image of Winston cones.

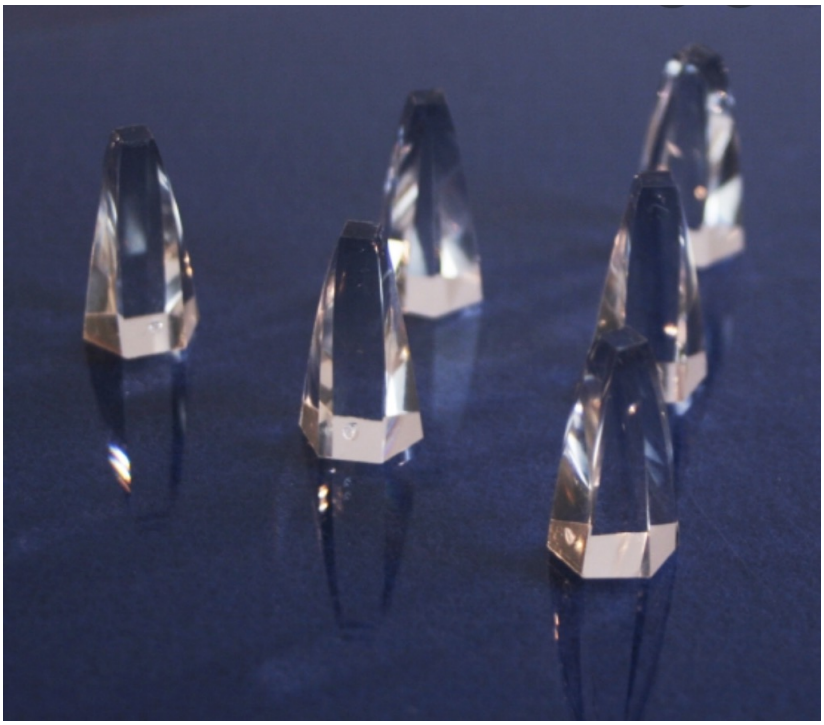

A voltage of about 700-800 V is supplied to each PMTs independently by a multi-channel power supply, resulting in a nominal gain of $\sim 2 \times 10^5$. A pre-amplifier built into the base of the PMTs provides an extra gain of 6.6 to the PMT signals [119]. This amplified signal is sent to the readout electronics via cable wires whose length is about 150 ft. Then a data acquisition system collects signals from the pre-amplifier and a trigger system starts to operate. This is explained in the next section.

In order to protect the PMTs from extremely bright events (natural or artificial), when the high voltage (HV) threshold is exceeded, it gets automatically switched off for that specific pixel. Typically during observations, the current is set between 4 to 8 μA. Finally,

to further protect the PMTs, the camera is covered by a water-tight and light-tight box with a shutter closed during daytime.

The trigger system

The VERITAS trigger system is designed to differentiate γ-ray initiated air showers light from night-sky-background noise (NSB). Also it helps both in maintaining as lower as possible the dead-time[3] and also in avoiding to overload the data storage. It is developed on a three-level scheme, as explained in [120]. Let's briefly explain how it works.

The first trigger/level (L1) is called the "pixel trigger", as it occurs at the pixel level. It consists of a constant fraction discriminator (CFD) operating for each PMT. It splits the output from the PMT into three components: the first one goes to a threshold discriminator (TD) which triggers when the PMT signal reaches some threshold voltage (around 45 mV); the second one is attenuated by some factor f[4] and the third one is inverted and delayed. These last two components go into a zero crossing discriminator (ZCD) which sums them up and finds the time when the combined signal reaches a threshold of given fraction of the total signal. The combination of TD and ZCD is called a constant fraction discriminator (CFD). So once the CFD is activated, it sends out a 10 ns logic output pulse which is given to level 2 of the trigger system, the camera-level (L2). In case the night sky noise rises for some external cause, a circuit rate feedback (RFB) is also included, which reduces timing jitter and stabilizes the CFD trigger [121].

L2 does trigger (i.e. it generates an output pulse) when at least three adjacent pixels exceed the L1 threshold within a coincidence time window of about 6 ns. In this way, L2 reduces

[3] Defined as the time during which no data is taken. Right now this is about 15%.

[4] f=0.76, i.e., the pulses are about 6 times smaller than for the high-gain readout.

the chance that triggers are generated by random night sky background event and/or PMT fluctuations.

The third and last level of the trigger system occurs at the array-level. It triggers when it receives L2 signals from multiple telescopes, in a short time window. As the signal must be transmitted via optical fibre cables from the telescope to the centrally located L3 system, a time delay between the different L2 signals occurs. To this type of delay, another one is also added, i.e. the one coming from the Cherenkov radiation hitting the telescopes at different times each. Of course, these delays are corrected by a pulse delay module (PDM), which pass the signals to the data acquisition system (DAQ) only if the delays occur within a time window of about 50 ns. To reject local muons, usually two or more telescopes within 50 ns (i.e. a stereoscopic view of the event) are needed. When the DAQ is triggered, no new triggers can be accepted during this time, resulting in a 10% dead time in the system for an L3 trigger rate of 250 Hz.

Bias curve

The "bias-curves" are used to estimate what are the best trigger conditions, such as low energy threshold, low NSB contribution and stable rates. This curve is obtained by observing a dark patch of the sky and adjusting the CFD voltage, i.e. the L2 and L3 are recorded as function of the CFD. As result, the optimal value of the CFD threshold is the one below which the rates are dominated by the NSB photons and above which are dominated by cosmic ray showers. One bias curve is shown in Fig. 4.7. For normal observation conditions, the CFD threshold level is about 45 mV (corresponding to approximately 4-5 photoelectrons). For observations with low-moonlight conditions, the CFD is about 65 mV. For moderate moonlight conditions (i.e. RHV) the CFD is 25 mV.

Figure 4.7: Bias curve example taken under dark sky conditions. It shows the trigger rates in dependence of the CFD threshold. The green, red, yellow and black points are respectively the different L2 trigger rates for the four telescope. The blue points represent the L3 rate.

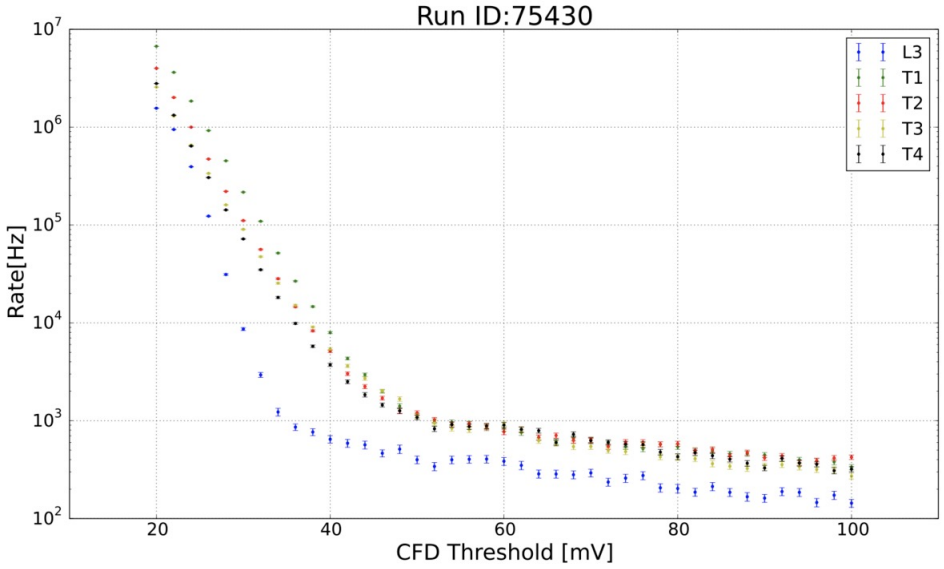

Data acquisition system

The analog electrical signal coming out from the L3 needs to be digitized. To do so, the data acquisition system (DAQ) operates at two levels: at telescope-level (i.e. L1) and at array-level (i.e. L3). At L1, each telescope uses a Flash-Analog-to-Digital converter board (FADC), shown in Fig. 4.8 [122].

Figure 4.8: An image of the FADC board.

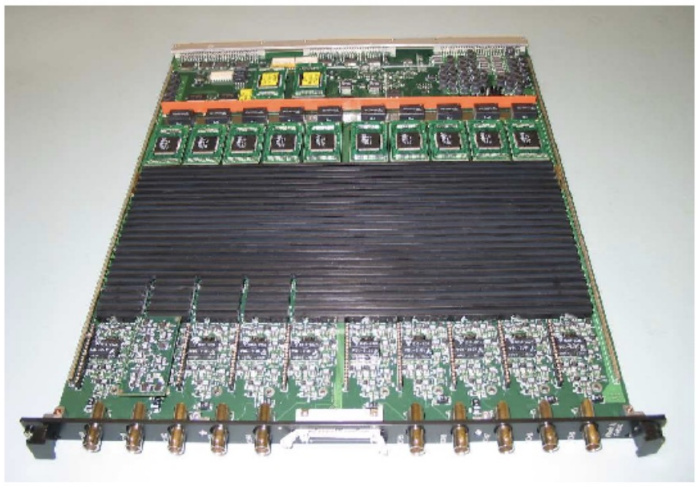

Each board has 10 channels, so for 499 PMTs it needs 50 boards. All the FADC boards are powered by four Virtual Machine Environment (VME) crates. There is also an extra one handling information such as event numbers and events. FADCs digitize continuously the analog PMT signal [123] at a rate of 500 MHz per second. On FADC two modes are available: high gain and low gain. It generally operates in high gain mode, but if the pulse exceeds the high gain range, then the signal is passed to the low gain channel, with a gain reduced by a factor of 6. A ring buffer stores the digitized signal with a memory depth of $32\mu s$ while awaiting the L3 trigger signal. When the L3 trigger signal is received by the FADC, the buffering process stops and the crates are "informed" about this so that they cannot receive further L3 signal. In the meantime, a segment (32 ns, 8 MB of memory buffer) of the FADC memory buffer is readout by the VME data acquisition system. Once the readout is completed, the crates are set again on "not-busy" mode and the next L3 signal is ready to be sent.

When the VME memory buffer is full in reading several events, it pass all these events to the "event builder" computer, which assembles them to form a telescope event file and write it on disk. This happens for all the telescopes at the same time. Consequently, the telescope event file is sent to the Harvester machine, which combines the event file from all 4 telescopes to form an array event. The array event file is archived and ready to be analysed in VBF format, i.e. VERITAS Bank Format, of about 12 GB size for a 30 min event. Then VERITAS members can get these data on the archive where the Harvester passed the data. This online database stores all the details of observations, such as L2 and L3 rates, dead-time histograms, coordinates tracking plots, NSB levels, FIR measurements[5] and even any observers comments. Also a data quality monitoring (DMQ) information is included in the database. DQM is taken every date after observations night. Fig. 4.9 shows a screenshot of the DQM database.

[5] A FIR is a far infrared camera mounted on top of the telescopes, to monitor the cloud condition by checking the changes in the temperature.

Figure 4.9: A screenshot of some DQM plots included in the database.

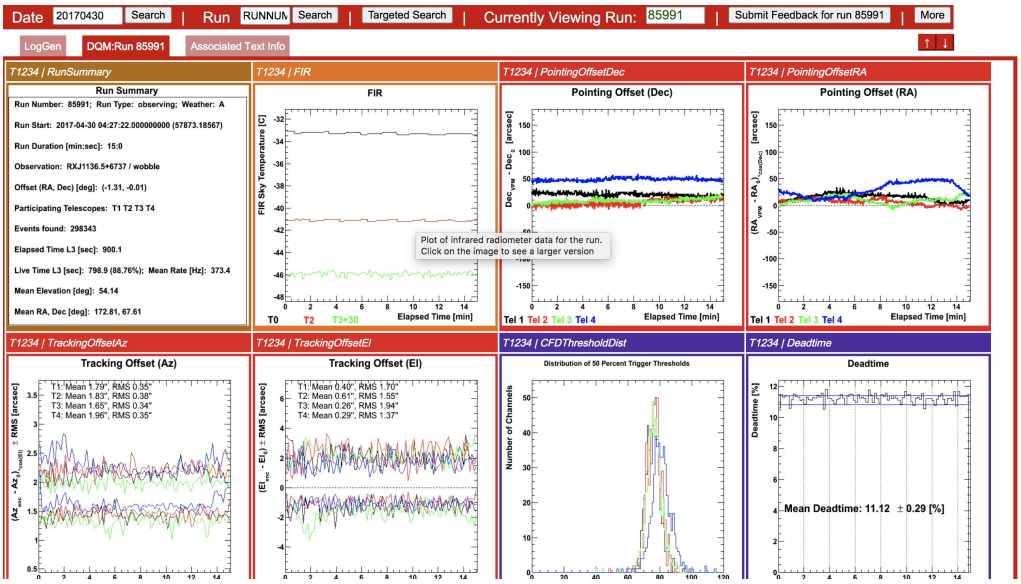

4.1.3 Calibrations

The calibration procedure is divided into two types: the absolute ones and relative ones. The absolute calibrations are performed every few months and they are used as input parameters for detector simulations to better model the detector response. Also, they are used to calculate the overall photon conversion factor[6]. This one depends on three parameters, i.e. the mirror reflectivity, the QE of the PMT and the correction factor of the electronic chain. The first two components are estimated in laboratories. The last component is calculated with a flasher system, which works in the following way. A light-emitting-diodes (LED) flasher system mounted on each telescope is used. It illuminates the

[6]The overall conversion factor converts FADC digital counts to photo-electrons (p.e.), which is directly proportional to the intensity of Cherenkov photons.

camera in a uniform and simultaneous way. In this way, the absolute gains in the camera are determined by measuring the position of the single photo-electron peak in the pulse-size spectrum, as explained in [124].

The relative calibrations, instead, measure channel-to-channel differences and are later used in data analysis. It assures that if a uniform light hitting on each camera pixel gives the same output response. Each night a 2-minute flasher run is used to quantify time differences and relative gains of the camera, allowing channel-to-channel variations to be measured. Time differences between channels are caused by cable of different lengths and electronic delays. It can be showed that the relative timing difference between pixels is not more than ± 2 ns for 99% of the channels. The relative gains measures the response of different pixels when exposed to the same light intensity. To get so, the PMT voltages are adjusted. These corrections are applied then to the data analysis.

In conclusion, it should also be mentioned that in addition to these calibration corrections, other corrections are applied too. For example, the FIR corrections. But it is also important to measure the pixel response to the current NSB condition. To do so, pedestal events are measured, i.e. events taken in absence of Cherenkov light representing the fluctuations in the PMT signal due to NSB. This is done by adding artificially a negative voltage offest (equivalent to 16 digital counts) to the PMT signal (see Fig. 4.10). The amount of charge deposited by pedestal event in each camera pixel is calculating by integrating the FADC trace over (usually) a 12 ns time window. During the observation process, these pedestal events are recorded when there is only NSB, and then during the offline analysis their contribution is estimated.

Figure 4.10: Example of FADC trace for a pedestal from a single PMT where there is only NSB.

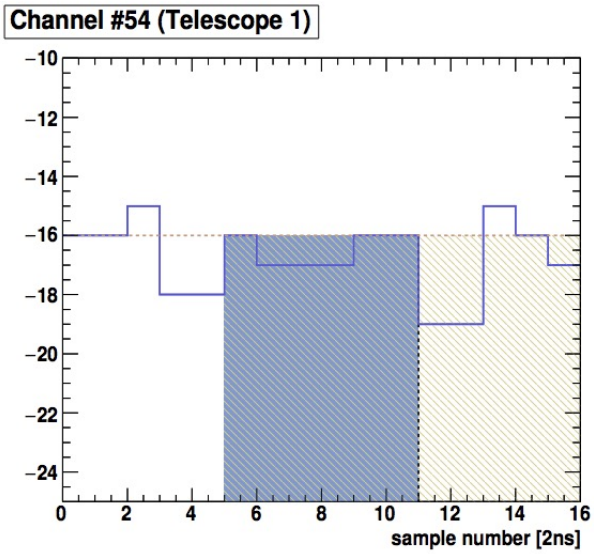

4.1.4 Data selection

Before analysing the archived data, it is necessary to filter them in order to select only the event files good/useful for the analysis. First, each data run[7] is assigned a flag indicating the quality of the weather during the night of its observation. Letter "A" indicates good weather, "B" acceptable weather with few thin moving clouds and "C/D"up to "F" indicate a very bad forecast condition, progressively, meaning the presence of thick clouds absorbing the Cherenkov radiation. Fig. 4.11 gives two examples of L3 rate plots, taking under two different weather conditions.

[7]Hereafter defined as single data even file.

Figure 4.11: Examples of L3 rate plots for the Crab: the one on the left was taken with weather condition "A", the one on the right with "C" condition, indicating the presence of clouds.

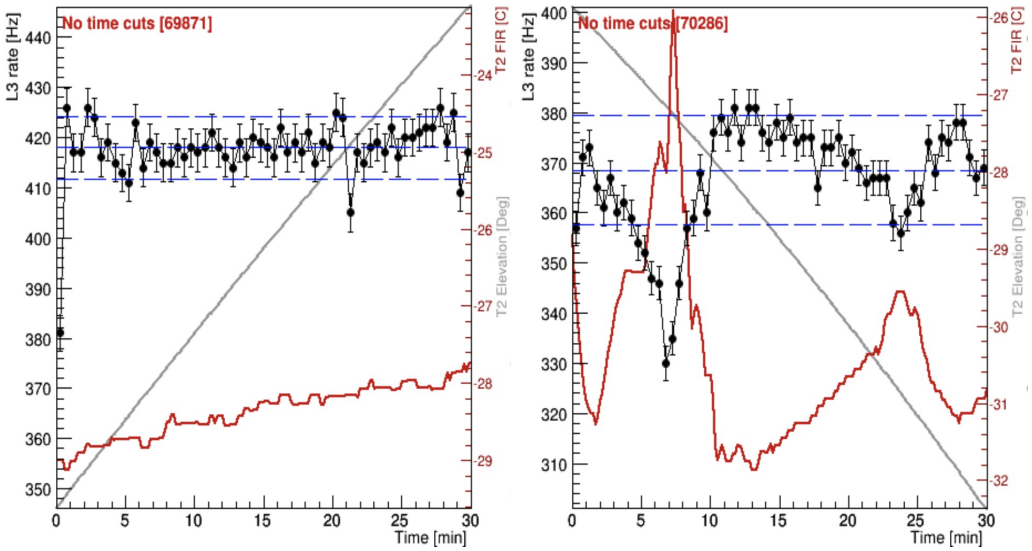

The weather assessment is supported by three FIR cameras mounted on T2, T3 telescopes and on another one (T0) pointing at the zenith. These monitor the temperature conditions, as mentioned earlier. In addition, there is as well a Light Detection And Ranging (LIDAR) system that records the vertical distribution of the clouds.

There are also flags indicating technical and/or external causes altering the quality of the data.

The majority of VERITAS observations take place on clear, dark nights. This provides about 750 hours of observation time per year. The majority of the observations are made in "wobble mode", meaning that the source is located 0.5° away from the camera center.

Wobble mode observations take data from both the signal region (ON region) and background regions (OFF regions) simultaneously, in order to minimize systematic and time-varying effects such as atmospheric changes [125]. The wobble positions are, then, shifted to another cardinal direction on the same source, or telescopes are pointed towards another source, after a typical run that lasts about 20 - 30 minutes. Observations are regularly performed while the Moon is above the horizon to maximize the service cycle of VERITAS. When compared to dark nights alone, this raises observation time by around 25%. The effect of the increased NSB and the possibility of PMT damage due to high currents are the main constraints for observations under moonlight. Under moonlight conditions, the NSB flux is highly variable: it depends on the angle between the moon and the telescope pointing position, on the moon phase and on the elevation.

When the Moon is above the horizon during low moon phases, there is almost no increase in average currents. As the Moon becomes brighter, the average currents increase and become more dependent on the Moon's elevation. When the currents become too high, no observations are carried out in order to preserve the instruments. VERITAS defines various operating modes based on the average currents in the cameras: from dark sky observations to a full moon pause.

4.2 VERITAS data analysis

4.2.1 MC simulations

In order to analyse the data, Monte Carlo (MC) simulations are needed. MC are in fact required to reconstruct the properties of the primary particle from the Cherenkov light detected and to produce the instrument response functions (IRFs, such as effective areas,

energy dispersion matrix, PSF..).

For this reason, the MC simulations are divided into two main steps: firstly, the creation and development of an air shower in the atmosphere is simulated and the CORSIKA package [112] is used to model it. The number of Cherenkov photons recorded depends on different variables: the energy of the primary particle, the angle of the hitting particle, the distance between the telescope and the incident particle's impact point and on the geomagnetic field. Thus, the showers are simulated by developing them over random azimuthal directions and covering a circular area on the ground of about 750 m. γ rays are the primary particles, with the energy ranging from 30 GeV to 200 TeV. The VERITAS site-specific parameters, such as altitude, geomagnetic field and telescope positions, are combined with two different atmospheric designs, one for summer and the other for winter. After the shower simulation, atmospheric extinction corrections, after they pass through the Earth's atmosphere, are applied to the Cherenkov photons too. Also, the air showers simulated cover a range of zenith angles from $0° - 65°$ and a range of azimuth angles from $0° - 360°$), i.e. the range that can be observed with the VERITAS telescopes.

As second step, the detector response function has to be simulated. To do so, the GrISU package[8] is used and it simulates two aspects of the detector: Cherenkov photon propagation through the optical system and camera and electronics response. The telescope geometrical properties are fully implemented, including mirror reflectivity, surface roughness, optical alignment and optical PSF. During the ray-tracing, the shadowing effects of the telescope structure are also taken into account, due to camera housing and quadrpod arms. The camera response is simulated too by considering the quantum efficiency of the PMTs and the collection efficiency of the light cones. Afterwards, the complete readout chain (i.e. PMT

[8] http://www.physics.utah.edu/gammaray/GrISU/

signal response, trigger system, FADC readout) is then simulated in the next step. The noise from NSB photons is simulated separately for different NSB conditions. The pattern trigger simulation starts with a simplified model of the CFD and ends with a full realization of the pattern trigger. The most common trigger threshold is 50 mV, which corresponds to roughly 4 - 5 photo-electrons. It's worth noting that, above the energy threshold, this simplified trigger model indicates good agreement between data and simulations. However, at low energy energies, the trigger caused by NSB photons plays a significant role and must be considered. The detector simulation's systematic uncertainty is estimated to be $\sim 15\%$. It is important to mention here that GrISU is used for V4 and V5 epochs IRFs. In fact, for V6 epoch, another simulation package is used to study the performance studies of the PMT upgrade, i.e. the CARE (CAmera and REadout) simulation package, developed by N. Otte[9]. After the simulations are completed, their output is written to disk in the VERITAS specific raw data format. They are, as well, analysed (and parametrized) in the same way as the real data (for image parametrization, see next Sec.). Their parameter values are, then, used to fill up the so called "look up tables", from which the energy and scaled parameters for the real γ-ray events can be estimated, as we can see later.

4.2.2 Image parametrization

In the first step of the analysis, the image parametrization is done. But before doing this, it is firstly determined the charge in each pixel by a trace analysis and after that the image cleaning is performed. Then, the image parametrization can be done.
Let's briefly discuss all these passages in order.

[9] http://www.gtlib.gatech.edu/pub/IACT/CARE.git

Trace analysis

The image of Cherenkov light due to a γ-ray shower (or cosmic ray) is done by recording the charge in each camera pixel. This charge is proportional to the number of hitting Cherenkov photons and it is obtained by integrating the recorded digital values of a FADC trace over a specific time window, usually 32 ns. The integrated charge is expressed in digital counts (d.c.). However, the real Cherenkov pulse lasts 8 - 10 ns. So, if we integrate over a longer time window, we may include the NSB component as well. For this reason, we should integrate the pulse over that portion of trace where the Cherenkov pulse is present, called the "signal window". This is done with the so-called "double-pass method" [10], which works in the following way [127].

[10] This method is implemented in one of the two VERITAS official analysis reconstruction software. In this case, I am referring to *EventDisplay* [126].

Figure 4.12: Typical FADC traces with a sampling rate of 500 Mega-samples per second, showing a PMT signal for a typical event. The shaded blue region shows the integration window.

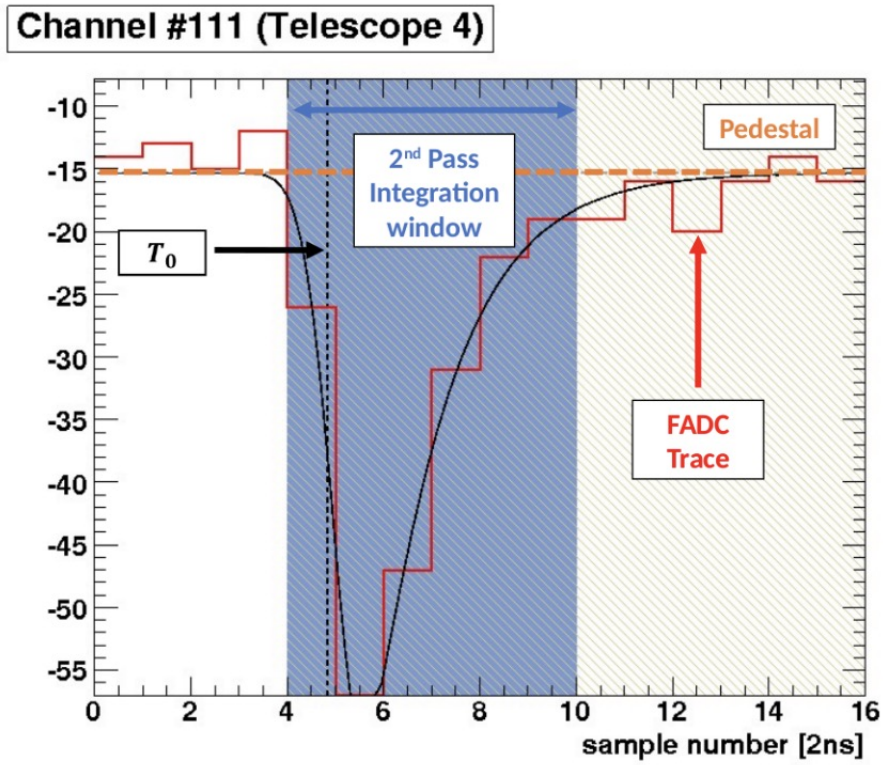

As first step, each FADC trace is given a large integration window (typically 10 samples, i.e. 20 ns) that is used to measure the charge and arrival time T_{zero}, which is defined as the time at which the pulse falls to half of its minimum value. It has to be noted that the start time of the integration window is different per each PMT channel along the image axis recorded in the camera. Indeed, as at smaller core distances, the Cherenkov photons emitted from the head of the shower arrive later than the ones emitted from

its tail. So a time gradient is generated. The resulting images are then cleaned and parametrized (see next sections about this). Then, the parametrized shower information are taken into consideration to determine the best location for the shorter (and second) integration window, usually of 6 samples (12 ns). Fig. 4.12 shows a typical FADC trace with the second shorter integration window highlighted. Then, a linear fit to the pulse arrival time as a function of position along the image axis is performed, and the slope of the fit is exactly the time gradient aforementioned (see Fig. 4.13).

Figure 4.13: Time gradient linear fit: arrival times per each pixel as function of position along the image axis.

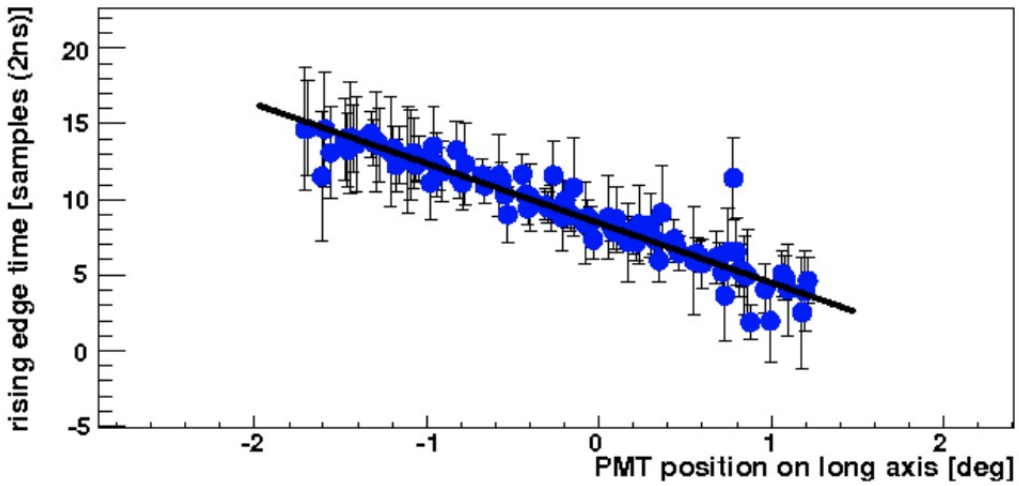

This is used to obtain a new T_{zero} per each pixel. This new T_{zero} is used as starting position of the second and shorter integration window. This method has the advantages of both increasing the signal-to-noise ratio and also preventing signal losses due to far showers.

Image cleaning

After determining the charge in each pixel, the image cleaning is performed. Its goal is to identify and remove/cut off all those pixels that do not contain Cherenkov light and that are dominated by NSB fluctuations. These cuts may be either fixed a priori or dependent on each pixel signal-to-noise ratio. For the image cleaning, the "pedvar" value, calculated during the calibration phase, is utilized. It is defined as the variance of the mean pedestal value, whose charge distribution is shown in Fig. 4.14. This pedvar value is proportional to the NSB (noise) level, as the pedestal events determine the pixel activity in the absence of Cherenkov light signals, as mentioned before.

Figure 4.14: Charge distribution of pedestals for Telescope 1, with an integration window of 6 samples. Here the mean pedestal value is 85.96, while the pedestal variance (pedvar) is 6.905.

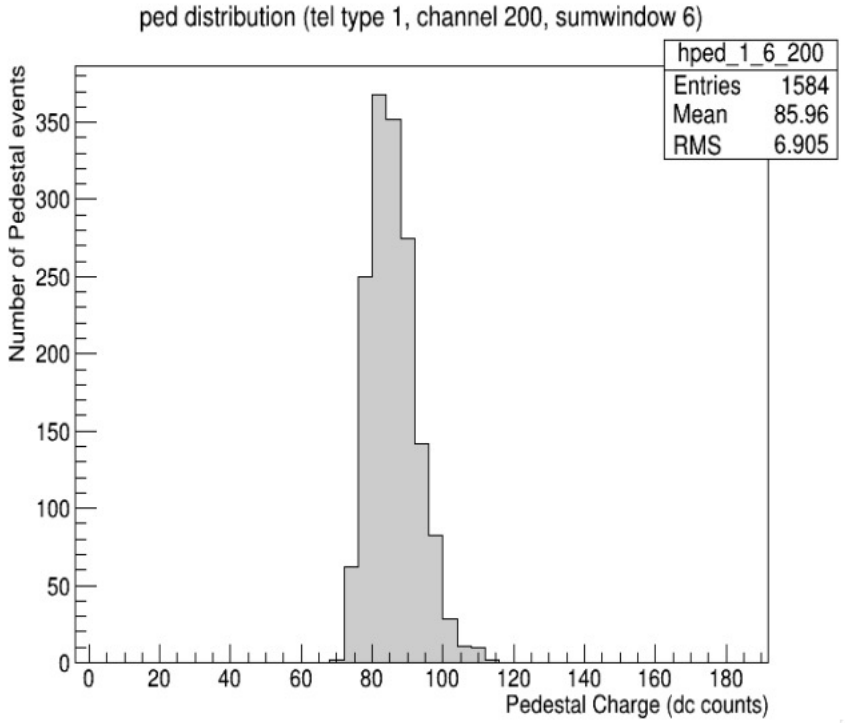

There are two steps to determine if a given pixel belongs to the shower image. In the first step, each pixel with a charge greater than 5 times its pedvar is selected and creates an image pixel. Afterwards, a lower cut value of 2.5 times the pedvar is used in the second step, imposing that at least one of the neighboring pixels has already been marked as an image pixel during the first step. If this cut is passed, the pixel becomes a "border pixel" for the shower image. If a picture pixel has no neighbors who have survived the cleaning process, it is removed. The image of the Cherenkov shower is then defined by the remaining

image and border pixels.

On the cleaned pixels/images, a moment analysis is performed to determine several parameters, such as distance, length size, width size and so on. Fig. 4.15 shows a representation of some of these parameters, explained later in Tab. 4.1. These parameters are used to determine, in turn, the brightness, the orientation, the position and the shape on the camera images. Moments are based on the position of the pixel in the camera and on the signal in it. Let's discuss them in the next section.

Figure 4.15: Representation of some shower image parameters.

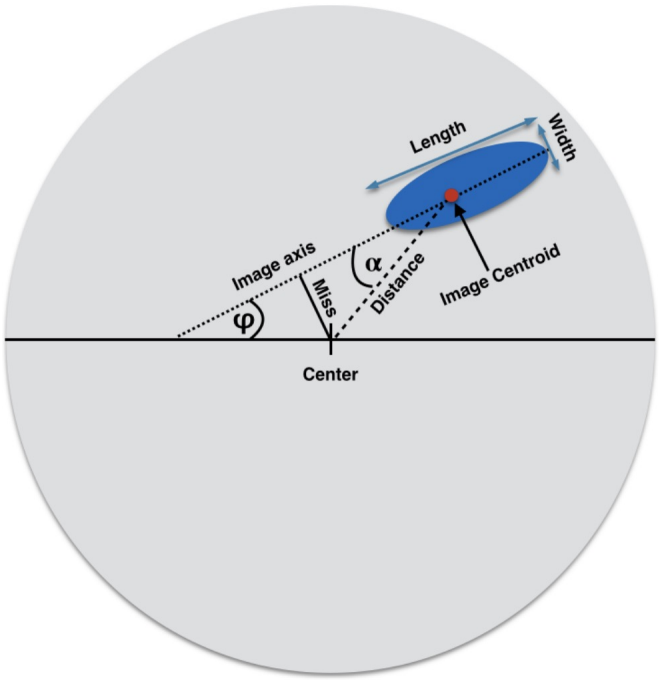

Image parametrization

Each image is parametrized after the shower images have been calibrated and cleaned. For the parametrization, the so-called "Hillas parameters" [107] are used. Hillas was the first one to propose to representation of the image in terms of some parameters, using a moment analysis [128]. The zeroth order moment gives the sum of digital counts of the elliptical image after the cleaning, i.e. its amplitude (or size). The first order moment provides the centre of gravity of the image in the focal plane of the camera. The second order moment describes the extension of the image. Table 4.1 lists and defines the main parameters.

Parameter	Definition
Size	Sum of integrated charge of all pixels (= total intensity of the image)
Width	The root mean squared (RMS) spread of charge deposit along the minor axis of the elliptical image
Length	The RMS spread of charge deposit along the major axis of the image
Centroid	Coordinates of the center of gravity of the image in the camera
Distance	The distance from the centroid of the image to the center of the FoV of the camera

Table 4.1: Main Hillas parameters that describe the orientation and shape of the image in the camera.

Since images at the camera's edge are difficult to recreate with this approach, they are normally left out of the study by considering events with a lower distance between the camera center and the image centroid or lowering the "loss parameter" (i.e., the fraction of the image contained in the edge pixels). A simple log-likelihood fitting algorithm is used to retrieve those truncated images at the camera's edge [126]. In general, for loss values

less than 50%, this log-likelihood reconstruction approach works well. As compared to the standard study, it results in a larger effective area at high energies.
At the end, the Hillas parameters are, in turn, used for the even reconstruction and discrimination. Let's discuss about it in the next section.

4.2.3 Event reconstruction

Geometrical reconstruction

Quality cuts are applied to the parametrized images, before the event reconstruction. These impose: a minimum number of image/border pixels, a minimum image size and a minimum number of telescope images. Afterwards, the stereoscopic method is used to reconstruct the arrival direction and the core location of each shower event [129, 130]. The basic idea of stereoscopic observation is that the major axis of the fitted ellipse maps the shower axis. So, major axes from multiple images can be superimposed and projected into a single and common camera plane coordinate scheme. From their point of interaction, the arrival direction of the shower can be determined. For N telescopes, there will be N(N-1)/2 intersection points, from which a single intersection point is found by doing a weighted average of them. The sine of the angle between two image axes, the size of the images, and the width-to-length (elongation) ratio for each image are used as weight, as defined by the following equation [129]:

$$weight_{1,2} = \left(\frac{1}{size_1} + \frac{1}{size_2}\right)^{-1} \times \left(\frac{width_1}{length_1} + \frac{width_2}{length_2}\right)^{-1} \times \sin(\theta_{1,2}. \qquad (4.1)$$

High-quality (i.e. brighter and longer) images pairs are given more weight in this way. The shower core location, defined as the point on the ground where the γ-ray photon

would hit if travelled directly to Earth without being absorbed by the atmosphere, is then determined, which is needed for energy reconstruction and gamma-hadron separation. This parameter is obtained by projecting multiple images in the shower plane coordinate system (the "ground" plane) and calculating the intersection point of the major axes. Then, the shower core location is then determined by the weighted average of all pairs of intersection points. Fig. 4.16 shows the stereoscopic approach just described. The so-called *impact parameter* is in this way calculated. It is the measurement of the distance from the shower core to a given telescope location within the shower plane coordinate system. As far away showers generate parallel images, angular resolution deteriorates as a function of the impact parameter. Hence, a cut on the impact parameter is applied to data.

The *emission height* of the shower, defined as the average emission height obtained by each pairwise combination of images, can be measured using the centroid of the images, the source location and the impact parameter [131]. The emission height can be used to reject poorly reconstructed showers and/or hadronic showers, as these ones can penetrate deeper into the atmosphere.

Figure 4.16: (Left) Reconstruction of the arrival direction of the shower, calculated by superimposing multiple camera images into a common camera coordinate system. (Right) Shower core position determination.

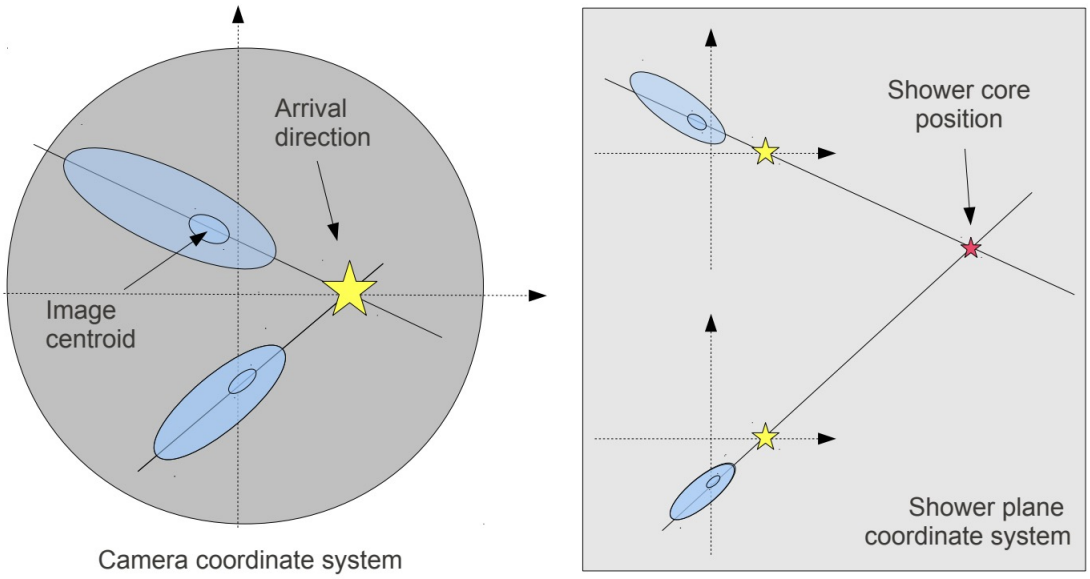

Energy reconstruction

The total charge contained in the telescope image (or size) depends on the amount of Cherenkov photons contained in the γ-ray-initiated air shower. Moreover, this size depends as well on the observing conditions, such as the shower direction (zenith, azimuth, wobble offset), the impact parameter and the NSB level.

The energy can be estimated via γ-ray MC simulations, generating the so-called "look-up tables", shown in Fig. 4.17. These tables contain the median and 90%-width (σ_E) values of the logarithm of the image size (such as, length and width) as a function of the primary γ-ray energy and of the impact parameter.

Figure 4.17: An example of lookup tables for the median (left) and the sigma value (right) used to estimate the energy of the reconstructed event (for a zenith angle of 20°).

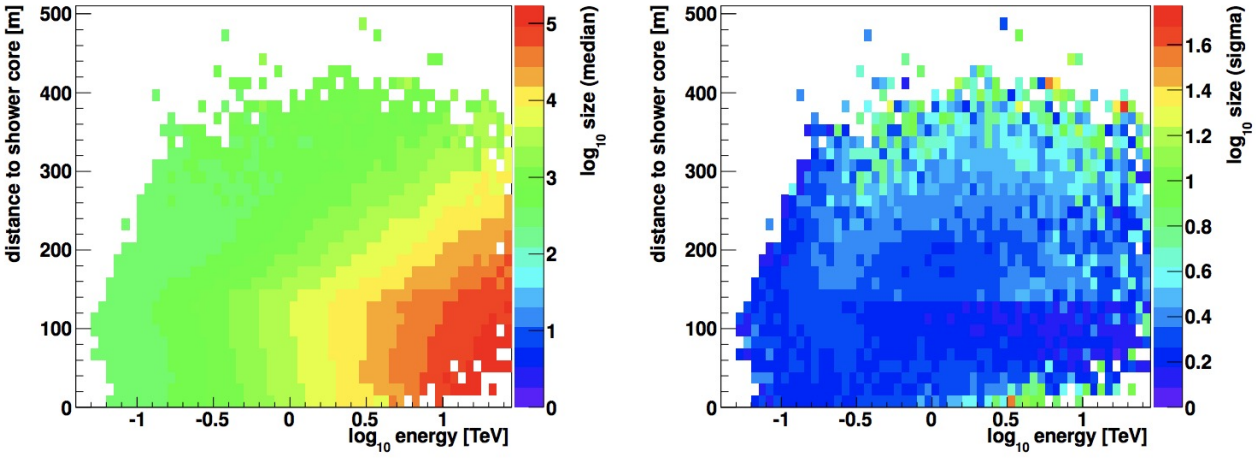

The energy of the event E_{event} is calculated by averaging the energy estimates of all N telescopes, weighted by $1/\sigma^2$, i.e.:

$$E_{event} = \frac{\sum_{i=1}^{N} \langle E_i \rangle / \langle \sigma_i \rangle^2}{\sum_{i=1}^{N} 1/\langle \sigma_i \rangle^2}. \tag{4.2}$$

where $\langle E_i \rangle$ is the median energy in a particular bin of the look up tables for telescope i, and $\langle \sigma_i \rangle$ is the 90% width in the energy distribution of that bin for telescope i. The estimated values are obtained by interpolating the results from different tables. This is done as the simulations are performed for specific steps of wobble offset, NSB level and zenith angle. Additionally, the χ^2-value of the energy estimation is derived:

$$\chi^2(E_{event}) = \frac{1}{N-1} \sum_{i=1}^{N} \left(\frac{E_{event} - E_i}{\sigma_i^2} \right), \tag{4.3}$$

which can be used afterwards to distinguish γ signal than background signal, as we will see in the next section.

4.2.4 Gamma-hadron separation

After the event reconstruction, it is necessary to separate the primary γ ray from the more numerous background events. This is done by applying cuts on the shape of the image and on the arrival direction of the events. Indeed, there is a consistent difference between the image shape of a γ-ray induced shower and the cosmic-ray one (as we saw in Chap. 3).

Shape parameters

The width and length parameters are very effective to reject cosmic-ray induced showers. Lookup tables (generated via on γ-ray MC simulations) are used because both parameters depend on different variables: the NSB level, the energy of the primary particle and the shower direction. To avoid this dependency, the actual length and width parameters are compared to the expected ones contained in the look up tables, i.e. the median and the 90%-width-values of the expected image width ($w_{MC}, \sigma_{width,MC}$) or length ($l_{MC}, \sigma_{length,MC}$), as a function of impact parameter (R) and the image size (s).
Thus, the new parameters mean-scaled length (MSCL) and mean-scaled width (MSCW) are obtained as:

$$MSCW = \frac{1}{N}\sum_{i=1}^{N}\Big(\frac{width_i - w_{MC}(R,s)}{\sigma_{width,MC}(R,s)}\Big), \tag{4.4}$$

$$MSCL = \frac{1}{N}\sum_{i=1}^{N}\Big(\frac{length_i - l_{MC}(R,s)}{\sigma_{length,MC}(R,s)}\Big), \tag{4.5}$$

where N is the number of telescopes, and $width_i$ and $length_i$ are respectively the width and length of the shower image in the ith telescope. From this, the mean-scaled parameters for γ-ray showers are distributed as Gaussian and peak on zero. On the contrary, the less compact and irregular background events are centered at greater mean-scaled values, as shown in Fig. 4.18.

Figure 4.18: Event distribution for ON events (black points) and OFF events (red points) of the Crab Nebula. See next section for ON/OFF regions definition.

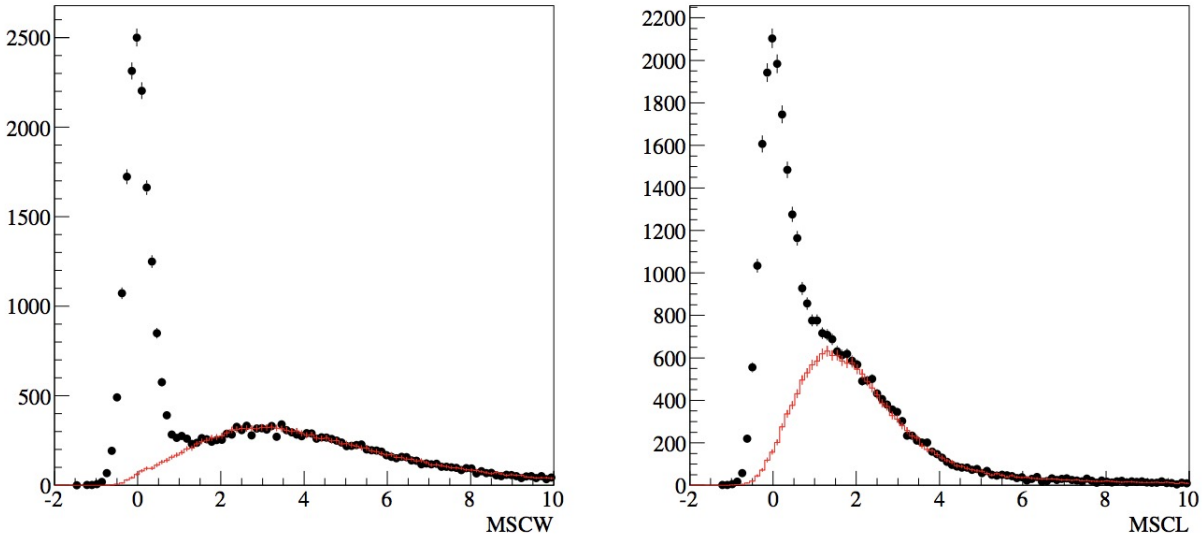

Hadronic showers have longer and broader images than γ-ray showers because they are less compact and erratic. As a result, the MSCW and MSCL primary distributions vary. The cut values for distinguishing background from signal events were calculated a priori by optimizing the sensitivity to detect a source with 5% of the Crab Nebula flux. This method produces three different types of cuts: "soft", "moderate" and "hard", referring to

the spectral hardness of the source they have been optimised for. In fact, soft cuts are optimised for source with a soft spectral, i.e. power-law index $\Gamma > 3.5$. They have a lower energy threshold and "looser" cuts allowing an increase of the signal (and the background as well) at lower energies. While hard cuts are optimised for hard spectrum sources with $\Gamma < 2.0$.

For a standard analysis, some other cuts are applied too, such as the size of the camera (all events with direction outside of this interval would be ignored), the distance of the core position to the telescopes, the second largest image size (which is used to distinguish among soft, moderate and hard cuts), the telescope multiplicity settings, the direction cut and the energy reconstruction cuts. Some of these cuts are listed in Tab. 4.2.

Cut parameter	Value
N_{tel}	$\geqslant 2$
Core distance	≤ 350 m
MSCW	-1.2 to 0.5
MSCL	-1.2 to 0.7

Table 4.2: Some of the quality cuts applied for a standard analysis.

In order to further reduce the hadronic cosmic-ray background, a gamma-hadron selection based on *Boosted Decision Trees* (BDT) [132] can be also applied. BDT is a multivariate technique used to differentiate between signal and background events, using machine learning algorithms. This type of selection gives improved sensitivity compared to the VERITAS standard analysis [132]. Then, trained BDT cuts are taken into consideration, additionally to the standard ones.

4.2.5 Signal extraction

After the reconstructed events have passed the stereo quality and gamma/hadron separation cuts, they are binned into a 2D histogram, the so-called skymap, obtained by converting the camera coordinates into sky coordinates.

However, it could happen that cosmic-ray showers are mistaken as γ rays (due to their similar MSCW and MSCL) and binned too. Thus, a cut on the arrival direction θ, which is the angle on the sky between the actual source location and its reconstructed position, is applied to eliminate the isotropic cosmic-ray background component. An ON region of radius of θ is then defined around the putative source (whose location is known a priori). For a standard point-like source analysis, a $\theta^2 = 0.008$ deg^2 is applied. Fig. 4.19 shows the distribution of events in the ON region and the distribution in the OFF regions (background regions), indicating the standard cut value on θ^2.

A remaining background component is still present though, event after the θ^2 cut. To estimate it, specific methods are used. Let's review some of them in the next section.

Figure 4.19: ON and OFF events distribution from the Crab Nebula. The red line indicates the source region events, the blue line the background events. The green line indicates the standard $\theta^2 = 0.008$ deg^2 applied in point-like source analyses.

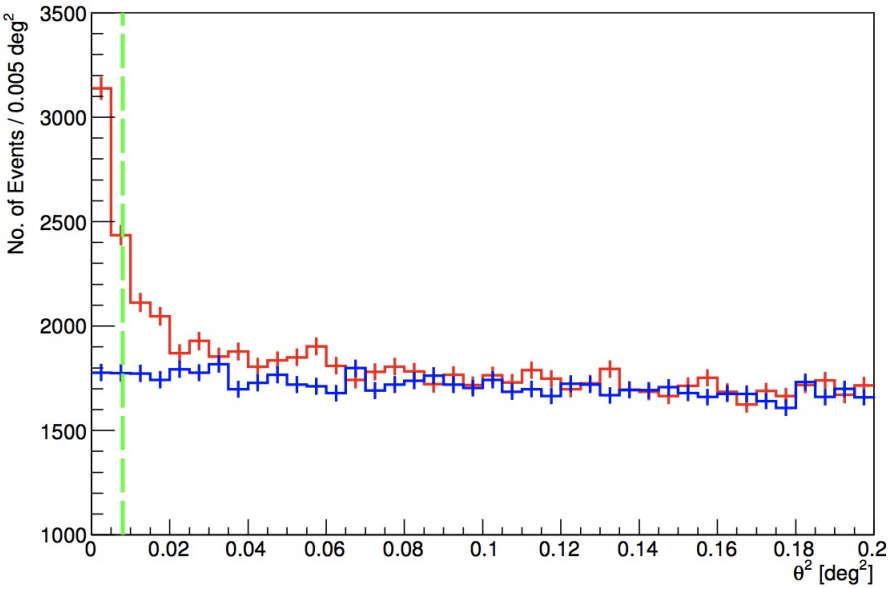

Estimation of the remaining background

The remaining background must be measured in order to evaluate the statistical excess of γ rays at the source position. To do so, OFF regions have to be defined, i.e. regions where to extract the background events. Two models are commonly used for defining the OFF regions: the reflected-region model and the ring-background model. Both background-region models are illustrated in Fig 4.20 [133].

Figure 4.20: This image shows two background estimation methods: the reflected-region model (on the left) and the ring-background model (on the right) [133].

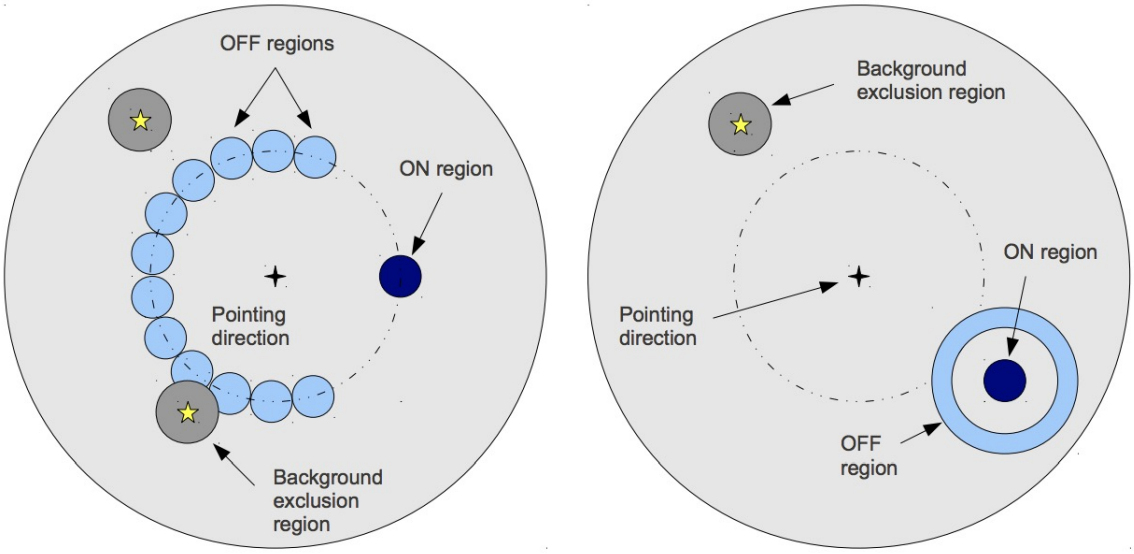

In the reflected-region (RE) technique, multiple circular regions (called OFF regions) of the same size as the ON region and equidistant from the pointing position are taken. One can use several OFF regions as long as they stay in the FoV, in order to prevent contamination from misreconstructed γ - rays. For this reason, this method cannot be used for extremely extended sources or if within the FoV there are too many other γ - rays sources. This model can be used in the "wobble mode" observations. W already saw that usually, for VERITAS observations, a wobble offset of 0.5 deg is used, with the direction alternating between North, South, East and West. An exclusion region is also defined around the already known sources (such as bright stars with magnitude brighter than 7), in order to prevent the leakage of γ rays into the OFF regions. A normalization parameter

is introduced, α, which takes into account the area of OFF regions compared to the ON area. Since the OFF and ON regions are both at the same distance from the camera center, no correction for relative camera acceptance is needed. The camera acceptance (see Fig. 4.21) deteriorates as the distance from the camera center increases, and it is believed to be symmetric in general.

Figure 4.21: Radial acceptance curve for the VERITAS camera, obtained from γ-ray like events (black cross) and proton MC simulations (red points). We assume that the acceptance in the camera is symmetric in azimuth.

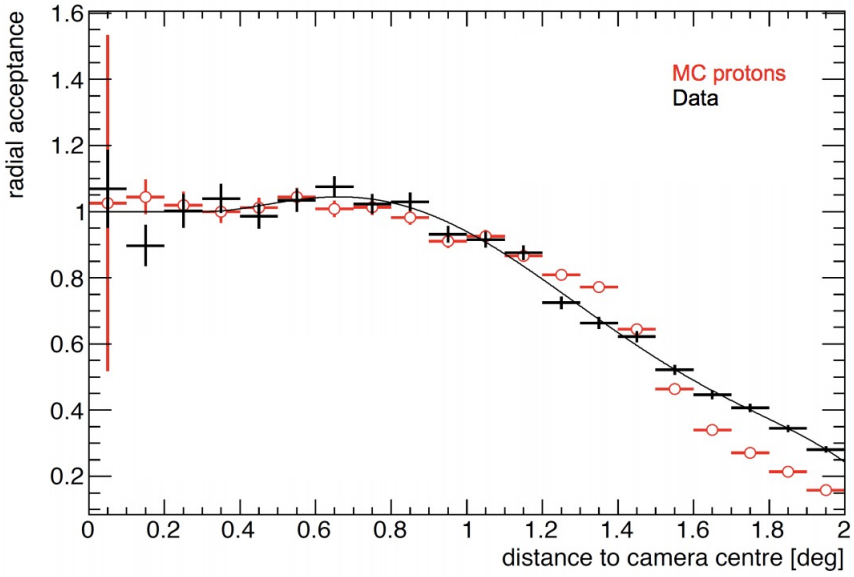

The OFF region in the ring-background model, instead, is characterized by a ring that surrounds the ON region. The ring radii have been selected such that the ON/OFF area ratio (α) is approximately 1:10. The area ratio is adjusted by the camera radial acceptance to give the normalization α. The radial acceptance curve is obtained by using γ-like events

or MC simulations. Also any part of the ring that overlaps with other known sources is excluded.

4.2.6 Source detection

Once N_{off} and N_{on}, i.e. the number of events in the (total) OFF and ON regions, respectively, are estimated, it is possible to calculate the statistical significance of a γ-ray source. The number of excess events is defined as:

$$N_{excess} = N_{on} - \alpha N_{off}. \tag{4.6}$$

The resulting significance of the signal is calculated using Eq. 17 of [134] and it is:

$$S = \sqrt{2}\Big\{ N_{on} ln\Big[\frac{1+\alpha}{\alpha}\Big(\frac{N_{on}}{N_{on}+N_{off}}\Big)\Big] + N_{off} ln\Big[(1+\alpha)\Big(\frac{N_{off}}{N_{on}+N_{off}}\Big)\Big]\Big\}^{1/2}. \tag{4.7}$$

The conventional criterion for claiming a detection of a γ-ray point-source requires S $\geqslant$ 5, which corresponds to a 99.9% probability that a signal is not from a random fluctuation in the background.

A significance skymap is then calculated by correlating the significance at each location of the skymap (an example is shown in Fig. 4.22). Also a significance distribution for all points of the skymap can be retrieved (see Fig. 4.23).

Figure 4.22: Example of skymap of the Crab Nebula in the sky coordinates.

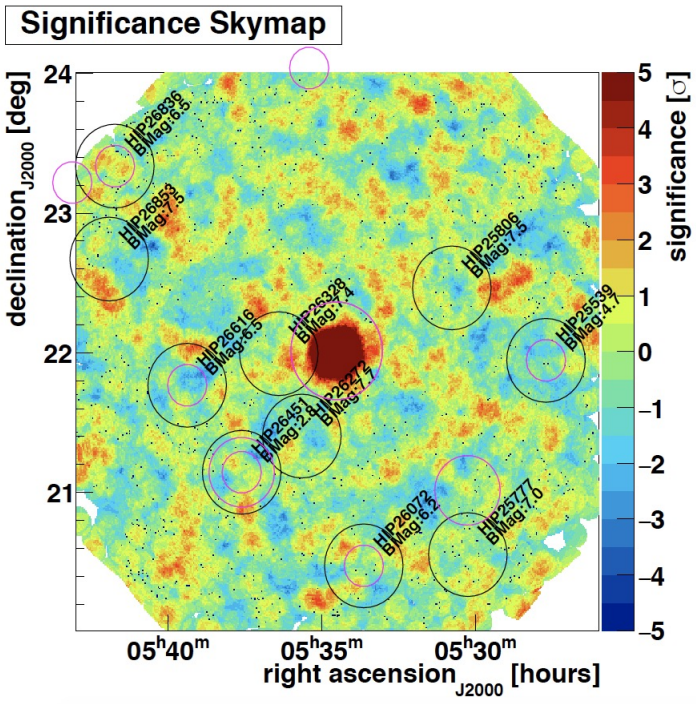

Figure 4.23: Example of significance distribution of the Crab Nebula. Red curve indicates the distribution taking into account the source region, the blue line, on the contrary, does not. The black line does not take into account the source region and the exclusion regions. The green line represents a Gaussian distribution.

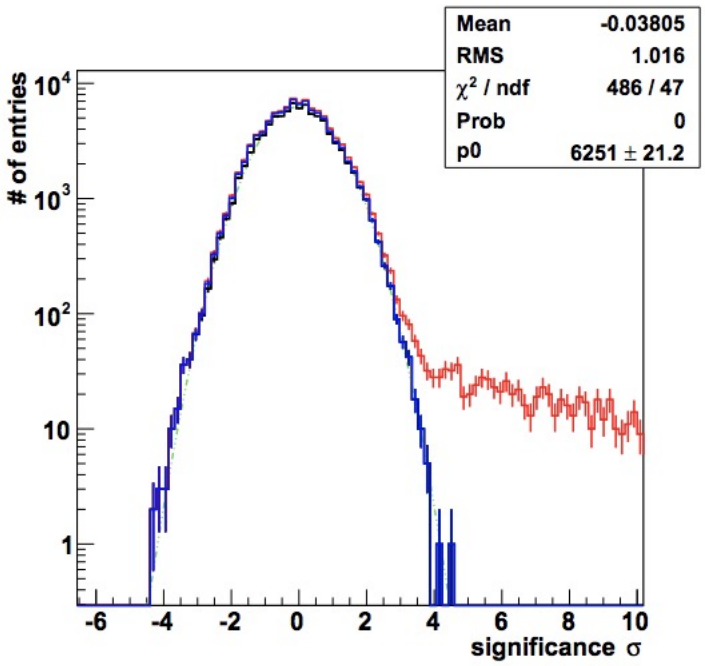

The excess events can be also transformed into a photon flux (or flux upper limit), i.e. the differential energy spectrum can be calculated. The use of quantities is essential is used to accomplish this: the effective area of the instrument and the total live time. This one is obtained by subtracting the dead time (already defined as the time during which no new event is recorded) from the actual observation time. About the effective area we are going to discuss in the next section.

4.2.7 Effective areas

The effective area defines the instrument ability to detect γ-rays. It is defined as the area over which hitting γ rays are recorded by the detector. We already saw that CORSIKA package produces MC simulations of γ-ray showers in the energy range of 30 GeV-250 TeV, over a radius of 750 m. And these simulations are used to calculate the effective areas, defined as:

$$A_{eff}(E) = \pi R^2 \frac{N_{selected}(E)}{N_{simulated}(E)}, \tag{4.8}$$

where πR^2 is the simulated area in the shower plane, on which the hitting particles are homogeneously distributed, $N_{selected}$ are the number of γ-rays that passes the selection cuts and $N_{simulated}$ is the number of γ-rays simulated.

The effective area is a function not only of the energy, but also of other observing parameters, such as the zenith and azimuth angles, the pointing offset from the source position, the NSB level, as well as the cuts used. The effective area is relatively flat and of the order of 10^5 m^2 at energies above about 1 TeV. It decreases dramatically at energies below 1 TeV, with a heavy dependency on the zenith angle. If the zenith angle increases, so does the energy threshold[11], because the emitted light must travel a much longer path through the atmosphere, and the likelihood of photons being absorbed is much greater than for low zenith angles. Thus, the intensity of Cherenkov light decreases and the detection threshold increases. Indeed low energy showers cannot trigger the telescope (let's recall that the trigger depends on the size of the image). Thus, to increase the sensitivity of the instrument for low-energy γ-ray showers, it would be worth it observing them at small zenith angles. Among large zenith angles (LZA) observation advantages, we could mention that at LZA,

[11] It is defined as the peak in the differential counting rate, assuming a spectrum like the one of the Crab Nebula.

larger pool of Cherenkov light is produced, thus increasing the effective area at LZA, as it can be understood from Fig. 4.24).

Figure 4.24: This illustration shows the effective area dependency on the zenith angle.

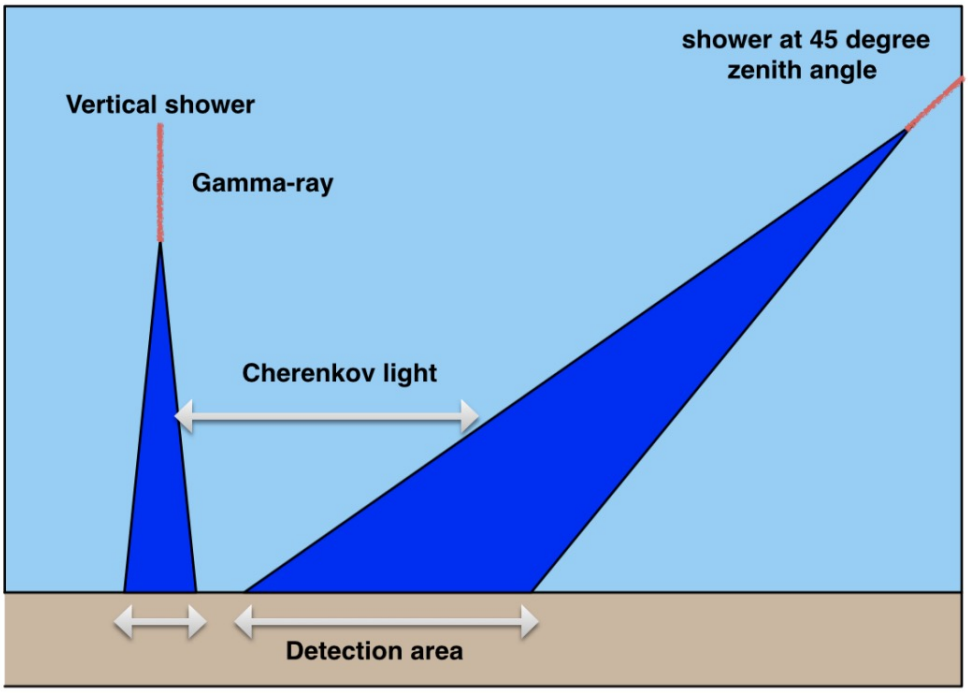

Effective area (EA) curves can be as function of either reconstructed energy or MC energy (for a fixed energy threshold). An example of EA plot is shown in Fig. 4.25.

Figure 4.25: Effective area curves, as a function of reconstructed energy, for different zenith angles (moderate cuts applied).

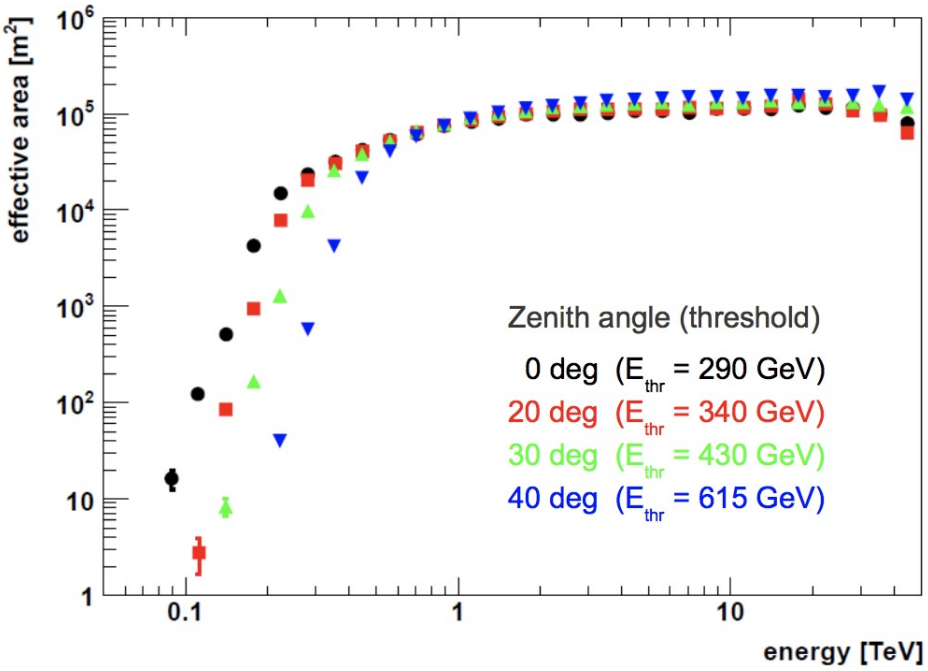

4.2.8 Flux determination

The effective area allows the count rate to be converted into a flux from a γ-ray source. The number of particles per unit area per unit time and per energy interval is known as the differential flux and is defined as:

$$\frac{dN(E)}{dE} = \frac{N_{excess}(E)}{A_{eff}(E)T_{live}dE}, \tag{4.9}$$

where $N_{excess} = N_{on} - \alpha N_{off}$, A_{eff} is the effective area of the instrument, T_{live} is the observation time (dead time already subtracted) and dE is the energy bin in which the flux is calculated[12]. By combining several observations, a time averaged differential spectrum of a γ-ray source is given by:

$$\frac{dN(E)}{dE} = \sum_{i=0}^{n} \frac{N^i_{excess}(E)}{\sum_{i=0}^{n} A^i_{eff}(E) T^i_{live} dE}, \tag{4.10}$$

where the sum runs over the observations runs n.

[12]The bin width must be at least the energy resolution of the instrument

Chapter 5

Gamma-ray signal from dSphs

As previously mentioned, dwarf spheroidal Galaxies (dSphs) are promising targets for indirect DM searches. They are objects with a radius of about 10^{19} m, quite nearby as most of them are within the viral radius of the MW (about 300 kpc). Their formation is still unclear, but numerical simulations are an important tool to further investigate on it. They offer the cleanest environment to look for γ-ray signal, as they also do not primarily host star formation regions, their stellar population is mostly populated by very old stars ("third stellar population") and are almost gas-free, in fact they have upper limits on gas mass lower than 1 $M_{\odot}$. They also lie at high Galactic latitudes which means they are not affected by the foreground coming from the Milky Way (see Fig. 5.1).

It is possible to infer the DM distributions contained in galaxies by studying the kinematics of gas and luminous stars. Using this method, it has been measured that dSphs are one of the most DM-dominated objects [5], being their mass-to-light ratios[1] about 30-50. Just as comparison, galaxies with radius of 10^{20} m have M/L ratio of about 4 - 10, while Galaxy clusters (radius of 10^{23} m) have the highest M/L ratios ever measured, i.e. about 80 -

[1] It is defined as the total mass divided by the luminous mass and it indicated the amount of DM contained within the galaxy.

900. DSphs are also very difficult to be detected as they appear to be faint and diffuse. However, in the past years, many new dSphs have been discovered and still some new ones will be detected, thanks to several sky surveys, such as Dark Energy survey (DES) [135], a wide-field optical imaging survey of the Southern Galactic hemisphere [136]. Even though so far no significant γ-ray excess has been detected from dSphs, it is essential to understand the content and spatial distribution of DM within dSphs, in order to put constraints on any particle theory predicting DM annihilation (or decay).

Figure 5.1: MW dSphs distribution in Galactic coordinates, as seen by Fermi-LAT in 4 years of operation [137].

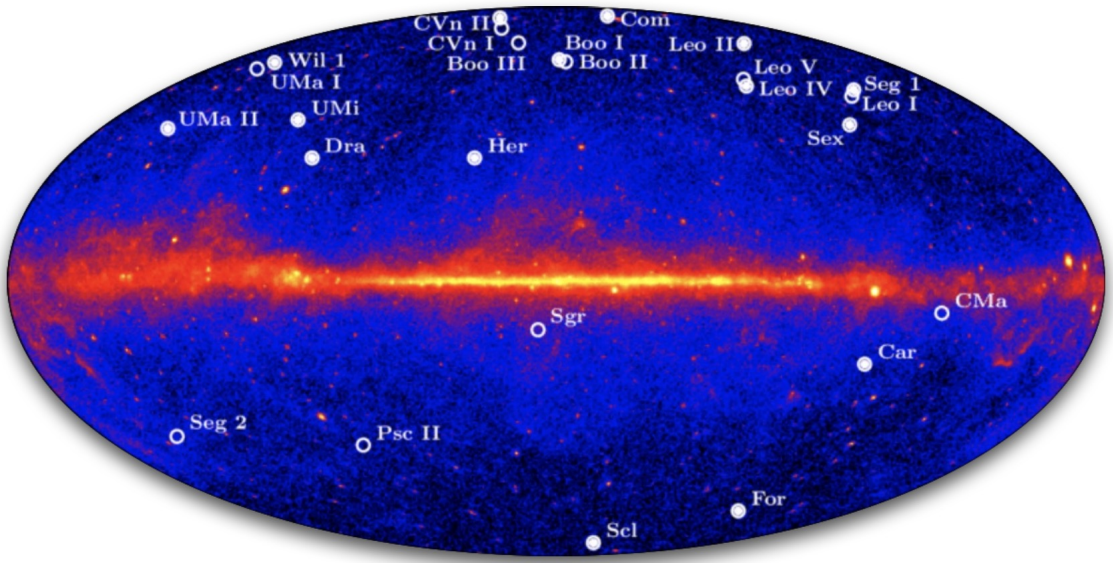

5.1 Dark matter annihilation flux from dSphs

The differential expected γ-ray flux (in γ m^{-2} s^{-1} GeV^{-1}) from DM annihilation can be defined as [138]:

$$\frac{d\Phi}{dE}(\Delta\Omega) = \underbrace{\frac{\langle\sigma_v\rangle}{8\pi M^2}}_{1^{st}\text{ term}} \underbrace{\sum_i B_i \frac{dN_{\gamma,i}}{dE}}_{2^{nd}\text{ term}} \times \underbrace{J(\Delta\Omega)}_{3^{rd}\text{ term}}. \tag{5.1}$$

It composed by three terms. The first one is the normalisation factor and it takes into account the annihilation cross section averaged over the velocity distribution $\langle\sigma_v\rangle$ and DM particle mass. The second term is the *particle physics factor*, including the differential spectrum of each annihilation channel per energy bin $\sum_i B_i \frac{dN_{\gamma,i}}{dE}$, where B_i is the branching ratio into a specific annihilation channel. The third term is the *astrophysical J factor* (or simply J-factor) and it gives us information on how DM is distributed within the source. In order to infer the J-factor, optical stellar-kinematic measurements are used such as the line-of-sight velocity and the position of stars potentially bound to the dSph [139] (see next section about it).

The J-factor is defined as:

$$J = \int\int \rho^2(l,\Omega) dl d\Omega, \tag{5.2}$$

where ρ is the DM density profile, l is the line of sight (l.o.s.) and Ω is the solid angle[2]. Different DM density profiles have been formulated (as we will see in Sec. 5.3) and some of which are identified in N-body numerical simulations. Current data sets do not provide strong upper constraints on the extent of DM halo, allowing emission to reach to an arbitrarily extended radius. Usually the most conservative choice when determining the truncation radius for the DM halo is to choose the outermost member star used to estimate

[2]Defined as $\Delta\Omega = 2\pi sin\theta d\theta$.

the velocity dispersion profile in the dSph. Moreover, due to our imperfect knowledge of the dwarfs and poorly constrained J factors for dSphs, many different realizations of halo J-profiles are consistent with the same kinematic data. This leads to systematic uncertainty on the calculation of cross-section upper limits [140].
But we will see all these details in the next sections.

Spectral signatures in DM annihilation

γ rays could carry important information about the nature of the DM particle, with some advantages. Propagating essentially unperturbed through the galaxy, they lead to distinctive spatial signatures; but an even more important aspect, as we will see, is the appearance of pronounced spectral signatures as well.
DM can annihilate (or decay) and the SM products can be leptons, quarks or bosons. These are called primary annihilation products. Such primary products can then produce γ rays (called secondary photons) through decay or hadronization, mainly through $\pi^0 \to \gamma\gamma$. The obtained γ-ray spectrum is referred to as the continuum (see Fig. 5.2). Additional γ rays may be added due to, e.g., inverse Compton scattering on starlight and the CMB of electron produced in e^-e^+ pairs. Electroweak and strong radiative corrections are another source of more low-energy photons.

Figure 5.2: γ-ray spectra from annihilation of DM with mass 1 TeV. γ-ray line is spread due to instrument PSF, assuming 100% branching ratio in that single channel [141].

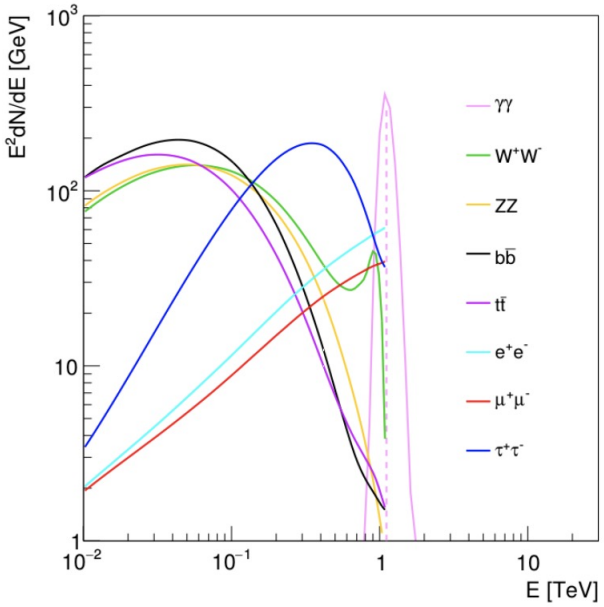

Moreover, a γ-ray line (called "monochromatic line") can be added to the photons continuum spectrum, when DM annihilates into γZ or $\gamma\gamma$ [142].

5.2 Modelling DM distributions within dSphs

In literature, different methods are used to determine the DM distributions (i.e. the J-factor) present within dSphs. These methods, of course, are based on theoretical principles, which we are going to discuss now in more detail.

Firstly, in order to determine the membership probability of stars to a specific dSph, the

color-magnitude diagram (CMD) is utilized [143][3]. In fact, if the stars lie on a specific position in the CMD, this means that they are more or less at the same distance, i.e. they belong to the same dSph. It has also been found out that dSphs contain several stellar populations with different ages, among which first stellar population stars, i.e. the ones that probably formed when galaxies began to build up in the early Universe [145, 146]. An example of CMD and sky position plot of stars identified as members of the same dSph (here Reticulum II) is shown in Fig. 5.3 [146].

Figure 5.3: On the left: an example of CMD of stars belonging to the dSph Reticulum II. On the right: the sky position plot of those stars [146].

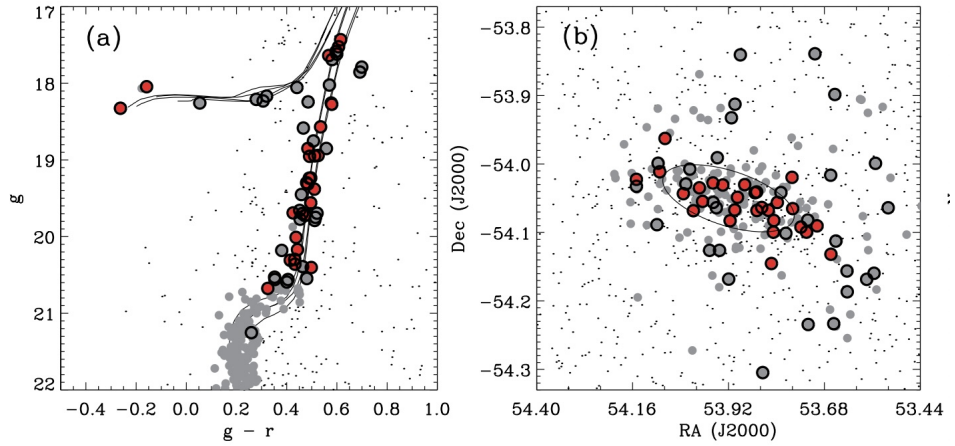

Secondly, in order to infer rotational velocities curves from dSphs, resolved stars measurements are performed, as the majority of dSphs lack of gas. These stellar kinematic measurements are obtained from three variables: the two dimensional projected positions

[3]The CMD is a scatter plot which shows observational data from stellar populations in terms of their luminosity and colour (i.e., surface temperature) [144].

and the one-dimensional line-of-sight velocities of resolved member stars, whose typical uncertainty is $\approx 1-2$ km/s. Differently, the tangential component of the velocity requires a precision of few km/s and the astrometric sensitivity of the current instruments is not good enough to resolve it. For nearly all dSphs, it can be showed that $v_{rot}/\sigma_{\parallel} < 1$, where $\sigma_{\parallel}$ is the measured line-of-sight velocity dispersion and v_{rot} is the rotational velocity. This means that dSphs are kept in equilibrium by the random motion of the stars. Moreover, the measured line-of-sight velocity dispersion $\sigma_{\parallel}$ has been measured to be in the range 3 - 10 km/s, with their luminosities varying between $L_{\star} \sim 10^3 - 10^7 L_{\odot}$. This leads to a total stellar mass in the range between $M_{\star} \sim 10^3 - 10^7 M_{\odot}$. An approximated estimate of the mass at the half-light radius, by measuring the velocity dispersion $\sigma_{\parallel}$ and the half-light radius r_h, can be obtained by the following relation, derived by the Jeans method [147]:

$$M \sim 4G^{-1}\sigma_{\parallel}^2 r_h. \tag{5.3}$$

For mostly all dSphs, it can be showed that[4] DM mass is much greater than the mass deduced in stars [148].

Everything we have just said makes the assumption that the stars present within the dSph are not influenced by the MW's DM halo potential. But how can we justify that? In order to give an answer to this question, let's first say that the best method to address this issue is via cosmological simulations. Indeed, one way to assess that would be by comparing the crossing time of stars present within the dSph with the orbital period of such dSph around the MW. If this latter timescale (which from simulations is about few Gyrs) is shorter than the orbital period, then the dSph could be modeled as a stellar system which is in

[4] Assuming that the system is spherically-symmetric and the velocity dispersion (as a function of the radius) is constant.

equilibrium in its own gravitational potential [148]. Unfortunately, current simulations do not have good enough resolution to measure the crossing time of stars. Thus, a dSph is considered as a system in a dynamical equilibrium if, in simulations, appear to have its inner parts (core) intact, differently than what may happen to its outer parts [149].
Now, with these theoretical principles in mind, let's discuss the different methods that are used to model the DM distributions within the dSphs.

5.2.1 Distribution function

Information on the kinematics of a stellar system can be deduced from the phase-space distribution f, one per each component, i.e. one for DM and the other one for the stars [148, 150]. Thus, if we assume spherical symmetry, the density is defined as:

$$\rho_\imath(r) = 4\pi \int f_\imath(r, \vec{v}) d^3\vec{v}, \tag{5.4}$$

where $f_\imath = f_{DM}$ for DM and $f_\imath = f_\star$ for the stellar component. The velocity dispersion for a component is:

$$\sigma^2_{\imath,\alpha}(r) \equiv \bar{v^2_{\imath,\alpha}} = \frac{1}{\rho_\imath(r)} \int v^2_\alpha f_\imath(r, \vec{v}) d^3\vec{v}, \tag{5.5}$$

where $\alpha = r, \theta, \phi$, the radial component is $\sigma^2_{\imath,r}$ and the tangential component is $\sigma^2_{\imath,t}(r) = \sigma^2_{\imath,\theta} + \sigma^2_{\imath,\phi}$ (with θ and ϕ are spherical coordinates).
The total gravitational potential Φ is the sum of the DM component and the stellar component. Each of those can be constructed numerically via the Poisson equation $\nabla^2\Phi_\imath = 4\pi G\rho_\imath$.
If we assume that the distribution function is isotropic, we can consider this as a function of the only energy E, i.e. $f_\imath(E)$ and we can link it to the density profile via the Eddington

formula, i.e.:

$$f_\imath(E) = \frac{\sqrt{2}}{4\pi^2}\frac{d}{dE}\int_E^0 \frac{d\rho_\imath}{d\Phi}\frac{d\Phi}{\sqrt{\Phi - E}}, \tag{5.6}$$

which implies that the phase-space distribution is uniquely determined, for a fixed model of stellar and DM density profile (i.e. given the potential of the system).

As only the stellar projected position and the line-of-sight velocity ($v_\parallel$) can be measured, the projection of Eq. 5.6 should be taken into consideration. Thus, we get:

$$\hat{f}(v_\parallel, R) = \int_R^{r_\parallel} \frac{rdr}{\sqrt{r^2 - R^2}} \int_{(1/2)v_\parallel^2 + \Phi(r)}^0 dE f(E), \tag{5.7}$$

where $2\Phi(r_\parallel) \equiv v_\parallel^2$ and R is the projected radius of the star. However, we would still need several inputs to calculate the stellar distribution function.

In order to infer information on the potentials that host the dSphs, simulations of dSph-like DM subhalos are generally performed [151]. The Einasto profile [47] (see Sec. 5.3.2) fits well these subhalos. In this way, for isotropic systems, it is possible to infer the shape of the distribution function in Eq. 5.7 by using the potentials of the DM subhalos. On the other hand, if we want to consider anisotropic systems, we would need as well to model the angular momentum and energy dependence of the distribution function.

5.2.2 Jeans modeling

As we have just seen, the stellar and DM distribution functions may depend on a complicated method to model DM distribution (as they may depend on both energy and angular momentum). Another simpler method that does not utilize any assumptions for the phase-space distributions of stars and DM, but instead that takes into consideration the moments of the phase-space distribution function can be used, i.e. the Jean modeling method.

As just seen, the phase-space distribution here is a 3D function, because with the current instruments it is possible to infer information only in just three dimensions, i.e. two spatial positions in the plane perpendicular to the line-of-sight and one dimensional velocity along the line-of-sight. Thus, the moments of the phase-space distribution used are the stellar density profile ν:

$$\nu(r) = \int f(\vec{r}, \vec{v}) d^3\vec{v}, \tag{5.8}$$

and the stellar velocity dispersion profile (in spherical coordinates):

$$\bar{v^2}(r) = \bar{v^2}_r(r) + \bar{v^2_\theta}(r) + \bar{v^2_\phi}(r) = \frac{1}{\nu(r)} \int v^2 f(\vec{r}, \vec{v}) d^3\vec{v}. \tag{5.9}$$

The spherical Jeans equation [152] links these two quantities and it reads as:

$$\frac{1}{\nu(r)} \frac{d[\nu(r)\bar{v}_r^2(r)]}{dr} + 2\frac{\beta_a(r)\bar{v}_r^2(r)}{r} = -\frac{d\Phi}{dr} = -\frac{GM(r)}{r^2}, \tag{5.10}$$

where:

$$\beta_a(r) \equiv 1 - \frac{2\bar{v}_\theta^2(r)}{\bar{v}_r^2(r)} \tag{5.11}$$

is defined as the orbital anisotropy and the enclosed mass profile is:

$$M(r) = 4\pi \int_0^r s^2 \rho(s) ds, \tag{5.12}$$

which includes contributions from the DM halo. As dSphs are predicted to be highly DM-dominated, the contribution of the stars in the enclosed mass in the galaxy is not that relevant and it can be neglected. The general solution of the Jean Eq. 5.10 is given by

[153]:

$$\nu(r)\bar{v}_r^2(r) = \frac{1}{f(r)}\int_r^\infty f(s)\nu(s)\frac{GM(s)}{s^2}ds, \tag{5.13}$$

with

$$f(r) = 2f(r_1)exp\Big[\int_{r_1}^{r}\beta_a(s)s^{-1}ds\Big]. \tag{5.14}$$

If we project along the line of sight the solution of Eq. 5.13, we get the following relation:

$$\sigma^2(R)\Sigma(R) = 2\int_R^\infty \Big(1-\beta_a(r)\frac{R^2}{r^2}\Big)\frac{\nu(r)\bar{v}_r^2(r)r}{\sqrt{r^2-R^2}}dr, \tag{5.15}$$

where $\Sigma(R)$ is the projected stellar density and $\sigma(R)$ the line-of-sight velocity dispersion [152], and they are both observed quantities. Then, Eq. 5.15 is fitted with observed velocity dispersion and projected stellar density (or surface brightness profile) to infer $\rho(r)$ and velocity anisotropy. To do so, the following assumptions are made: star distribution is described by the Plummer profile [154][5] (however, the stars make a negligible contribution to the gravitational potential); also the presence of any binary stars has no effect on the distribution of stellar velocities; the system must be in a dynamic equilibrium with spherical symmetry and β_a is constant.

It is important to mention that, for real galaxies, the aforementioned assumptions are not valid and that systematic errors may arise. For example, for real galaxies a cylindrical symmetry may be more appropriate. In fact, assuming a spherical symmetry in the Jeans equation leads to the so called mass-anisotropy degeneracy. This degeneracy exists between the assumed mass density and the velocity distribution of the system and this may lead to wrong mass estimates [155]. It is extremely important that it gets removed in order to

[5]The Plummer profile is a density profile used in N-body simulations of stellar systems, and it reads as $\rho \propto r^{-5}$.

properly identify DM structures and test the ΛCDM model. In the past years there have been several attempts to break this degeneracy, with significant yet not complete success [156, 157, 5, 158].

5.2.3 Orbit modeling

The orbit-based technique is used to reconstruct the potentials of dSphs. It does not require any a priori assumption on the orbital anisotropy nor on the distribution function [159]. It works in this way. Different orbits that sample the available phase-space in energy and angular momentum are generated. Assuming a potential model, the orbits of mock particles are tested. Each orbit has its own weight matching the photometry. Thus, the best fitting model, from the orbit distribution, is determined and the velocity anisotropy and the phase-space distribution are calculated. However, this technique requires expensive computational costs [160].

5.3 DM density profiles

There is a substantial diversity in density profiles describing the distribution of DM. During the past decades, cosmological large-scale N-body simulations have been a powerful tool successfully describing the formation and evolution of cosmic structures from initial over densities seeds. Now we are going to discuss into more detail some of the most utilized density profiles. All of them describe the mass density profile of a DM halo using a small number of parameters. Moreover, they assume a spherical symmetry, i.e. they do not take into account any perturbation due to interactions with the environment. This is a

good approximation especially for the inner parts of galaxy clusters and elliptical galaxies. Fig. 5.4 shows the most used ones that we are also going to describe in the following.

5.3.1 General Zhao DM profile

One of the most adopted density profile used to describe DM distribution is the so called Zhao profiles general family [161, 162]. It is described by three slope parameters (α, β, γ). Fixing these, it is possible to get one specific DM profile among the wide Zhao profiles general family (as described in the next subsections). This DM density profile is defined by the following double power-law relation:

$$\rho(r) = \frac{\rho_s}{(r/r_s)^{\gamma}[1+\rho_s(r/r_s)^{\alpha}]^{(\beta-\gamma)/\alpha}}, \tag{5.16}$$

where r_s the scale radius[6], γ is the inner slope while β the outer slope, α is the transition slope and $\rho_s = \rho(r_s)2^{(\beta-\gamma)/\alpha}$ is the normalisation.

As said, this model includes different well-known cases, which some of them are: the Schuster-Plummer sphere [163], the Jaffe model [164], the Hernquist model [162], the Moore profile and the most used one, i.e. the Navarro-Frenk-White (NFW) profile.

The Navarro-Frenk-White profile

The NFW density profile is defined as:

$$\rho_{NFW} = \frac{\rho_s}{r/r_s(1+r/r_s)^2}, \tag{5.17}$$

[6]Usually it is defined as the radius for which the logarithmic slope of the mass density profile is -2.

where $\rho_s = 4\rho_{NFW}(r_s)$ is the scale density. As stated in [165], the physical origin of this density profiled has not been fully explained.

The NFW halo mass can be calculated via the following relation:

$$M(r_{max}) = 4\pi \int_0^{r_{max}} \rho_{NFW}(r) r^2 dr = 4\pi\rho_s r_s^3 \Big(\ln\Big(1 + \frac{r_{max}}{r_s}\Big) - \frac{r_{max}}{r_{max} + r_s} \Big), \qquad (5.18)$$

where r_{max} is approximately the radius at which the halo is in virial equilibrium. Usually it is $r_{max} = r_{200}$. For this work, we adopted NFW parameters to calculate J-profile values (see Chap. 6).

Figure 5.4: This plot shows the most commonly used DM density profiles, normalized to a local density of $\rho_\odot = 0.3$ GeV/cm^3 at $r_\odot = 8.3$ kpc from the Galactic Centre. It is taken from [141]. The distributions are

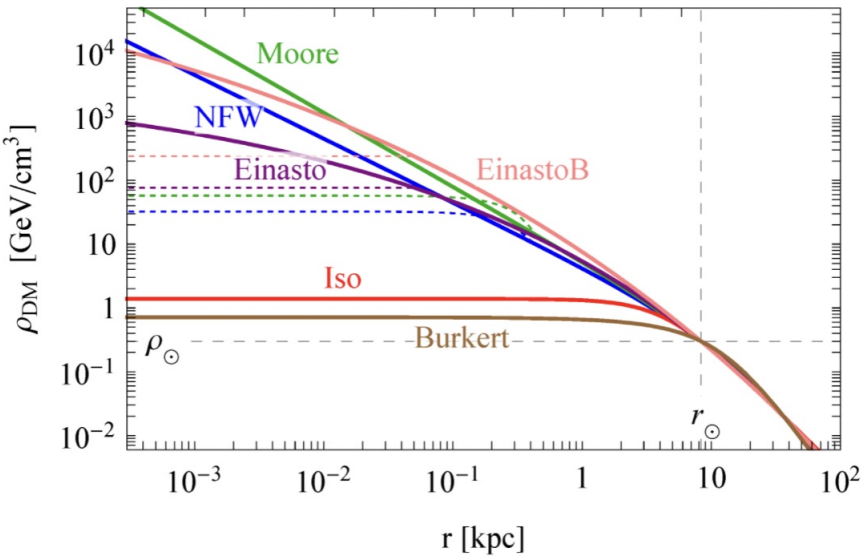

The Moore profile

The Moore profile is defined as [166]:

$$\rho(r) = \frac{\rho_s}{(r/r_s)^{3/2}[1+\rho_s(r/r_s)^{3/2}]}. \tag{5.19}$$

At large distances, it behaves as the NFW profile. However, it has a steeper slope than NFW towards the center of the DM halo.

5.3.2 Einasto

In 2004, Einasto introduced the following fitting formula for the density profile of DM halos [167], i.e.:

$$\ln\left(\frac{\rho_E(r)}{\rho_s}\right) = -\frac{2}{\beta}\left[\left(\frac{r}{r_s}\right)^{\beta} - 1\right] \tag{5.20}$$

where the third additional parameter, β, is called "shape parameter". The Einasto profile has been found to fit well highly resolved N-body simulations of DM halos [168].

5.3.3 The pseudo-isothermal elliptical mass profile

This DM density profile was introduced by [169] and it is defined as:

$$\rho(r) = \frac{\rho_s}{1+(r/r_s)^2(1+(r/r_c)^2)^n}, \tag{5.21}$$

with r_s being the scale radius of the halo core and r_c the cut-off radius truncating the halo mass density. Moreover, usually it has n=1. This profile is mostly used to constrain DM halos of elliptical galaxies.

5.3.4 The Jaffe profile

This DM density profile is mostly used for galaxy-scale DM halos. It described by the following relation [164]:

$$\rho(r) = \frac{\rho_s}{(r/r_s)^2(1+(r/r_s)^2)}. \tag{5.22}$$

If $r \ll r_s$, the density is steeper than the Moore profile and it has a cuspy core.

5.3.5 Burkert profile

Burkert density profile for DM halo [170] is defined by the following functional form:

$$\rho = \frac{\rho_s}{(1+r/r_s)[1+(r/r_s)^2]}. \tag{5.23}$$

This is a phenomenological formula, providing a good fit to the observed data to less than the virial radius. But, it is not valid for large distances from the galactic center. This profile converges to the NFW profile for $r > 0.3 \times r_{vir}$. However, the Burkert profile is not theoretically motivated and it remains just a phenomenological approach to face the DM problem.

5.4 Dwarf Spheroidal galaxies: extended sources

Considering the spatial extent of dSphs may provide additional information to increase the signal-to-noise ratio. This is, precisely, the goal of this thesis. But to do so, it would be necessary to quantify how (and if) γ-ray telescopes could resolve the extension of dSphs DM halo. Thus, the point spread function of the instrument (in this case, IACTs) should

be compared to the annihilation (or decay) emission profile. We took into consideration the study carried out by [171]. They calculated the J-profile for 20 dSphs galaxies obtained using a data-driven Jeans analysis of kinematic stellar data. To describe the DM density distribution, they used the general Zhao profile (already presented by Eq. 5.3.1), while to describe the stellar distribution, the Plummer profile was used. Moreover, they assumed a spherical symmetry and dynamic equilibrium for the dSphs, and a constant velocity anisotropy profile, whose parametrization is obtained from simulated halos, was, as well, assumed.

The J-profile, already defined in its differential form by Eq. 5.2, is calculated up to $\theta_{max} = \arcsin(r_{max}/D)$, where r_{max} is the distance from the dSph center up to the outermost star member belonging to the dSph, and D is the distance from the Earth to the galaxy. So if we integrate the J-profile up to θ_{max}, we can get the total DM flux expected from the halo. Fig 5.5 shows the annihilation J-profile integrated up to θ_{max} for each dSph.

Figure 5.5: Annihilation J-profile integrated up to θ_{max}. Bars indicate the 1σ range based on the kinematic analysis [171].

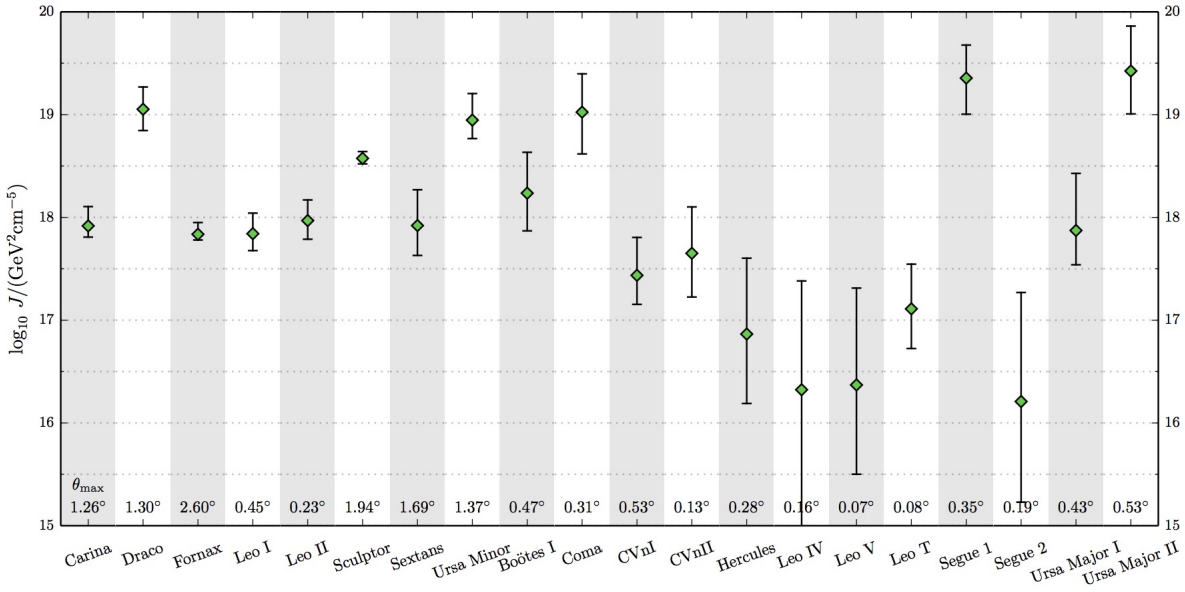

The authors, then, calculated, per each dSph, the containment fraction, defined as $J(\theta)/J(\theta_{max})$, where $J(\theta)$ is the J-factor integrated over the solid angle $d\Omega$ out to the truncation radius (about which we are going to talk in the next section). Lastly, they compared it to the PSF [7] of IACTs and Fermi-LAT, at different energies.

[7] Let's recall that the containment fraction of the PSF is the probability that a γ ray can be reconstructed within an angle θ of its true origin.

Figure 5.6: Comparing the PSF of IACTs, at different energies, to the containment fraction (cf) for annihilation, defined as $J(\theta)/J(\theta_{max})$. The x-axis is the angular distance from the center of each dSphs (in degrees) up to θ_{max} for each dSph. The dotted black line is the median value of the cf and the grey shaded band is the 16^{th} and 84^{th} percentile at each angle. Different colours correspond to different energies of the Fermi-LAT PSF, as labeled in the image. The PSF of a typical IACT (like VERITAS), defined as 68% containment of 0.1°, is represented by the dashed orange line. Image from [171].

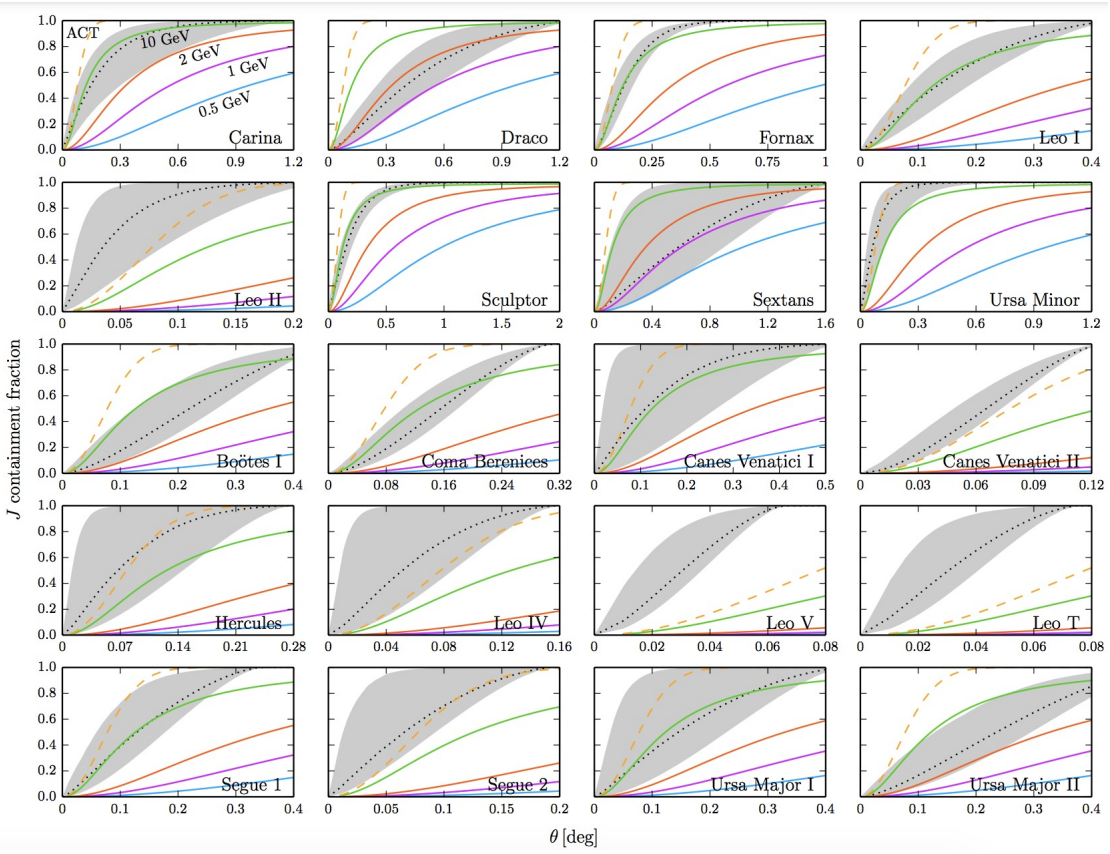

Fig. 5.6 shows this comparison. It is clear that for many classical dSphs (i.e. the ones with the best-measured stellar kinematics to date, like Fornax, Draco etc.), IACTs should

have enough resolution to detect extended DM emission from them, if there is any. Similarly for some ultra-faint dSphs (i.e. containing only a few tens of bright stars), like Bootes and Ursa Major II.

5.4.1 Truncation radius in dSphs

For all dSphs, the model of an isothermal sphere, described by a single power law, i.e. $\rho(r) \propto r^{-2}$, fits well the kinematics of dSphs [172]. From Eq. 5.17, it can also be deducted that the annihilation rate would drop rapidly at galactocentric distances $r \gg r_s$, where r_s is the so-called scale radius, i.e. the radius at which the transition between two power-law components: from an inner logarithmic slope to outer logarithmic slope. Within the scale radius, the emission depends on the slope of the inner density profile. However, the current kinematic datasets do not allow to put constraints on the scale radius estimation. In this way, the emission may extend up to an arbitrary radius. Thus, it is important to avoid that outer parts of the halo dominate the calculation of the integrated J-factor.

One of the most conservative choices for the truncation radius is to set it up to the distance of the outermost star member of the galaxy, and there are different ways to study it. In [171], for example, they did use the whole distribution of projected radii of the kinematic sample to estimate the r_{max}. They assumed a spherical symmetry to calculate the probability distribution for the unprojected distance up to the outermost observed star, having measured the projected distances to the observed stars. To do so, they started considering a single star. Then, they normalized the probability that its line-of-sight distance relative to the halo center (z) to be proportional to the unprojected Plummer density profile, which is:

$$P(z|R) \propto \left(1 + \frac{z^2 + R^2}{R_e^2}\right)^{-5/2}, \tag{5.24}$$

where R_e and R are the projected half-light radius and its projected distance, respectively. Afterwards, they constructed the probability distribution for the unprojected distance r, given the projected distance R:

$$P(r|R) = \int_z P(r|z,R)P(z|R)dz, \tag{5.25}$$

where $P(r|z,R)$ is the Dirac delta function[8]. In this way, they calculated the cumulative distribution function (CDF) of r given R:

$$CDF(r|R) = \int_r^0 P(r'|R)dr' = \frac{(r^2-R^2)^{1/2}(r^2+\frac{1}{2}(3R_e^2+R^2))}{(r^2+R_e^2)^{3/2}}, \tag{5.26}$$

for $r > R$ and $CDF(r|R) = 0$ for $r < R$. In order to find the CDF of the distance to the outermost of n observed stars, they multiplied the CDFs for each of the n stars, i.e.:

$$CDF_{max}(r|R_1,...R_n) = \prod_{i=1}^{n} CDF(r|R_i), \tag{5.27}$$

where R_i is the measured projected distance to the i^{th} member star. It should be mentioned that this conservative method may provide lower values of J-profiles. One of the disadvantages of this method to extract the truncation radius is that it can be applied to mainly the ultra-faint dwarfs, which could not be promising targets as classical dwarfs. With this conservative way of choosing truncation halos, the outermost observed stars of the ultra-faints appear to be much closer than those in the classical dwarfs. For our analysis, we adopted the J-profile values and the NFW and r_{max} values calculated in this way by [171].

Another method to estimate the truncation radius would be to determine the radius where

[8] I.e., $P(r|z,R) = \delta(r - \sqrt{z^2+R^2})$

the halo density is equal to the density of the MW halo [173].

A third method would assume that the tidal radius[9] is a good estimator for the halo size [174, 175, 176]. It was found that that these last two methods are pretty consistent between each other [173]. However, assuming the tidal radius as a good indicator of the size of the dSph may lead (in some models) to lower values of the halo density of the outermost star than the one expected for the MW halo at the same position. This would be not possible as the outermost star would be lost due to tides. So, for example one way to prevent this problem would be to impose, for physical reasons, the tidal radius to be higher than the distance to the outermost star (as assumed in [171] too).

5.4.2 Systematic uncertainties on J-profile

J-factor measurement are affected by both statistical and systematic errors, having of course, different causes.

The former ones are due to finite size of the stellar-kinematic data samples, especially for the ultra-faint dSphs. For small stellar-kinematic samples ($N < 100$) typical for ultra-faint dSphs, the statistical errors dominate on systematic errors. They can be treated as nuisance parameters in a likelihood analysis.

Systematic uncertainties, on the other hand, dominate errors especially for large stellar kinematic samples ($N > 1000$) typical of classical dSphs. There are different causes from which systematic uncertainties may arise.

Firslty, the main contribution to the systematics comes from the many realizations of halo.

[9] The tidal radius is the theoretical limit for a particle bound to a satellite that is orbiting in the gravitational field of a host halo.

In fact, the analysis generates many realizations of halos which reasonably fit the same stellar kinematic data. The shaded band in Fig 5.6, for example, clearly shows our imperfect knowledge of the dwarf density profiles. In Chap. 7, the systematic uncertainties in our analysis, caused by many realization of the DM halo, will be shown.

Secondly, instrumental systematics should be considered too. High resolution spectrographs cannot resolve systematics at or below ~ 2 km/s of velocity dispersion (as we saw in Sec. 5.2).

Another cause for systematic uncertainties comes from the MW tidal field. In fact, dSphs that orbit within the MW can be stripped by the Galactic tidal force. For this reason, they would appear more elongated towards the center of the MW (observed from the Earth) and some "intruders" stars may be wrongly considered as dSph member stars (e.g., stars from MW). Thus the line-of-sight stellar velocity dispersion would be increased too, leading to differences in the J-factors of about 20%. Methods to clean dSphs from external stars have also been studied by [177].

Another source for systematics errors comes from several stellar population in dSphs. Each of them has a specific Jeans equation. If just one single stellar population is considered, the accuracy of derived J-factors will decrease by a factor of 2 [178].

For some dSphs, it is also uncertain to localize precisely the center of a classical dSph. This would lead to underestimate the cuspiness of both stellar and DM density profiles leading, in turn, to uncertainties on the J-factors of about 50%.

Another systematics arises from the non-sphericity of dSphs [179]. DM halos (as well as stellar component within dSphs) are commonly modeled as spherical [180, 181] but the typical projected minor-to-major axis ratio is ~ 0.3 [182]. Recently, N-body cosmological

simulations, on the other hand, pointed out that most likely a triaxial[10] analysis instead of a spherical one may be more appropriate [183, 184]. Triaxiality, however, causes also projection effects on the estimation of DM and stellar profile, which leads to a $\sim 30\%$ systematic difference on J-profile measurements, depending on the DM halo orientation with respect to the observer line of sight. In fact, projection effects have strong impact on the velocity dispersion measurement: it increases when the line-of-sight alignment moves from the short to the long axis (see Fig. 5.7).

[10] For a spherical model, axes a=b=c, while for a triaxial model $a > b > c$.

Figure 5.7: This plot from [140] shows the projection effects, along both short and long axis, on the reconstructed velocity dispersion profiles, using the cuspy model for DM ($\gamma = 1$ in Eq. 5.3.1). Legenda explains the meaning of the points showed in it.

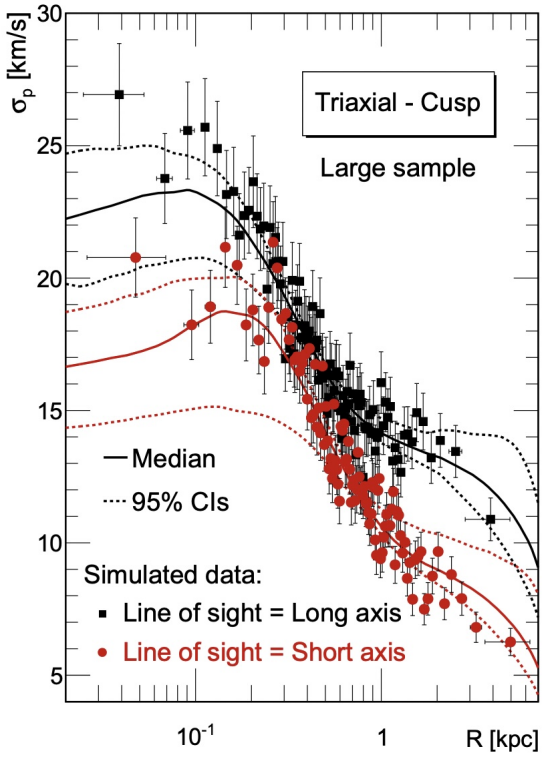

Chapter 6

Data analysis procedure

6.1 The goal

In previous published works such as [185] or [186], authors did set upper limits on the annihilation cross-section performing a conventional spectral analysis and considering dSphs as point-like sources. They used one of two VERITAS software packages, i.e. VEGAS [187]. They used cuts and IRFs for point-like sources, with a ON source region of radius $\theta^2 = 0.03\,\mathrm{deg}^2$ ($\theta = 0.17$), which are optimized for VEGAS.

In [171] (as we already saw in Sec. 5.4), they showed that some dSphs have an angular extension that goes beyond the selected ON region. Thus, IACTs have enough angular resolution to detect them as extended, so that we could exploit their angular information. For this reason, dSphs could be considered, and thus analysed, as extended sources.

The last two columns in Tab. 6.2 show the J-factor values and the angular extension of the dSphs. To include the angular extension information in our analysis, we did perform an unbinned maximum likelihood estimation (MLE), taking into account both energy and angular extension dependencies in observed events and DM spectra. We labeled this analysis

as "2D". On the other hand, the conventional analysis, taking into account only the energy of the observed evens was labeled as "1D".

The main goal of this thesis was to find/constrain DM properties by analysing dSphs with VERITAS dataset including their angular extension information in the likelihood analysis. In this work, we used another reconstruction analysis software package, i.e. EventDisplay [126].

Four dSphs were analysed (Bootes, Draco, Segue1, and Ursa Minor), which are published in the aforementioned works in order to compare our results to the ones obtained with the the conventional spectral and point-like analysis.

6.2 Statistical analysis technique - theoretical

6.2.1 Maximum Likelihood Estimation

One of the best statistical methods to compute best-fit parameters of a model is MLE, and the process of finding the best set of parameters is called "parameter estimation". The basic concept of MLE is that the best fit-parameters are the ones that maximise the probability of the observed data with respect to the given model [188]. Let's discuss in more detail what this method establishes.

The likelihood, which is defined as the total probability of observing the data, S, given the model, M, with a set of parameters, θ, can be described in the following way:

$$\mathcal{L}(\theta) = \prod_{i=1}^{N} \mathcal{L}_i(\theta) = \prod_{i=1}^{N} P(S_i|\theta, M), \tag{6.1}$$

where N is the number of samples. Commonly, it is used in the logarithm of Eq. 6.1, i.e. $-2\log\mathcal{L}$. With this definition, one has to find the values of parameters that minimize the likelihood function. There are several tools/packages for this process. One of the most used is a tool provided by ROOT [189], called *TMinuit* (used in this thesis too). TMinuit (the "minimizer") finds the minimum value of a function with different parameters and computes the best-fit parameter values with their uncertainties, taking into consideration the existing correlations between the parameters. However, one of the problems that the minimizer could face is the fact that it may find not the "global" minimum of the likelihood function, but the "local" one. This failure could be avoided by choosing different minimization methods, provided by ROOT. Also, it is possible to run the minimizer different times, every time with different initial set of parameters.

After finding the set of parameters at which the likelihood function is at its minimum, it is also possible to calculate the confidence interval of the parameters. The confidence interval is the range of values within which the true population value of the parameter will lie, with a certain confidence level (C.L.). In other words, the confidence level (usually expressed as a percentage) represents the probability that the parameter being estimated by the statistics would fall within the confidence interval. The C.L. can be also defined as C.L.$= 1 - p$, where the p-value is defined as the probability, taking under consideration the hypothesis H_0 (usually referred to as null hypothesis, as we will see in the next subsection), to obtain a result as consistent or less with H_0. The smaller the p-value, the higher the evidence in favor of an alternative hypothesis H_1 (with $H_1 \neq H_0$) [190]. If we have a Gaussian distribution, the 1σ interval corresponds to a 68.3% confidence level, the 2σ interval corresponds to a 95% confidence level and the 3σ interval corresponds to a 99% confidence level [1].

[1] Where σ is the standard deviation of the Gaussian distribution.

Table 6.1: Most commonly used C.L. and their associated p-value [192].

C.L.	p-value
90%	0.1
95%	0.05
99%	0.01

Fig. 6.1 shows the one-tailed distribution at 95% C.L. of the probability of observation under the H_0 hypothesis. Tab. 6.3 summarizes the most commonly used C.L.s with their associated p-value.

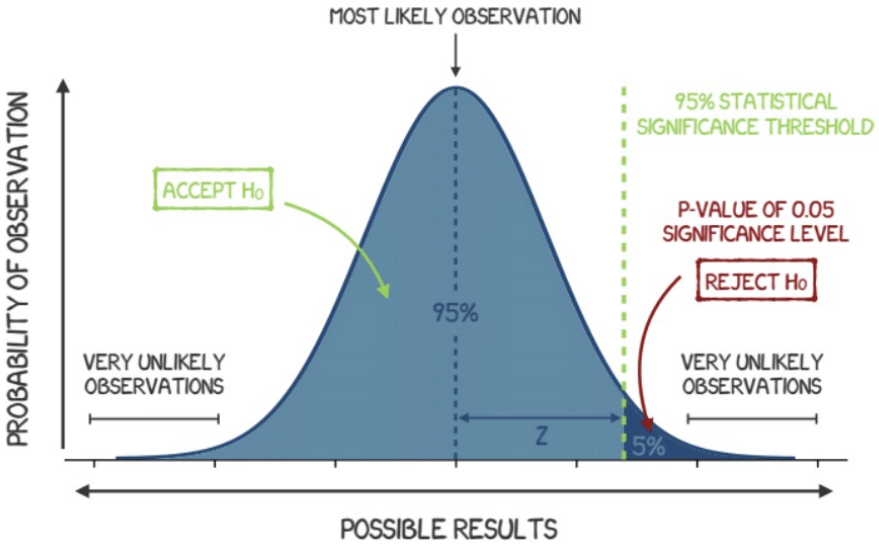

Figure 6.1: One-tailed distribution of the probability of observation under the H_0 hypothesis where the p-value is 0.05 corresponding to 95% C.L. [191].

Likelihood ratio test

As there are different theoretical models that could explain data, it is important to compare those models in order to rule out the one less likely. One essential tool to determine the validity of two competing models (or hypotheses) is the so-called "likelihood ratio test" [193, 190]. Usually, one compares H_0 (the null hypothesis) with H_1 (the alternative hypothesis). With the null hypothesis, generally, one assumes that no signal has been detected, whereas the alternative hypothesis has signal with background. Null hypothesis and alternative hypothesis have, respectively, n and m free parameters, being $n < m$. Thus, the likelihood ratio between these two models is defined as:

$$Ratio = \frac{\mathcal{L}_0}{\mathcal{L}_1}, \tag{6.2}$$

where $\mathcal{L}_0$ and $\mathcal{L}_0$ are the likelihood values of H_0 and H_1, respectively. For sake of simplicity, one calculates the so called test statistic, TS, defined as:

$$TS = -2\log(Ratio) = -2\log\left(\frac{\mathcal{L}_0}{\mathcal{L}_1}\right) = 2(\log\mathcal{L}_1 - \mathcal{L}_0). \tag{6.3}$$

The higher is the TS, the more H_1 is favored over H_0. For large datasets, the TS follows a χ^2 distribution, and in this case the significance of H_1 over H_0 is given by $\sqrt{TS}$ [190].

6.2.2 Conventional spectral analysis with likelihood ("1D analysis")

In order to detect a possible signal from DM annihilation and/or constrain its cross-section, an unbinned maximum likelihood estimation can be performed. We adopted the likelihood

function already proposed by [194, 195]. It includes the expected spectral shape from DM annihilation events, achieving in this way an improved sensitivity by a factor 1.5-2.5 (as already shown in [194, 195]), compared to the standard "Poissonian likelihood approach" proposed by [196]. Indeed, [195] used a more DM-oriented approach. They assumed *a priori* the expected spectral shape (which is fixed and known for a given DM model), and included it in the maximum likelihood analysis, they exploited the spectral information of the events from DM annihilation and achieve better sensitivity with respect to the standard analysis of the IACT data. In this "DM oriented" function, in addition to two Poissonian terms, there are two probability density functions to take the likelihood of ON and OFF region events as signal and background into account [138]:

$$L = \frac{(g+\alpha b)^{N_{\rm on}} e^{-(g+\alpha b)}}{N_{\rm on}!} \frac{b^{N_{\rm off}} e^{-b}}{N_{\rm off}!} \prod_{i=1}^{N_{\rm on}} P_{\rm on}(E_i|M,\langle\sigma_v\rangle) \prod_{j=1}^{N_{\rm off}} P_{\rm off}(E_j), \tag{6.4}$$

where $N_{\rm on}$ ($N_{\rm off}$) is the number of observed counts in the ON (OFF) region(s), b is the number of expected background counts, and α is the background normalization (i.e., the ratio between number of ON/OFF regions). The term $P_{\rm on}$ is the likelihood of the i^{th} ON region event with energy E_i to be an event from a distribution composed by the signal from DM annihilation and the background within the region of interest (ROI). This likelihood can be represented by:

$$P_{{\rm on},i}(E_i|M,\langle\sigma_v\rangle) = \frac{\alpha b p_b(E_i) + g p_g(E_i)}{\alpha b + g}, \tag{6.5}$$

where p_b and p_g are the probability density functions of background events and expected dark matter signal, respectively, as a function of reconstructed energy. The term $P_{\rm off}$ is the

same as $P_{\rm on}$, but for the OFF region (i.e., $g = 0$). The parameter g is the total number of expected events from the DM annihilation, at a given mass M and averaged annihilation cross-section $\langle\sigma_v\rangle$, within the ROI, and its differential form is:

$$\frac{dg}{dE} = \frac{\langle\sigma_v\rangle T_{obs}}{8\pi M^2} \int_{E'} \frac{dN}{dE'} J(E') A(E') D(E|E') dE', \tag{6.6}$$

where $A(E')$ is the effective area as a function of true energy E', T_{obs} is the observation time for a source, dN/dE' is the expected spectrum[2] of γ rays from a DM annihilation event (from [141]), $D(E|E')$ represents the probability of an event with true energy E' having a reconstructed energy E (i.e. the energy dispersion matrix), and $J(E')$ is the integrated J factor as a function of true energy E', that has to be convolved with the PSF of the instrument. It is evident that all variables are expressed as a function of energy. In order to consider the logarithm of function 6.7, we would have:

$$\begin{aligned}
\log \mathcal{L} =& N_{on} \log(g + \alpha b) - (g + \alpha b) - \log(N_{on}!) + N_{off} \log(b) - b \\
& - \log(N_{off}!) + \sum \log \left(\frac{\alpha b \mathcal{P}_{off}(E_i) + g \mathcal{P}_s(E_i)}{\alpha b + g} \right) + \sum \log \mathcal{P}_{off}(E_i) \\
=& N_{on} \log(g + \alpha b) - (g + \alpha b) + N_{off} \log(b) - b \\
& - N_{on} \log(g + \alpha b) + \sum \log \left(\alpha b \mathcal{P}_{off}(E_i) + g \mathcal{P}_s(E_i) \right) \\
=& N_{off} \log b - g - (1 + \alpha) b + \sum \log \left(\alpha b \mathcal{P}_{off}(E_i) + g \mathcal{P}_s(E_i) \right),
\end{aligned} \tag{6.7}$$

where $\mathcal{P}_s = \frac{1}{g} \frac{dg}{dE}$.

[2] Assuming here a 100% branching ratio into a certain annihilation final state.

Finally, we can get the logarithm of the likelihood function 6.7:

$$log\mathcal{L} = N_{off} \log b - g - (1+\alpha)b + \sum \log\left(\alpha b \mathcal{P}_{off}(E_i) + g\mathcal{P}_s(E_i)\right). \tag{6.8}$$

The log-likelihood for the null hypothesis will be:

$$log\mathcal{L}_{null} = N_{off} \log b_{null} - (1+\alpha)b_{null} + \sum \log\left(\alpha b_{null} \mathcal{P}_{off}(E_i)\right), \tag{6.9}$$

where

$$b_{null} = \frac{N_{on} + N_{off}}{\alpha + 1}. \tag{6.10}$$

We will describe in more detail in the next sections specifically what specific input files we used and how we generated them in order to estimate the 1D likelihood function.

6.2.3 Adding spatial information into the likelihood ("2D analysis")

To achieve the main goal of this work, i.e. exploiting the angular extension properties of dSphs, we modified the Eq. 6.7 likelihood function in order to include the spatial information in it. Firstly, we computed a two-dimensional (2D) J factor as a function of true energy and solid angle, $J(E', \Omega)$. Also, we built the 2D probability density functions for signal and background; i.e., $p_g(E', \theta)$ and $p_b(E', \theta)$. Therefore, the "extended" (or "2D") likelihood function is represented by:

$$L = \frac{(g+\alpha b)^{N_{\rm on}} e^{-(g+\alpha b)}}{N_{\rm on}!} \frac{b^{N_{\rm off}} e^{-b}}{N_{\rm off}!} \prod_{i=1}^{N_{\rm on}} P_{\rm on}(E_i, \theta_i | M, \langle\sigma_v\rangle) \prod_{j=1}^{N_{\rm off}} P_{\rm off}(E_j, \theta_j). \tag{6.11}$$

The number of expected events from DM annihilation is then given by:

$$\frac{d^2g}{dEd\Omega} = \frac{\langle\sigma_v\rangle T_{obs}}{8\pi M^2} \int_{E'} \frac{dN}{dE'} \frac{J(E',\Omega)}{d\Omega} A(E')D(E|E')dE', \tag{6.12}$$

whose total number is simply given by integrating Eq. 6.12 over the solid angle and the true energy:

$$g = 2\pi \int_E \int_\theta \frac{d^2g}{dEd\Omega} \sin(\theta) dEd\theta. \tag{6.13}$$

The logarithm of function 6.11 is:

$$log\mathcal{L} = N_{off} \log b - g - (1+\alpha)b + \sum \log\left(\alpha b \mathcal{P}_{off}(E_i,\theta_i) + g\mathcal{P}_s(E_i,\theta_i)\right). \tag{6.14}$$

The log-likelihood for the null hypothesis will be:

$$log\mathcal{L}_{null} = N_{off} \log b_{null} - (1+\alpha)b_{null} + \sum \log\left(\alpha b_{null} \mathcal{P}_{off}(E_i,\theta_i)\right), \tag{6.15}$$

where

$$b_{null} = \frac{N_{on} + N_{off}}{\alpha + 1}. \tag{6.16}$$

For several masses, we minimised the negative logarithm of Eq. 6.7 with respect to two free parameters (σ and the nuisance parameter b) to constrain the DM annihilation cross-section. The significance of the DM signal was estimated from the likelihood ratio test, TS$= -2(log(L_0/L_1))$, where L_0 is null hypothesis (no signal) and L_1 is the alternative model hypothesis (including signal). For a one-sided likelihood, the value TS $= 2.71/2$ has

to be solved[3], allowing us to set 95% C.L. limits.

6.3 VERITAS analysis

In this section, we are going to give more details about the specific criteria applied to select our dataset, such as time cuts, weather condition and epoch, in order to select only good quality data. Afterwards, we will also see what background estimation method was adopted and its consequences. In conclusion, we will talk about how we optimized the θ^2 cut applied to perform the 2D analysis.

6.3.1 Constructing the dataset

In this work, we analysed VERITAS data from four dSphs, i.e Bootes, Draco, Segue1 and Ursa Minor. We did choose specifically these four dSphs because the same ones were used in the previous VERITAS published point-like work [185], in order to make a direct comparison. Tab. 6.2 summarizes the main properties of the dSphs analysed in this work, such as their astronomical coordinates (RA and Dec.), their magnitude, their distance D from the Earth to the center of the dSph, the truncation radius at the outermost observed star r_{max} and the corresponding θ_{max}, the J factor value integrated within a cone of radius θ_{max} (from [171]). Fig. 6.2 shows also the events zenith and azimuth distribution, for all dSphs.

[3] Only positive values of the TS are allowed.

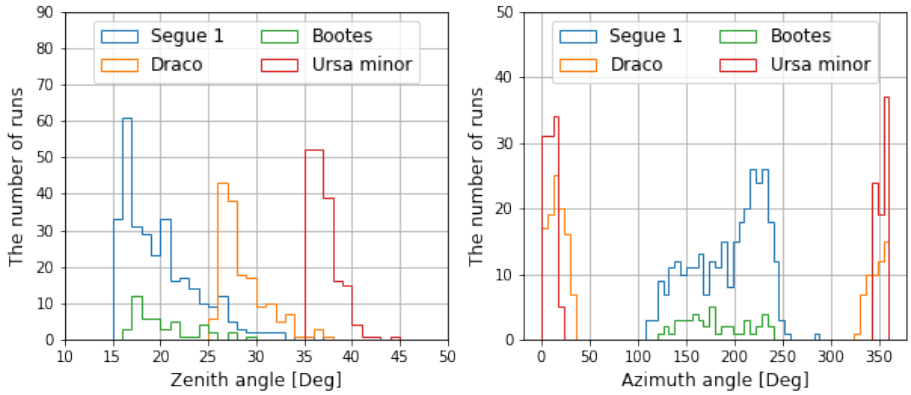

Figure 6.2: Zenith and Azimuth distributions of the four dSphs analysed here.

The observation period considered was between 2007 up to 2013, for a total amount of quality-selected time of 475.65 hrs[4]. Note that only data with good weather conditions were taken, as well as in dark conditions (no moonlight) and with no hardware malfunctions. This was done in order to minimise the effect of systematic errors on the final results. In our case, only data with weather labelled as "A" (completely clear sky) and/or "B" (few thin cloud) were selected. The first four columns in Tab. 6.4 show the exposure time, respectively, per array epoch (i.e. "V4", "V5" and "V6") and the total exposure time per each dSph.

Furthermore, another criterion applied to select runs was that data had to be taken in wobble mode [133], already described in Chap. 4). We also required that all four telescopes were operating during the observations. No filter (such as RHV data) was applied to data. Finally, to estimate the background counts, we decided to use the so called "Reflected

[4]This is the total amount of time before applying any time cuts.

Table 6.2: Main properties of the dSphs, i.e. RA, Dec., the distance D from Earth to the center of the dSph, their magnitude, the truncation radius at the outermost observed star r_{max} and the corresponding θ_{max}, the J factor value integrated within a cone of radius θ_{max} (taken from [171]).

Source	RA [hh:mm:ss]	Dec. [dd:mm:ss]	D [kpc]	M_V [mag]	r_{max} [pc]	θ_{max} [deg]	$\log_{10} J(\theta_{max})$ $\log_{10}$[GeV^{2}cm^{-5}]
Boötes I	14:00:06.07	+14:30:00	66 ± 2	-6.3 ± 0.2	544^{+252}_{-135}	0.47	$18.24^{+0.40}_{-0.37}$
Draco	17:20:12.4	+57:54:55	76 ± 6	-8.8 ± 0.3	1866^{+715}_{-317}	1.30	$19.05^{+0.22}_{-0.21}$
Segue I	10:07:04.0	+16:04:55	23 ± 2	-1.5 ± 0.8	139^{+56}_{-28}	0.35	$19.36^{+0.32}_{-0.35}$
Ursa Minor	15:09:08.5	+67:13:21	73 ± 3	-8.8 ± 0.5	1580^{+626}_{-312}	1.37	$18.95^{+0.26}_{-0.18}$

regions model background"[133] (and see also Sec. 4.2.5).

6.3.2 Time cuts

Time cuts were also applied to single runs, after a careful analysis of single L3 plot of each run (see Chap. 4 about L3). This was done to remove any spike or dip in the L3 rate, meaning that some signal loss due to either bad weather condition or hardware malfunctions. In more detail, per each run, we selected a specific time interval (or even multiple time windows) to be excluded, in order to mask it. An example of this type of cut was already shown in Chap 4, Sec 4.1.4.

After applying these time cuts to our dataset, and also the deatime correction (see Chap. 4 for deadtime definition), the total amount of exposure time, per each dSph, is shown in Tab. 6.3.

Table 6.3: Table showing, per each dSph, the time before (exposure time) and after (live time) correcting for deadtime and applying time cuts (these selected as explained in the text) and their ratio.

dSph	Exp. Time [hrs]	Live Time [hrs]	ratio in %
Segue1	103.53	92.83	0.01
Ursa Minor	67.46	57.1	0.01
Draco	55.13	42.54	0.01
Bootes	15.33	13.97	0.01

6.4 VERITAS reconstruction analysis/data processing

We analysed the dSphs data with one of the two official reconstruction analysis softwares, i.e. *EventDisplay* [126], version v483. Standard calibration and reconstruction pipeline were used (for an overview of the standard reconstruction analysis pipeline, see Chap. 4). In order to further reduce the hadronic cosmic-ray background, we decided to apply BDT cuts [132].

The "Reflected Region Model" [133] was used to define regions to estimate/extract the background contribution, i.e. the OFF regions. We defined them on a run-by-run basis. For all our dSphs we used six OFF regions so that the normalization ratio between the ON- and OFF-regions, the relative exposure time, is $1/6$, $\alpha = 0.167$. The size of each ON- and OFF regions is the same, θ^2 of 0.008 deg^2 for a point-like source[5]. Since we are interested in the extension of the dSphs, we extended the size to the optimal value, $\theta^2 = 0.02$ deg^2 (see Sec. 6.5.1). In addition, we had to mask the signal region in order to prevent the signal leakage into the background regions. To do this, the ON- and OFF-regions were set apart from at least $\theta^2 = 0.35$ deg^2 around each dwarf, except for Draco, for which we used

[5]This is valid for *EventDisplay*, as we saw that for VEGAS for a point-like source it is used 0.03 deg^2.

a radius of $\theta^2 = 0.5\ deg^2$, considering its high extension. This selection was based on the simulation study (see Fig. 6.3). This figure shows the cumulative rate only of the signal to see how extended the signal distribution is for all dSphs. In principle, we set as radius of the exclusion region around the dSph the θ^2 value at which the cumulative rate reached approximately the value of 1.

Visible starlight can also affect the background estimate, so we removed bright stars by excluding circular background exclusion areas centered on stars with minimum apparent magnitudes of $m_B < 7$ with a size of $0.25°$.

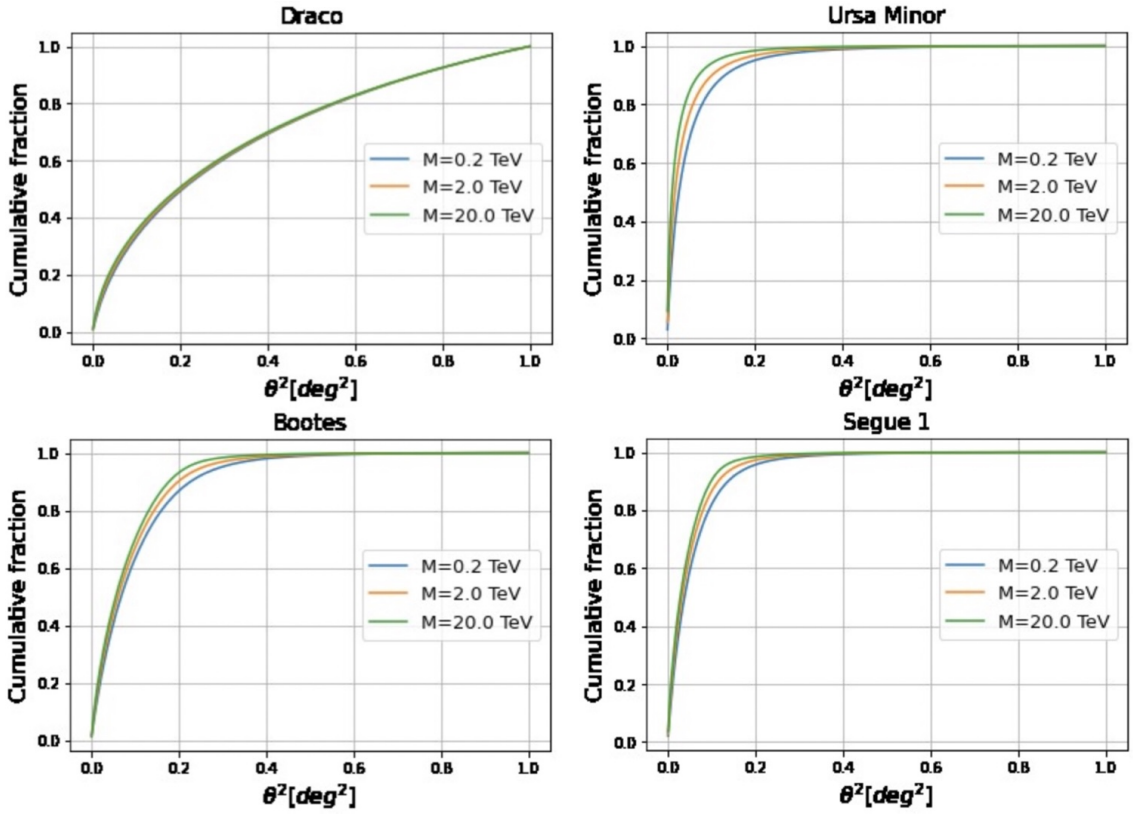

Figure 6.3: Plots showing the relative rate of expected DM signal as a function of the angular extension of the dSphs, for three different masses, as shown in the legend, for all dSphs. Based on these images, the exclusion radius around the source was chosen, as explained in the text. Courtesy of Dr. Donggeun Tak.

6.5 θ^2 cut optimization

6.5.1 Theoretical optimum - expected signal

As the goal of this thesis is to analyse dSphs as extended sources, IRFs suitable for performing an extended analysis were needed to be first generated and then used. Since the IRFs depend on the size of the region (θ^2)[6], we performed an optimization study in order to find the optimal θ^2 cut based on the DM property. Note that this was mostly performed by my colleague, Dr. Donggeun Tak. We did expect that each dSph would have its own angular extension with a different optimal θ^2 value. Firstly, we checked how the Li&Ma significance [197] varied by extending the size of the source region (Fig. 6.4 and Fig. 6.5). For each dwarf and mass, we tried to find θ_p^2 where the Li&Ma significance peaked. We generated the DM signal count for the $\tau^+\tau^-$ annihilation channel (Eq. 6.13) and calculated the Li&Ma significance, assuming that $N_{\rm on} = \alpha N_{\rm off} + g$ (Fig. 6.5). Above the θ^2 cut (>0.008 deg^2), we assumed that the background rate is constant. Note that in principle the background rate is independent of θ^2 within the central region of the camera. Fig. 6.5 shows θ_p^2 as a function of mass. Note that θ_p^2 is independent of the DM cross-section and exposure time. We can see that the value of θ_p^2 tends to decrease as mass increases. This simulation study implies that to detect all possible signals from the DM annihilation, we would need to increase the size of a source region to the optimal value, depending on the characteristics of the dwarf.

[6] E.g, the higher the θ^2 cut value, the higher the effective area.

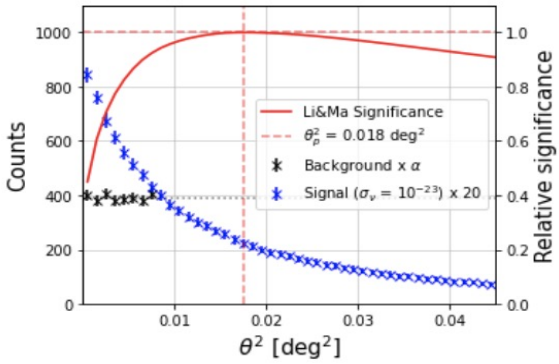

Figure 6.4: Dependence of the Li&Ma significance on the angular extension for Segue1 at 1 TeV. The dashed line is where the Li&Ma significance peaks (θ_p^2).

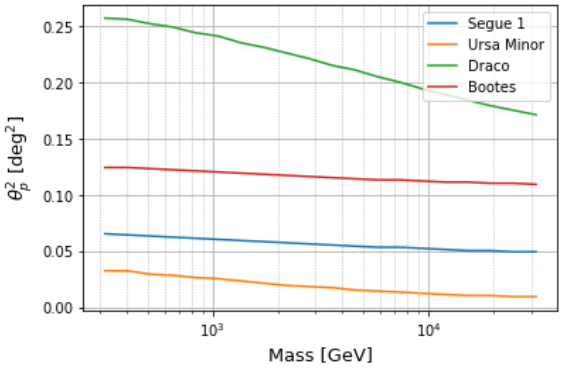

Figure 6.5: Dependence of θ_p^2 on DM mass for the four dSphs considered.

6.5.2 Realistic optimum - skymap study

In the previous section, we found that the preliminary optimal θ^2 cut value would depend on the characteristics of each dSph. However, it does not mean we can use the optimal value for each dSphs. It is because we also need to consider whether the skymaps look reasonable or not. To verify this, we generated IRFs for different θ^2 cuts and gamma-hadron separation cuts and check whether the skymap, which is the image of a portion of sky centered on the source in sky coordinates plane, is well behaved (see Sec. 4.2.5). We checked the Li&Ma significance at each location/point of the skymap and the significance distribution, which is extracted from the skymap for all the points in the skymap. If the background was correctly estimated (i.e, it was not underestimated or there was no leaking to OFF regions), one would expect the significance distribution of the source to be Gaussian

distributed around the value of 0 and RMS of about 1.

In order to generate skymaps, there is no need to use full IRFs, but it is sufficient to apply the gamma-hadron selection (see Sec. 4.2.4) to raw data, which contains information on several stereo quality cuts, among which the direction cut, which is exactly the θ^2 cut value we are interested in. Then, we could set the value of θ^2 cut that we wanted to test.

For the preliminary study, we started from Ursa minor because its density distribution is compact compared to others with a high J-factor value (see Fig. 6.5), and it has a deep exposure (as reported, respectively, in Tab. 6.2 and 6.4).

We started from $\theta^2 = 0.035$ cut deg^2, which (looking at Fig. 6.5) is the optimal θ^2 cut value at the DM mass where VERITAS has its best sensitivity [49], around 600 GeV, which is in agreement with the previous study [185]. We obtained the results shown in Fig. 6.6. As it can be seen, the significance distribution looked too wide/poorly behaved, meaning that the background estimation was not good enough and/or the cut was too loose.

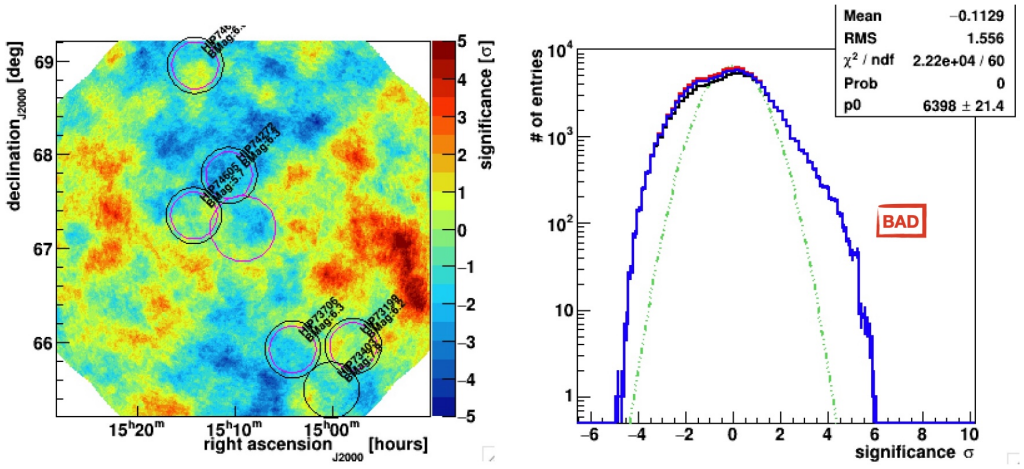

Figure 6.6: Skymap and significance distribution of Ursa Minor, using $\theta^2 = 0.035$ deg^2.

For this reason, we rejected $\theta^2 = 0.035$ cut deg^2, and tightened the cut up up to $\theta^2 = 0.030$ cut deg^2, whose result is shown in Fig. 6.7. Again, the significance distribution looked still too wide.

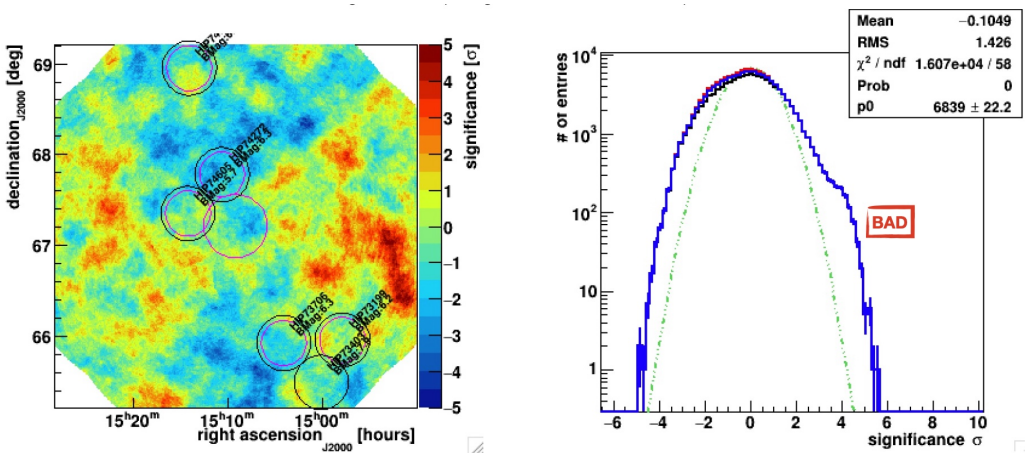

Figure 6.7: Skymap and significance distribution of Ursa Minor, using $\theta^2 = 0.030$ deg^2.

We further tightened the cut up up to $\theta^2 = 0.025$ cut deg^2 (see Fig. 6.8). However, the cut was still too loose.

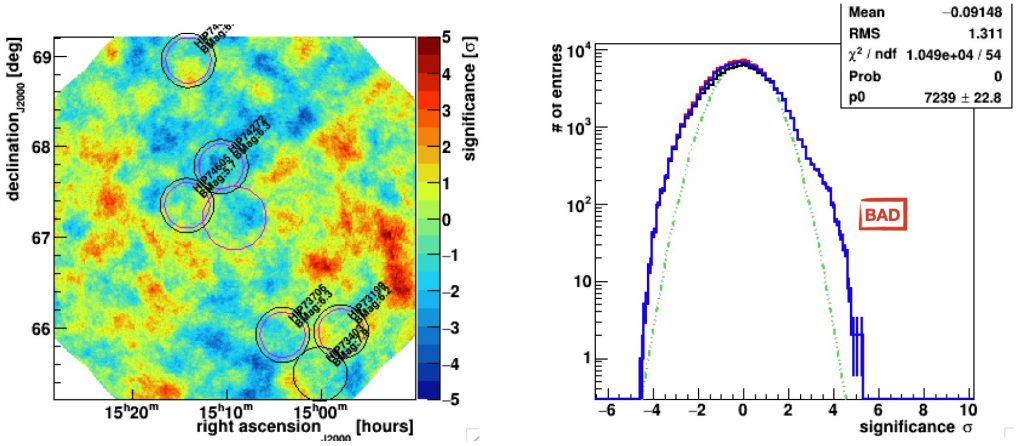

Figure 6.8: Skymap and significance distribution of Ursa Minor, using $\theta^2 = 0.025$ deg^2.

At the end, we decided to set the cut at $\theta^2 = 0.020$ cut deg^2, as the significance distribution was acceptable enough (see Fig. 6.9).

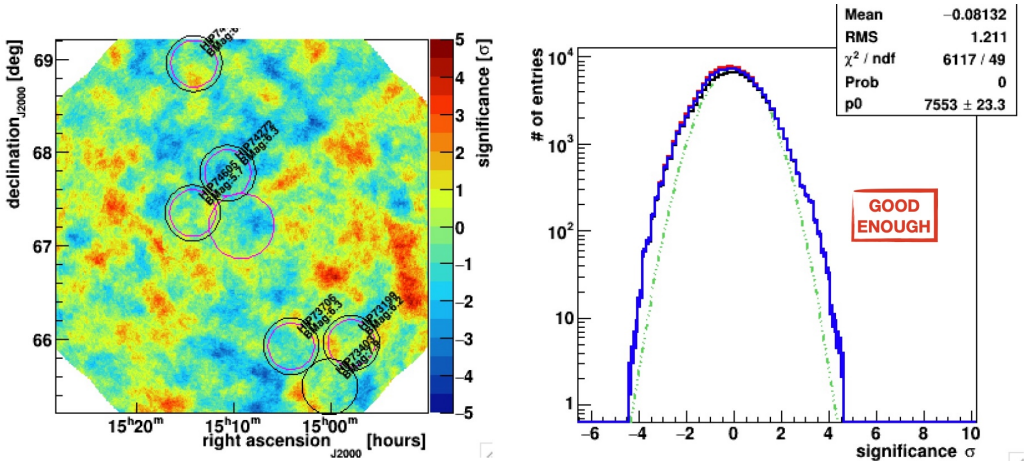

Figure 6.9: Skymap and significance distribution of Ursa Minor, using $\theta^2 = 0.020$ deg^2.

Another type of cut that affects the goodness of the results/skymaps is the one applied on the second largest image size, i.e. the one that specifies if soft, moderate or hard cuts are used. As dSphs are weak sources, one would expect to use soft cuts, in order to get as much signal as possible. As well as using the "NTel2" cut (meaning that two telescopes must record images from an event in order for the event to be selected) should increase the signal. However, we decided to use moderate and NTel3 cuts (same meaning of NTel2, but with three telescopes), because using soft and NTel2 cuts led to the results shown in Fig. 6.10, which looks poorly reconstructed. It has to be said, though, that in the previous published results [185], they used soft and NTel2 cuts, whose values were adapted specifically to VEGAS package.

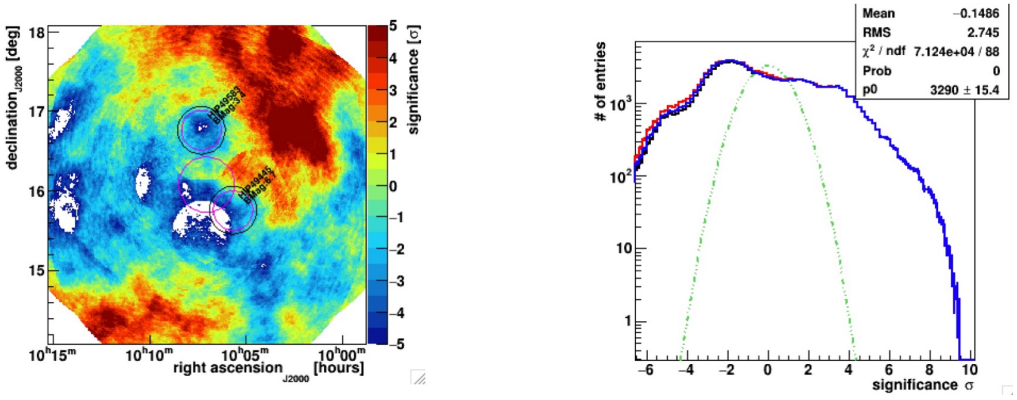

Figure 6.10: Skymap and significance distribution of Segue1, using $\theta^2 = 0.5$ deg^2, soft cuts.

Moreover, for all these tests we did use BDT cuts too, in order to improve the gamma-hadron discrimination.

Finally, after setting the $\theta^2 = 0.02$ deg^2 as optimal value for Ursa minor, the final skymaps and significance distributions are shown in Fig. 6.11. This cut is much tighter than the

Table 6.4: VERITAS data analysis results, i.e. exposure time for the three different epochs (V4, V5 and V6), total observation time, N_{on} and N_{off} counts and the detection significance (in units of standard deviation σ). Note that the background normalization factor is $\alpha = 0.167$ for all four dwarfs.

Source	Exp. V4 [min]	Exp. V5 [min]	Exp. V6 [min]	Tot. Exp. [min]	$N_{\rm on}$ [counts]	$N_{\rm off}$ [counts]	α	σ [σ]
Boötes I	960	0	0	960	398	2351	0.167	0.3
Draco	1169	2170	3435	6813	1326	8119	0.167	-0.7
Segue I	0	6121	4921	11042	3227	19947	0.167	-1.5
Ursa Minor	711	2209	6844	9724	1328	8204	0.167	-1.5

optimal value obtained from the DM property (Sec 6.5.1). We expect that this cut cannot be extended (or marginally extended) in other dSphs because this limit is set by the instrument properties. Therefore, we concluded that θ^2 of 0.02 deg^2 is the most extended size for this study, and we chose this value for the other dSphs as well.

Table 6.4 shows the VERITAS data analysis results of this work. For each dSph, it shows the quality-selected observation time per each epoch, the total exposure time, the $N_{\rm on}$ and $N_{\rm off}$ counts, i.e. the number of observed counts in, respectively, the ON and OFF regions and the detection significance[7].

[7] Calculated using Li&Ma Eq. 17 in [197].

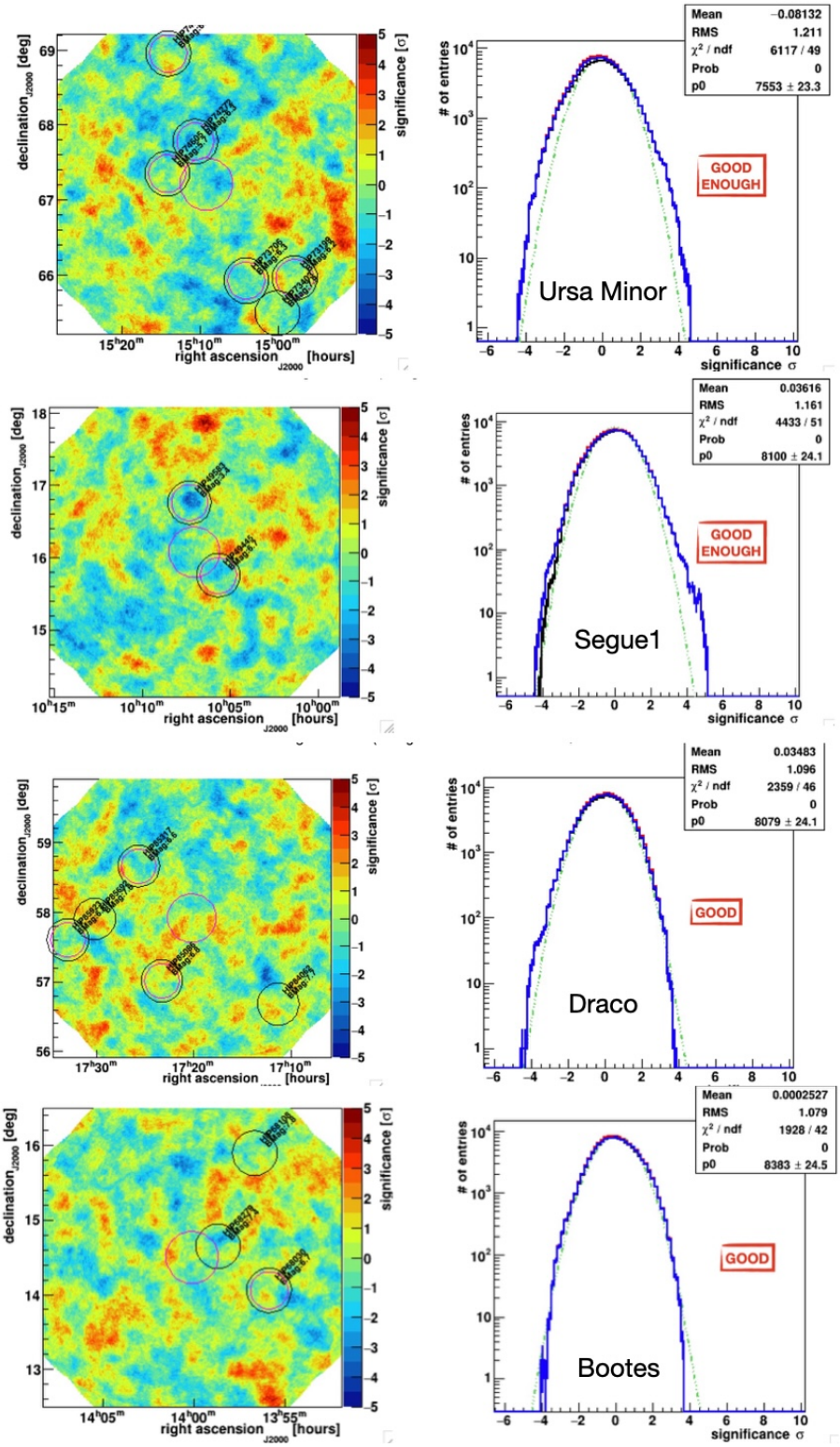

Figure 6.11: Skymap and significance distribution of all dSphs, using $\theta^2 = 0.20$ deg^2, soft cuts.

6.6 Likelihood analysis - practical

6.6.1 Dark matter spectra

First of all, we needed DM spectra for the likelihood analysis. The DM spectra of various annihilation channels are provided by [141] (PPPC4DM, Fig. 6.12), who used two MC simulations generators (PYTHIA and HERWIG [198, 199]) to compute them. They also included electroweak corrections (see Chap. 2). From this spectrum, we can get the dN/dE' (see Eq. 6.2.2 and Eq. 6.12) value for each DM mass and true energy, i.e. the energy spectrum of a single annihilation, assuming a 100% branching ratio into an annihilation final state. With PPPC4DM, we analysed two annihilation channels because DM is expected to annihilate more likely into heavier channels such as $b\bar{b}$ (the second heaviest quark) and $\tau\tau$ (the heaviest lepton). Moreover, they are widely studied in other literature, so it would be good for the comparison study.

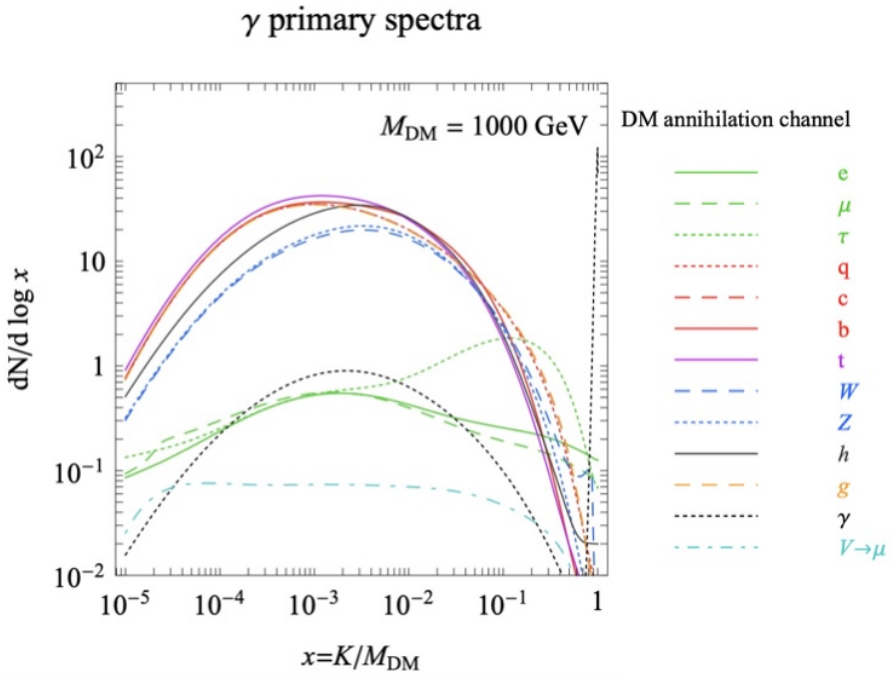

Figure 6.12: Primary flux from γ rays at $M_{DM} = 1000$ GeV, for different annihilation channels [141].

6.6.2 J-factor

Another factor that we needed for the likelihood analysis is the J-factor term. We calculated it, per each dSph, by using the NFW formula, whose parameters were taken from [171] (we already discussed about [171] work in Sec. 5.4).

As [171] provided multiple sets of NFW parameters, we decided to use one of the sets resembling the 50th percentile of the J-factor distribution by eye (Figure 6.13).

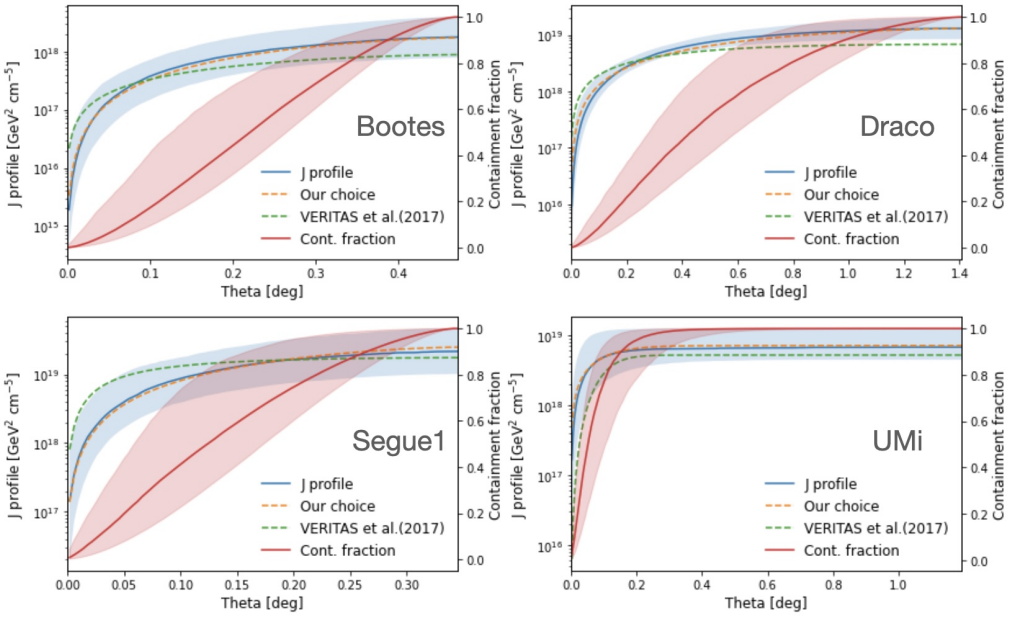

Figure 6.13: Blue line: J-profiles for all dSphs, as a function of the dSph angular extension. Red line: containment fraction of J-profile, defined accordingly to [171]. Orange line: the actual J-profile used for our analysis, using a real NFW set of parameters. Green line: J-profile used in the work published in [185].

Our study on the systematic uncertainty due to the J-factor can be found in Sec. 7.2. For the 1D analysis, we calculated the J-profile as function of the reconstructed energy, while for the 2D analysis we calculated the J-profile as a 2D function of energy and angular extension (θ^2). Moreover, we convolved the J-profile with the PSF of the telescope in order to take into account the finite resolution of the instrument. Each PSF was obtained by interpolating the simulated PSF, as each run depends on specific zenith or azimuth angles and NSB level. Then, for each dwarf, PSFs were "weighted"-averaged by the livetime of each run. An example of the weighted-averaged PSF with point-like cut is shown in Fig. 6.14.

Fig. 6.15 shows an example of the weighted-averaged PSF with extended cut.

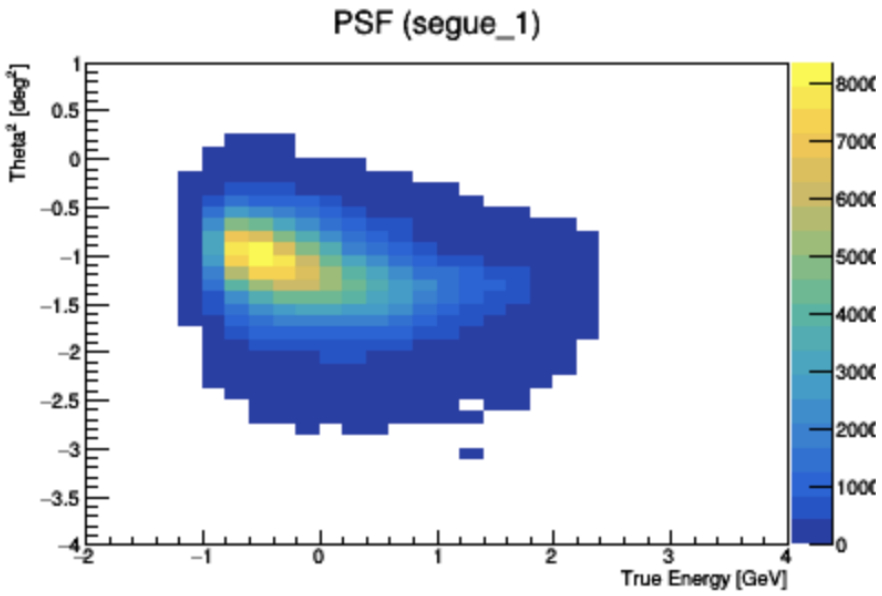

Figure 6.14: Weighted Segue1 PSF with point-like cut.

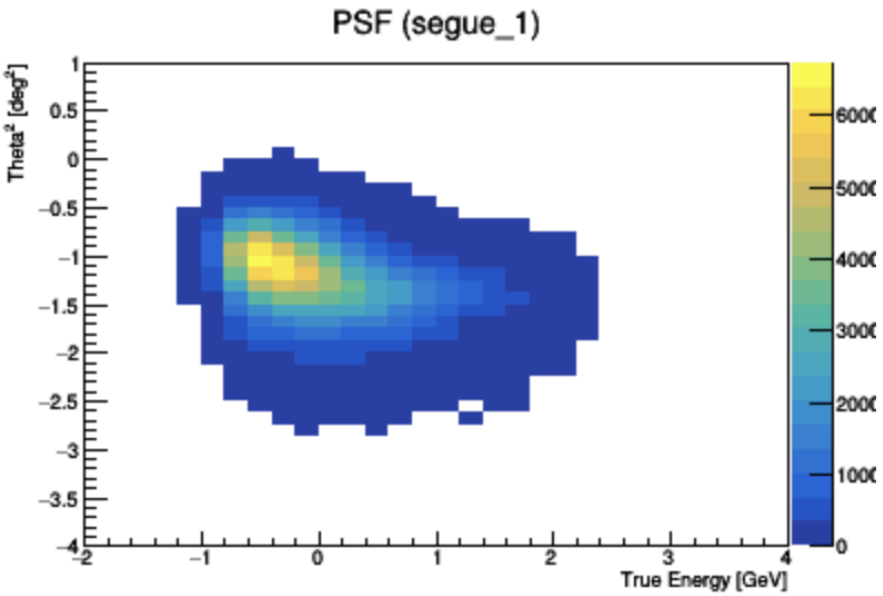

Figure 6.15: Weighted Segue1 PSF with extended cut.

Fig. 6.16, Fig. 6.17, Fig. 6.18 and Fig 6.19 show both the 1D and the 2D convolved J-profile for each dwarf, where we calculated and used for this analysis. For both 1D and 2D analyses, we used the same NFW set of parameters in order to calculate the J-profile.

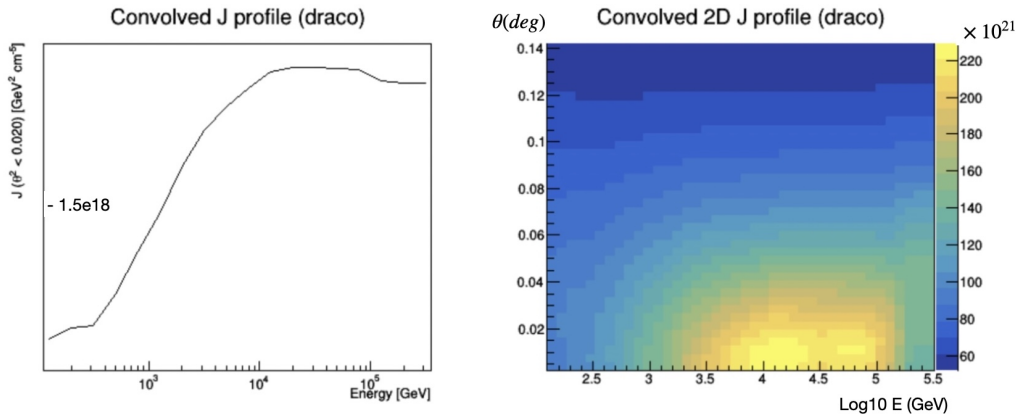

Figure 6.16: 1D (left) and 2D (right) convolved J-profile for Draco. In the 2D histogram: the x-axis is $\log_{10} E$ GeV, on the y-axis is the θ^2 expressed in deg^2, and on the z-axis the counts.

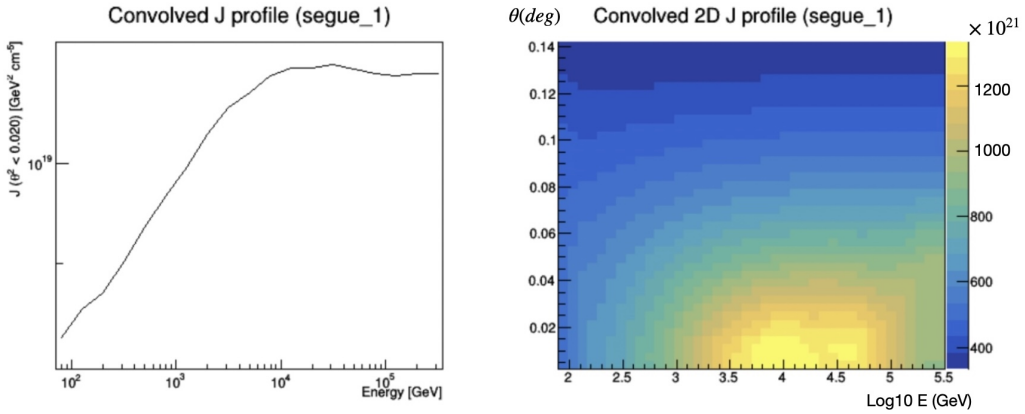

Figure 6.17: 1D (left) and 2D (right) convolved J-profile for Segue1. For axes description, see Fig. 6.16.

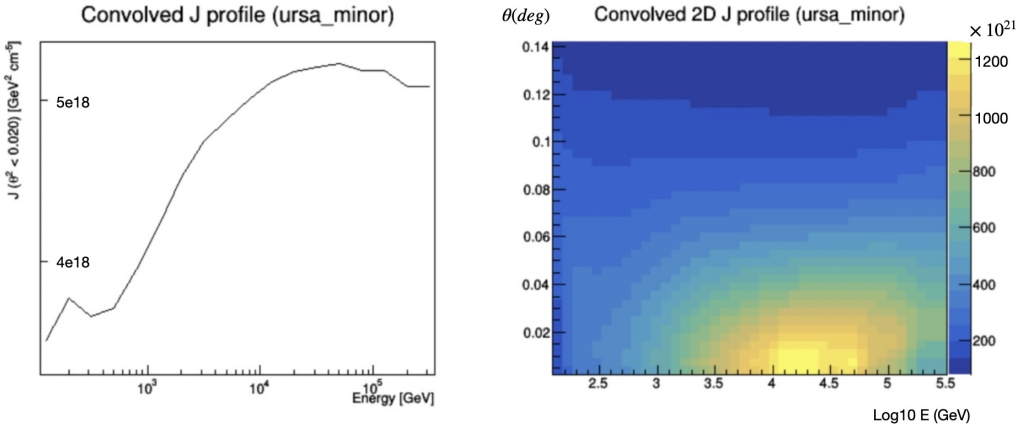

Figure 6.18: 1D (left) and 2D (right) convolved J-profile for Ursa Minor. For axes description, see Fig. 6.16.

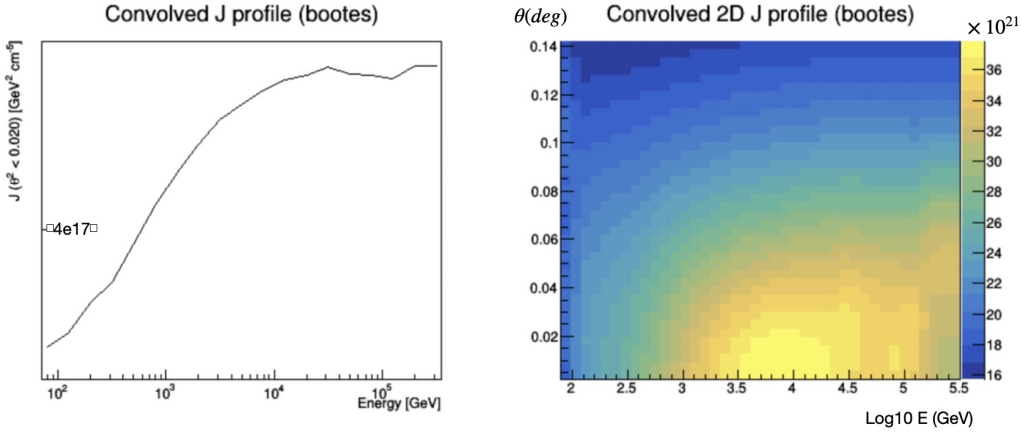

Figure 6.19: 1D (left) and 2D (right) convolved J-profile for Bootes. For axes description, see Fig. 6.16.

6.6.3 IRFs - energy disperson and effective area

Other IRFs in addition to the PSF were needed for this analysis: the energy dispersion matrix and the effective area. The energy dispersion matrix is the histogram containing the probability D(E,E') of having reconstructed energy E' if the true (MC) energy is E. For the energy dispersion matrix, we made the weighted-averaged one as well. Fig 6.20 and Fig. 6.21 show, respectively, the energy dispersion matrix as an example used with extended cuts and point-like cuts.

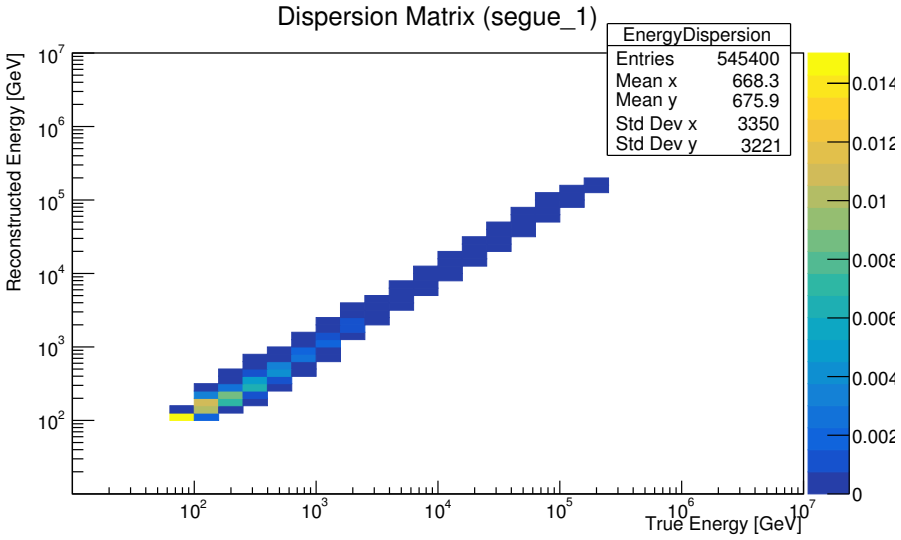

Figure 6.20: Extended ($\theta^2 = 0.02$ cut) energy dispersion matrix for Segue1.

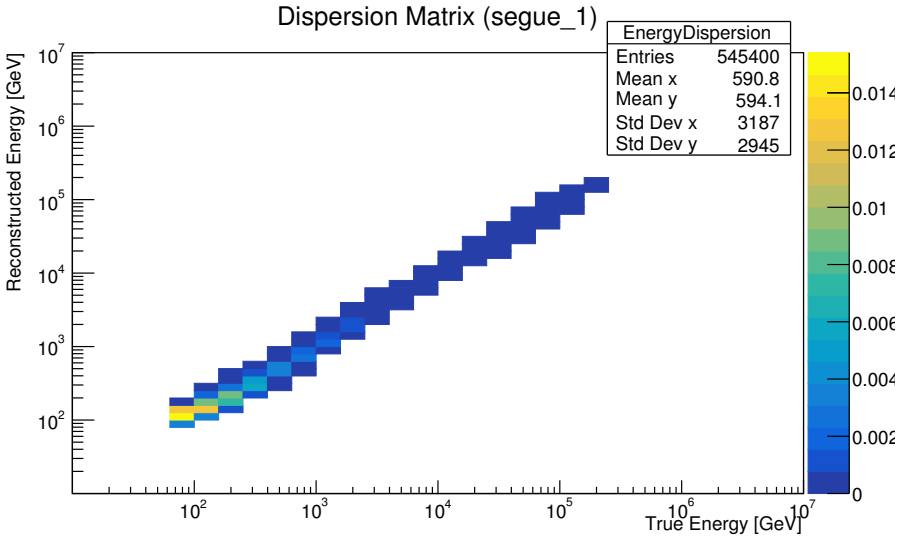

Figure 6.21: Point-like (θ^2 = 0.008 cut) energy dispersion matrix for Segue1.

The effective area is the true energy versus area (cm^2), which converts the photon counts to flux. Fig 6.22 and 6.23 show, respectively, the effective areas used with extended cuts and point-like cuts.

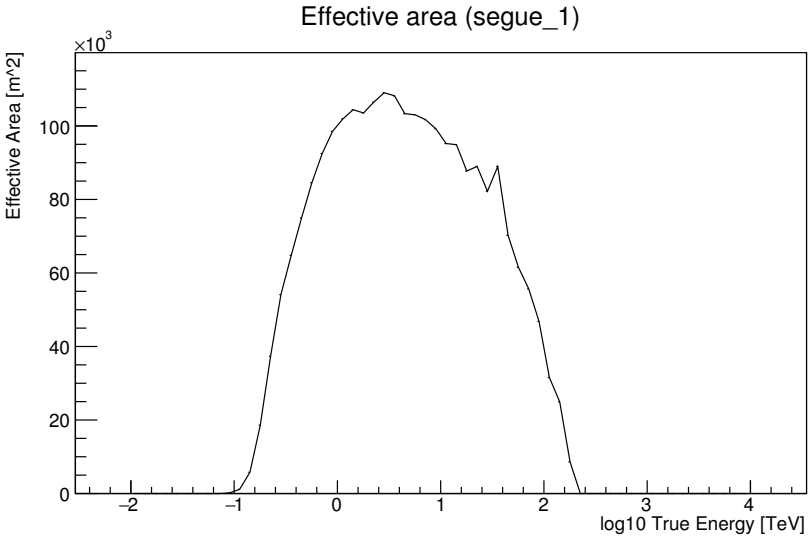

Figure 6.22: Extended ($\theta^2 = 0.02\ deg^2$ cut) effective area for Segue1.

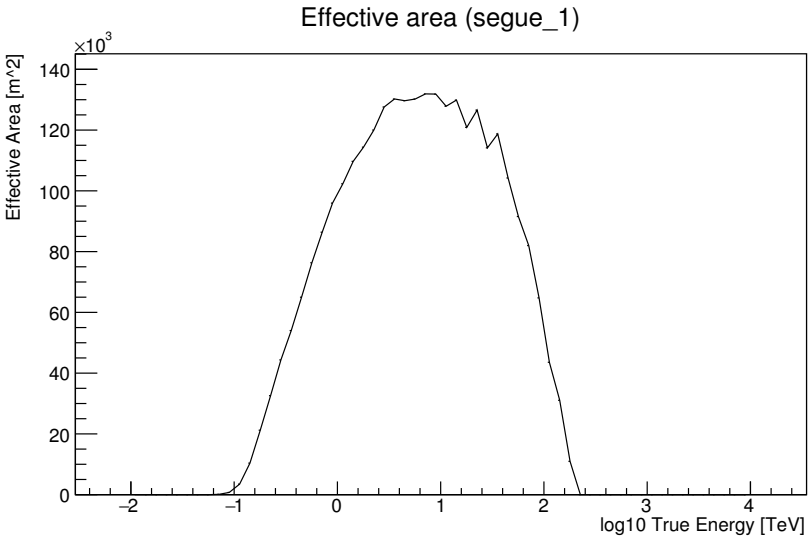

Figure 6.23: Point-like ($\theta^2 = 0.008\ deg^2$ cut) effective area for Segue1.

6.6.4 Observed events

For each run, we generated the eventlist table to perform the unbinned likelihood analysis. For each dSph, we created a ".txt" file containing in columns, per each run of the dSph, the following information in order: the run number, its energy, a boolean that classifies whether it is from ON- or OFF-regions, and its θ value. Instead of using all events, we applied two additional selection criteria based on the energy dispersion matrix and effective area of each run. We ignored events whose energy is lower than certain thresholds: the deviation between the true and reconstructed energies is higher than 20%, and the effective area is lower than 15% of its maximum. With these eventlists, we could generate 1D and 2D histograms of N_{off} and N_{on}. Fig. 6.24, Fig. 6.25, Fig. 6.26 and Fig. 6.27 show, for all dSphs, the ON- and OFF-regions distribution used for the 2D analysis with extended cuts. Due to the limited background observation, the probability density function of background events is not continuous and precise; in some very-high-energy bins, there are no background events, so that we cannot assign the background likelihood when events correspond to those bins. To overcome this problem, we could have fitted the low-energy background distributions with a power law, and then extrapolated up to the highest energy we observed in all regions (see Fig. 6.28).

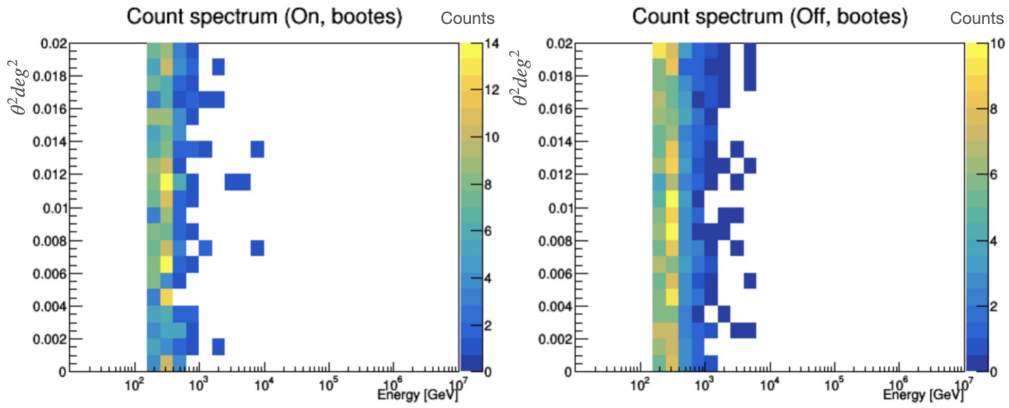

Figure 6.24: N_{on} and N_{off} 2D distribution for Bootes.

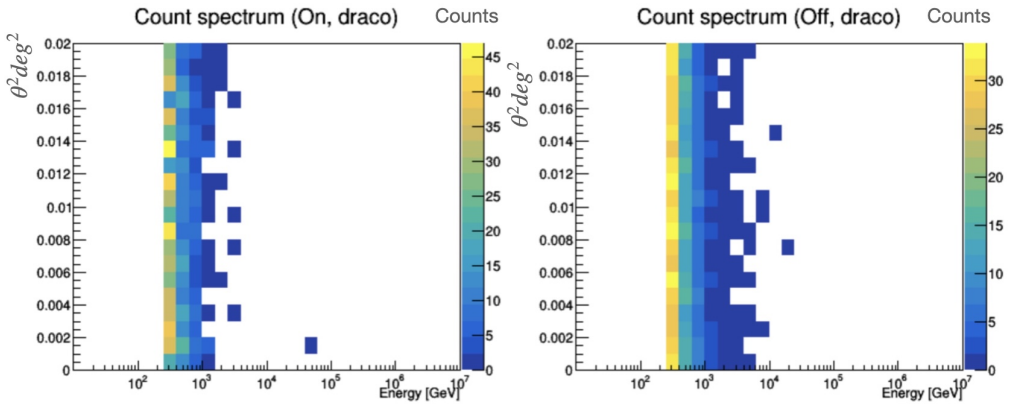

Figure 6.25: N_{on} and N_{off} 2D distribution for Draco.

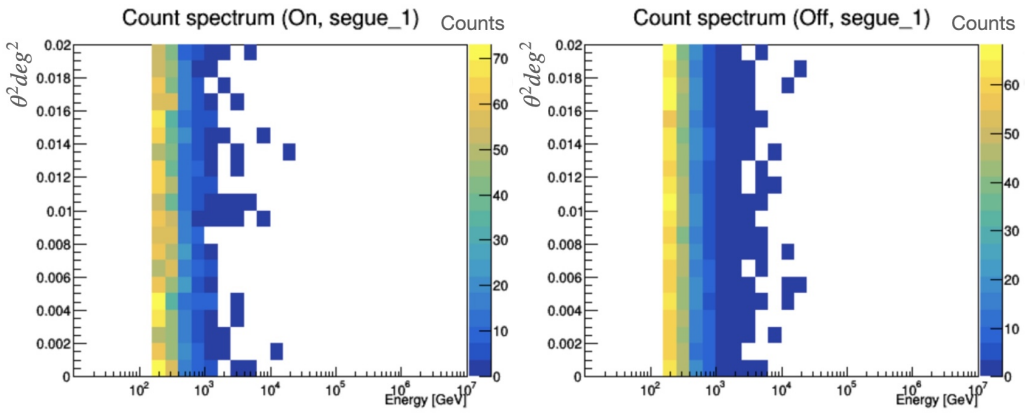

Figure 6.26: N_{on} and N_{off} 2D distribution for Segue1.

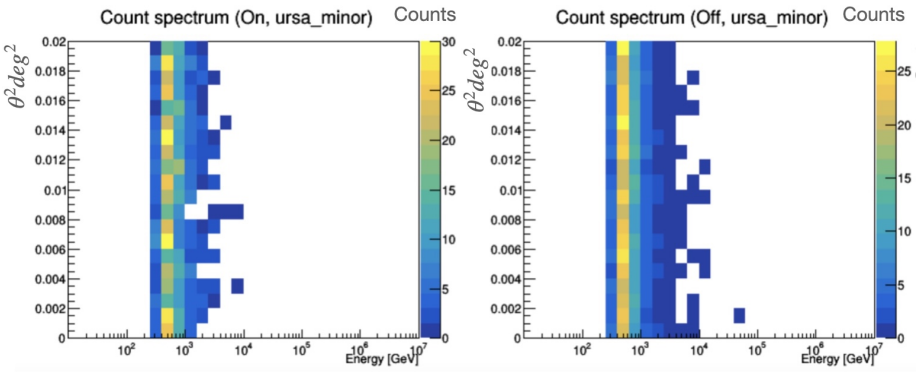

Figure 6.27: N_{on} and N_{off} 2D distribution for Ursa Minor.

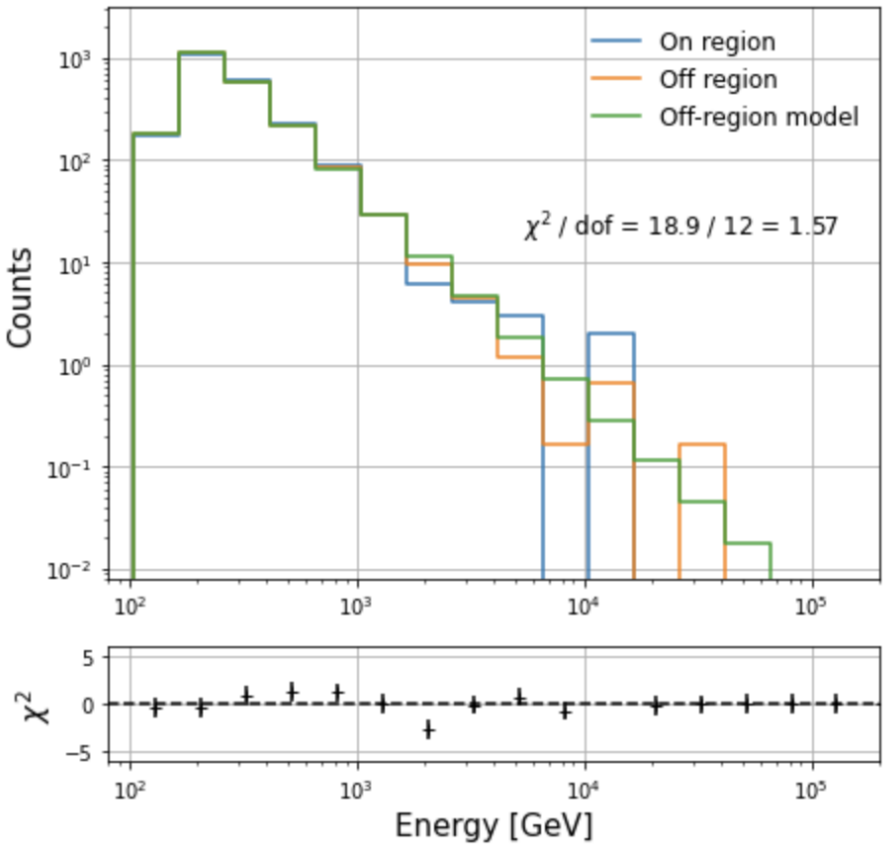

Figure 6.28: N_{on}, N_{off} and $N_{on,model}$ distributions for Segue1 using the 2D analysis cuts.

6.6.5 Expected signal distribution

To make the analysis faster, we pre-calculated the term g, that we simply labeled here as the "expected signal" beforehand. This value is calculated by using Eq 6.12. Examples of g in both 1D and 2D analysis for all dSphs are shown in Fig. 6.29, Fig. 6.30, Fig. 6.31 and Fig. 6.32 when we assumed the cross-section of DM as $10^{-23} cm^3/s$. In order to check the

consistency of g between 1D and 2D analyses, we transformed the 2D histogram into a 1D simply by integrating over θ for a fixed energy. In this way we could compare the two 1D histograms and see if they were in agreement.

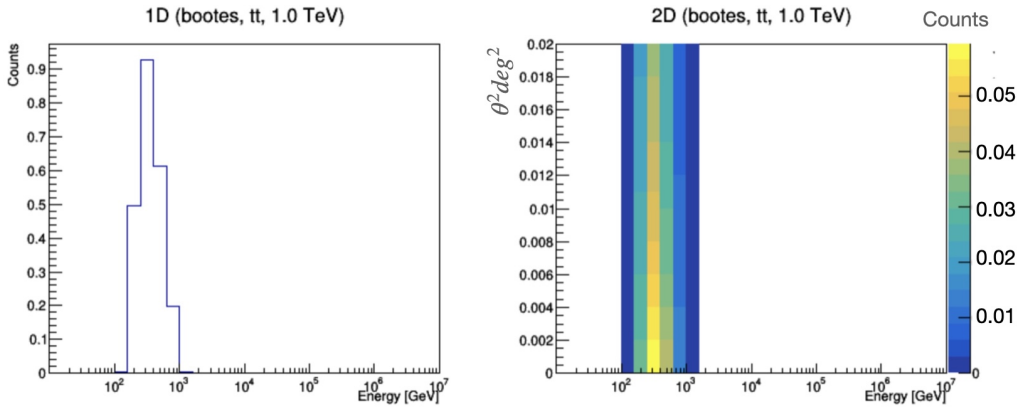

Figure 6.29: 1D and 2D counts distribution of g for Bootes.

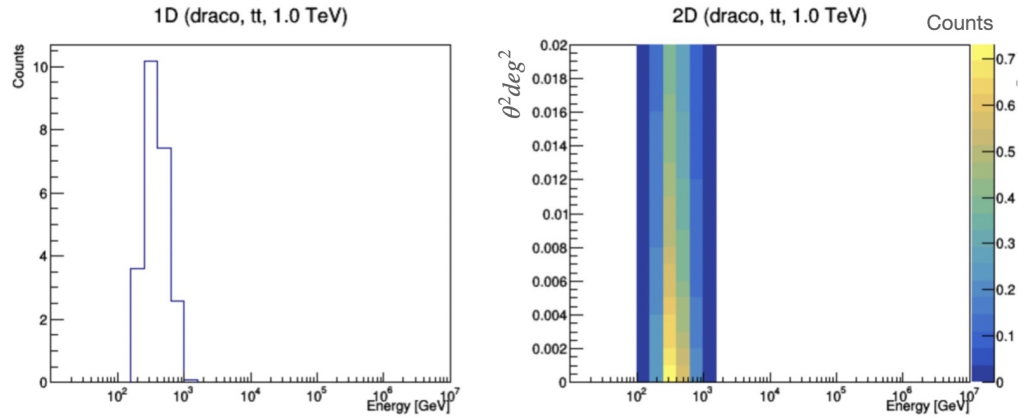

Figure 6.30: 1D and 2D counts distribution of g for Draco.

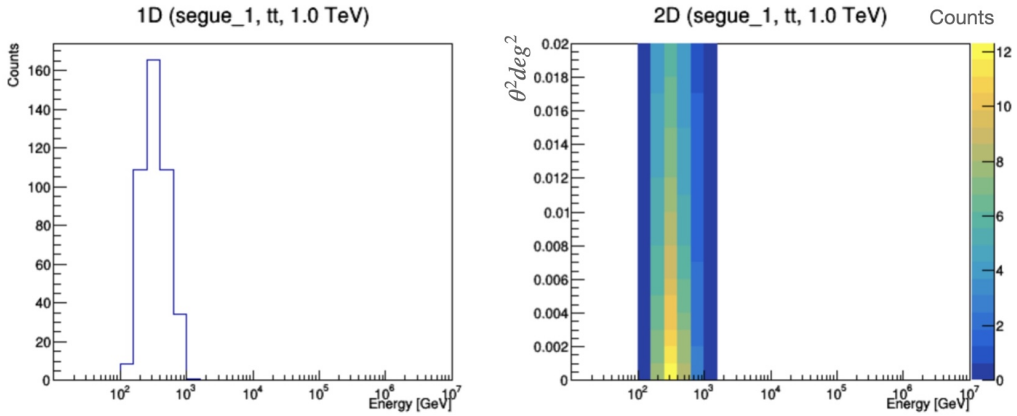

Figure 6.31: 1D and 2D counts distribution of g for Segue1.

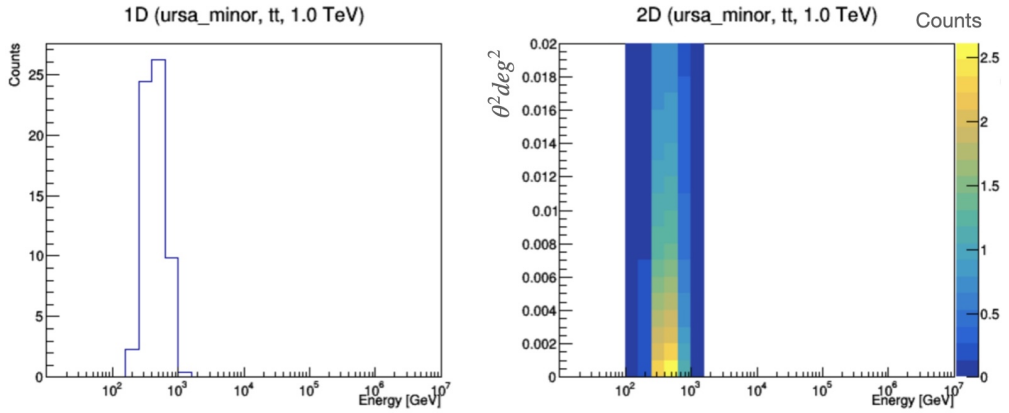

Figure 6.32: 1D and 2D counts distribution of g for Ursa Minor.

6.6.6 Minimization

To perform the MLE analysis, in both 1D and 2D cases, we used a C++ code, to be run in ROOT version 5.34.32. Thanks to ROOT, it was possible to perform the minimization

with the TMinuit tool, already described in Sec. 6.2.1. More specifically, to minimize the likelihood function, we used the "MIGRAD" algorithm, which is the most efficient and complete minimization method within TMinuit, for almost all type of functions [189]. The function minimized was Eq. 6.8 and 6.14 in 1D case and 2D case, respectively.

Three parameters were fixed during the minimization, i.e. the α ratio, the N_{off} and the mass. The other two variables, i.e. the annihilation cross-section and the number of expected background events b, were regarded as free parameters. If the minimisation failed to find its global minimum, we had to modify either the steps width to look for minimum parameters or the range where to look for them. When no DM signal was detected, we set upper limits on the annihilation cross-section within the mass range from 10 Gev to 10^5 GeV (logarithmically even spaced). Once the variables in which the likelihood function reached its minimum value were found by the minimizer, then the sets of parameters that belong to the 2 σ C.L. contour [189] can be found. If the contour is not created due to big uncertainty, we obtained the likelihood profile depending on σ. We took the value of the cross-section at which the likelihood profile was equal to 2.71/2 (Fig. 6.33).

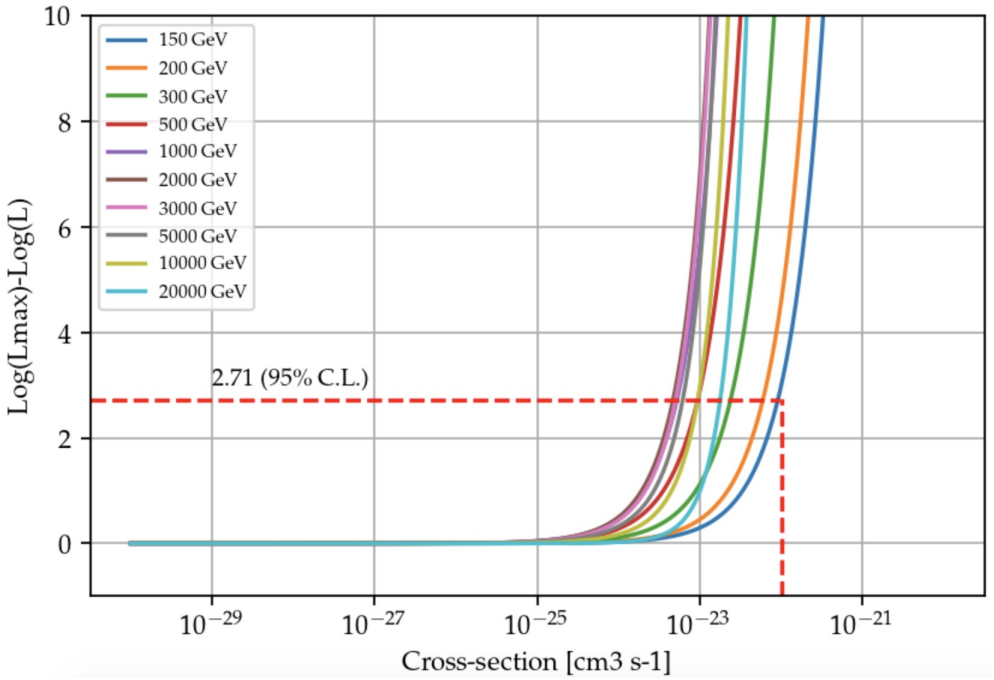

Figure 6.33: An example of how the limit on the cross-section was calculated. Each line corresponds to the likelihood profile per different masses. This was for Segue1 $b\bar{b}$ channel, with 2D cuts.

6.7 Testing the effectiveness of 2D analysis

We performed two simulation studies to address the effectiveness of the 2D analysis, compared to the 1D analysis. Note that this effectiveness study was done by Dr. Donggeun Tak.

Firstly, we checked the effectiveness of the 2D MLE analysis for detecting the DM signal. To test this, we assumed the DM cross-section (high enough to be detected) and produced a simulated on-region distribution, $N_{\rm sim}(E,\theta) = \alpha N_{\rm off}(E,\theta) + g(E,\theta)$; for each channel and

dwarf, we used different $\langle\sigma_v\rangle$ to make TS values obtained from the MLE be high enough (about 20 to 30)[8]. Then, we synthesized events from the simulated on-region distribution, where the number of the synthesized events is obtained from the Poisson fluctuation of $N_{\rm on}$. After that, we performed MLE with the synthesized events. From 1000 realizations, we took the average TS value for each mass. Fig. 6.34[9] shows the comparison between TS values from the 1D and 2D MLE analyses. The left panel of Fig. 6.34 shows that the effectiveness of the 2D method can depend on the DM annihilation channels. Also, the right panel ($\tau^+\tau^-$ for Segue1 and Draco) shows that the effectiveness of the 2D analysis does not depend on which dwarf is being considered. This implies that the 2D MLE analysis can be more effective in detecting a possible DM signal (Fig. 6.34) by a factor of 20-30% (depending on channel and/or source).

[8] For Segue1, we used $10^{-23.8}\mathrm{cm}^3\mathrm{s}^{-1}$ ($\tau^+\tau^-$) and $10^{-22.0}\mathrm{cm}^3\mathrm{s}^{-1}(b\bar{b})$. For Draco, we used $10^{-21.6}\mathrm{cm}^{-3}\mathrm{s}^{-1}$ ($\tau^+\tau^-$).

[9] Thanks/Credits to Dr. Donggeun Tak (donggeun.tak@desy.de). These results were already shown at ICRC2021.

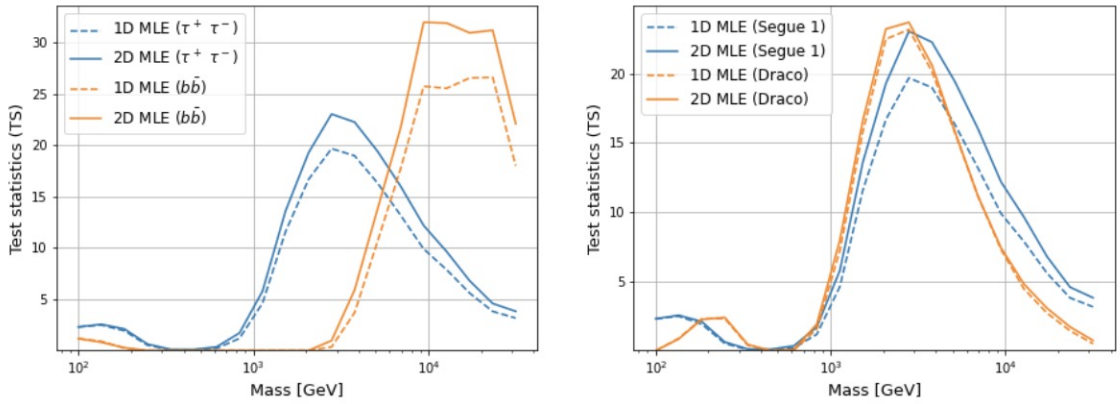

Figure 6.34: Comparing TS as a function of DM mass for 1D and 2D analysis. *On the left*: results for two DM annihilation channels, i.e. $\tau\tau$ and $b\bar{b}$ for Segue1. *On the right*: results for two different dSphs, i.e. Segue1 and Draco. Note that $\langle\sigma_v\rangle$ is set to be different for each channel and each dwarf.

Chapter 7

Results and discussion

In this chapter, we will show results of our analysis already discussed in Sec. 6.2.2 and 6.2.3. As no DM signal was detected, we set constraints on the thermally-averaged[1] velocity-weighted[2] annihilation cross-section σ_v, only for two annihilation channels, i.e. $b\bar{b}$ and $\tau\tau$. We used both the analysis described in Sec. 6.2.2 and Sec. 6.2.3 and compared the corresponding results, which we are going to show in this chapter.

7.1 Comparing results/limits: 1D vs 2D analysis

Fig. 7.1 and Fig. 7.2 show, for all four dSphs and respectively for $\tau\tau$ and $b\bar{b}$ channels, the comparison between 1D and 2D limits. Note that 1D results were obtained by using the conventional 1D analysis with point-like IRFs (i.e. with $\theta^2 = 0.008\ deg^2$, already explained in Sec. 6.2.2 and used in [185]), while the 2D results were obtained by using a 2D likelihood

[1] In Chap. 2, we saw that DM particles had a Maxwell-Boltzmann velocity distribution in the early Universe. Thus, a thermal average of the annihilation cross-section is needed, in order to use it in the Boltzmann equation for the DM relic density.

[2] It is velocity-weighted as it should take into account the fact that the two DM particles are moving with respect to one another.

analysis including the dSphs angular extension information with extended IRFs (i.e. with a looser $\theta^2 = 0.02\ deg^2$, already explained in Sec. 6.2.3) .

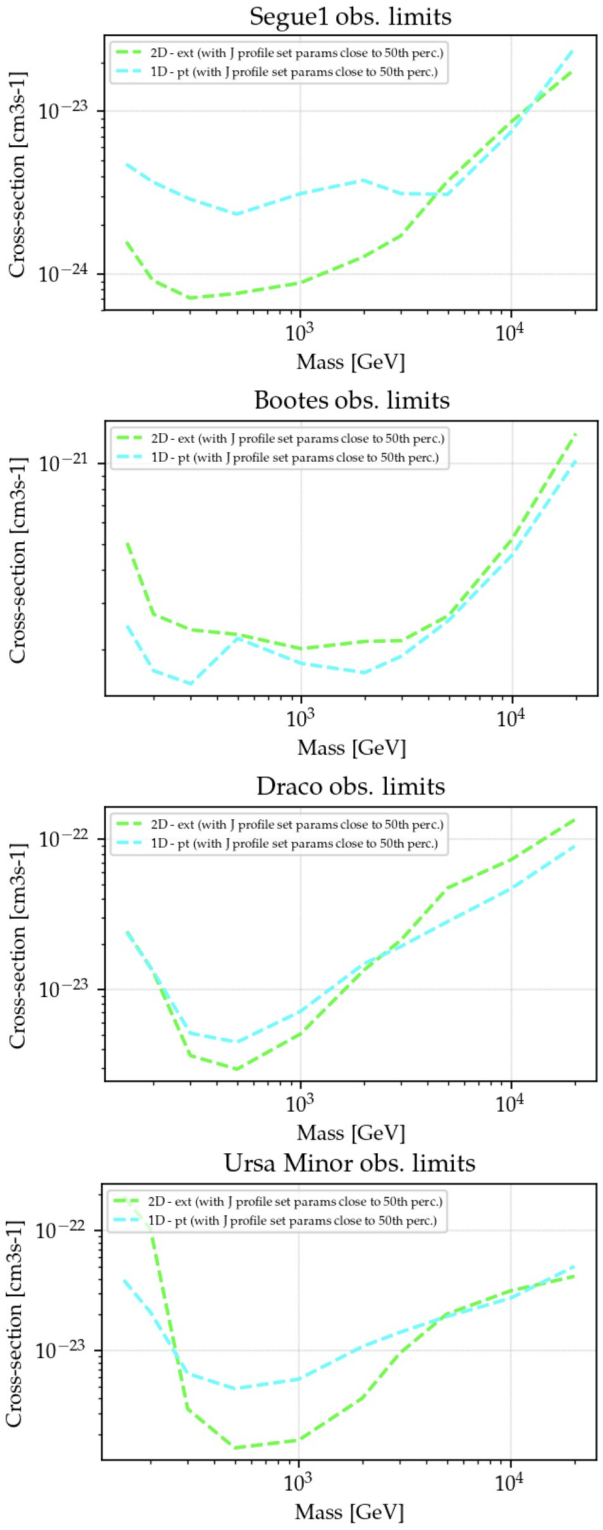

Figure 7.1: Comparison between 1D point-like limits and 2D extended limits for $\tau\tau$ channel, both using the NFW set of parameters which represents the one close to 50th percentile of J-profile.

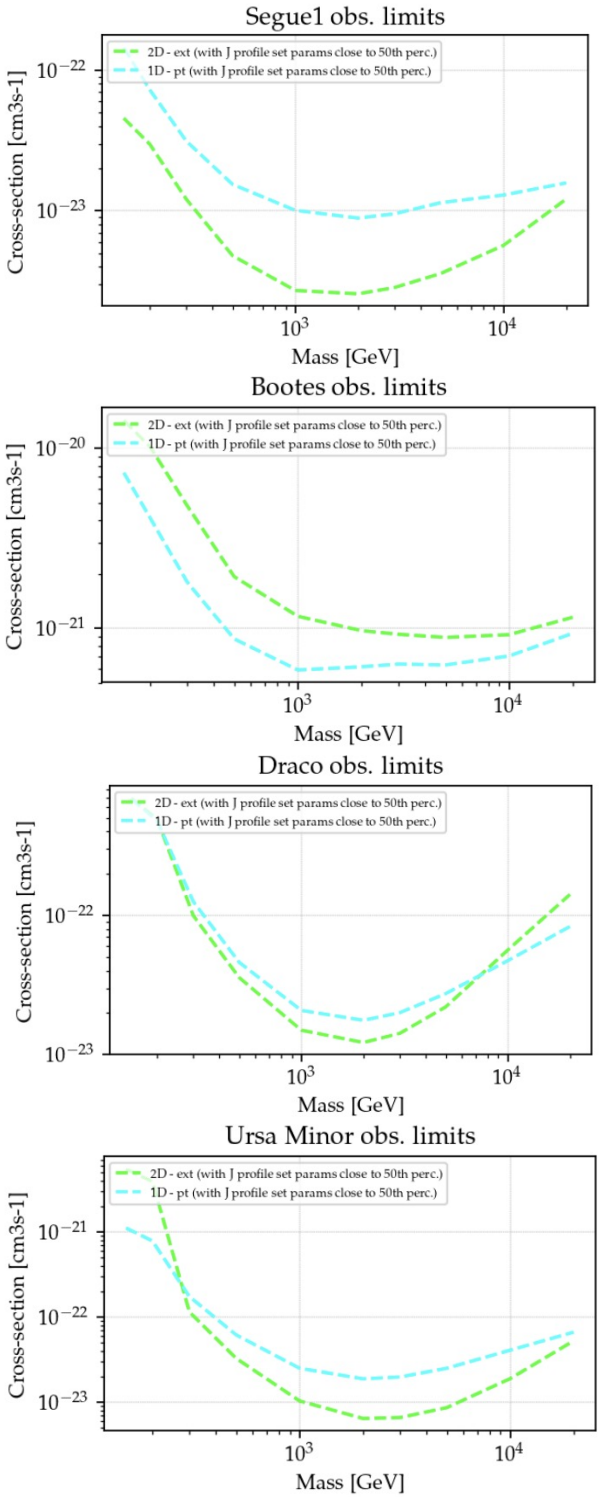

Figure 7.2: Comparison between 1D point-like limits and 2D extended limits for $b\bar{b}$ channel, both using the NFW set of parameters which represents the one close to 50th percentile of J-profile).

We found that, for $b\bar{b}$ channel, it is evident that performing an extended analysis provided more constrained results (green lines in Fig. 7.1 and Fig. 7.2) compared to the standard 1D analysis (light blue lines in the aforementioned figures). This does not occur for the Bootes case. Since it has a smaller dataset and low exposure, the Bootes analysis is done with a poor statistics with low counts. This is why Bootes is less sensitive in the 2D analysis.

About the $\tau\tau$ channel, we could say that the trend observed in this channel is pretty consistent with the one observed in the $b\bar{b}$ channel. However, with the 2D analysis we did not always get this improvement compared to the 1D case, depending on the source and on the DM mass considered. For example, in the mass range between 200 GeV - 3 TeV we can say that the limits obtained with the 2D method are more constrained than the ones obtained with the 1D analysis, for all dSphs except for Bootes (always due to its smaller dataset). This can be alos due to the different cuts used in the analyses: 1D analysis used soft NTel2 cuts, while the 2D one used moderate NTel3 cuts.

Overall, with the 2D analysis an averaged improvement of about 15% can be achieved.

7.2 Systematic uncertainty study

In Sec. 5.4.2, we already saw that systematic uncertainty on the annihilation cross-section limits is mostly due to our imperfect knowledge on the kinematics describing dSphs density profiles. Indeed, multiple realizations of halos reasonably fit the same stellar kinematic data. All other systematic uncertainties are negligible compared to this uncertainty.

The most accurate way to generate the systematic uncertainty band would be to generate a lot of convolved J-profiles with different set of NFW parameters and to compute upper

limits with them. However, due to the computational limitations, we simplified the process. We directly performed three times the limit calculation: one with the median value of the J-profile distribution (Fig. 6.13), the second time with the 16th percentile of the J-profile distribution (to get the upper bound of the systematic band) and the third time with the 84th percentile of the J-profile distribution (to get instead the lower bound). This process is valid because an upper limit is inversely proportional to expected counts for given mass (e.g., Eq. 6.7), and the expected counts are linearly proportional to the convolved J-profile (see Sec. 6.6.5 and Eq. 6.12). In other words, since the convolution is processed beforehand, we can expect that the band from the convolved J-profiles will be present in the upper limits in the same way. We also double-checked this consistency with a smaller dataset, and the two methods were consistent with each other (Fig. 7.3).

We obtained the systematic uncertainty band around the observed limits in the 2D extended analysis, for all dSphs, shown in Fig. 7.4 for the $\tau\tau$ annihilation channel. As it can be noticed, the ultra-faint dSphs Bootes and Segue1 have two of the largest systematic uncertainty bands, due to the low number of independent velocity measurements of each star (only ten in the case of Bootes), as also pointed out in [171, 200]. On the other hand, classical dSphs such as Draco and Ursa Minor have thinner systematic uncertainty band as their kinematic dataset available is richer.

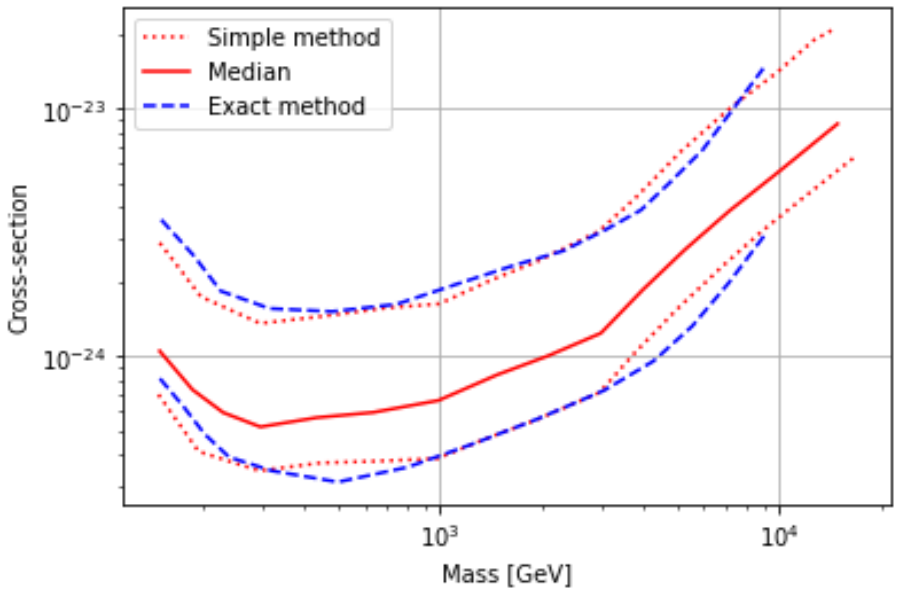

Figure 7.3: Checking the systematic uncertainty calculation (for Segue1, 2D analysis) using two methods. Blue band represents the more accurate way to estimate the systematic band, as explained in the text. The red line represents the observed limit. The red dashed lines represent the limits obtained using the 16th percentile (upper line of the "band") and the 84th percentile (lower line of the "band") of the J-profile distribution. The blue lines, instead, represent the edges of the systematic band obtained by calculating the cross-section upper limits with different sets of NFW parameters.

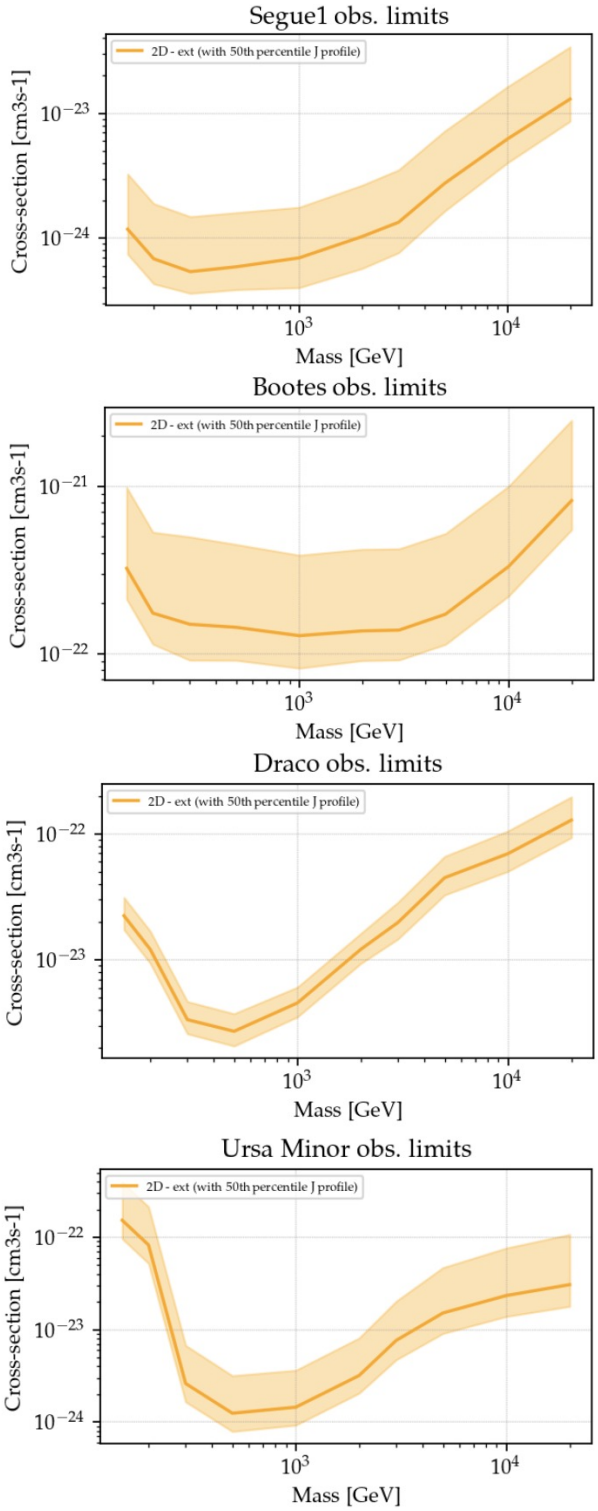

Figure 7.4: $\tau\tau$ limits with systematic band for all dSphs.

Another interesting aspect that is worth to be quantified in the future would be to compute the statistical fluctuations on cross-section annihilation limits, induced by our finite event statistics/dataset (which we mentioned already was less significant than the systematic uncertainty).

To do so, we should have a look at the distribution of the test statistic under the background-only hypothesis. No events in the ON region should be used. In Eq. 6.11 it could be possible to let N_{on} fluctuating around N_{off}, and then to fill the N_{on} energy distribution from N_{off} energy distribution. However, this work has not been done in this thesis.

7.3 Comparing with other experiments

We compared Segue1 $\tau\tau$ limits obtained with our 1D and 2D analyses with the MAGIC [194], HAWC limits [201] and previous VERITAS results [185], in Fig. 7.5. In Fig. 7.6, we compared our results for the $b\bar{b}$ channel to the MAGIC limit [194].

Table 7.1: This table shows, per VERITAS (this work and [185]'s work), HAWC [201] and MAGIC [194], the size of the ON region, the exposure time and the statistical method used to calculate the upper limits on the annihilation cross-section for Segue1 data.

Experiment	ON-region size (θ^2 cut) $[deg^2]$	Exposure time	Analysis method -
Our work	0.02	184 hrs	MLE (unbinned) with EventDisplay
VERITAS2017	0.03	184 hrs	Event-weighting method with VEGAS
HAWC	0.2	507 days	MLE (binned)
MAGIC	0.015	157 hrs	MLE (binned)

Tab. 7.1 summarizes the dwarf observations carried on by all the three experiments. We will talk about the MAGIC observatory in Sec. 8.2.3. Here we will just briefly describe the dSph analysis on Segue1 performed by MAGIC in [194]. They processed Segue1 data observed between January 2011 until February 2013, for a total observation time of 157.9 hrs of good-quality data. They performed a binned MLE analysis taking into consideration the spectral signatures, as shown in [202]. They used a θ^2_{cut} optimized for a point-like source, i.e. $\theta^2_{cut} = 0.015\ deg^2$, claiming that it can be confirmed that the sensitivity could be improved by up to 10% with looser θ^2_{cut} than the one they used. They also modeled the DM density using the Einasto profile, assuming the scale radius $r_s = 0.15$ kpc, the scale density $\rho = 1.1 \times 10^8\ M_\odot kpc^{-3}$ and the slope $\alpha = 0.30$ (see Sec. 5.3). No DM significant excess was detected, thus they set 95% C.L. upper limits within the mass range of 100 GeV - 10 TeV, on the annihilation cross-section for the following annihilation channels: W^+W^-, ZZ, $b\bar{b}$, $\tau\tau$, $\gamma\gamma$, $t\bar{t}$ and $\mu^+\mu^-$. They as well assumed that each of these final states has a branching ratio of 100%. The most constraining limit was obtained for the $\tau\tau$ channel, corresponding to a DM annihilation cross-section upper limit of: $\langle\sigma_{ann}\rangle < 1.2 \times 10^{-24} cm^3 s^{-1}$ at $M_{DM} = 500$ GeV.

HAWC instrument will also briefly described in Sec. 8.2.5. In [201], they analysed data from 15 dSphs. Among those, there was Segue1, for which they had a total exposure time of 507 days (from November 2014 to June 2016). They assumed that dSphs were point-like sources, using a $\theta^2_{cut} = 0.2\ deg^2$. The NFW profile was used to model the DM density of their dSphs, using the median density parameters provided by [171]. A binned MLE analysis was performed too. They did not detect any significant γ-ray excess, therefore they set 95% C.L. upper limits on the DM annihilation cross-section, within the mass range of 1 TeV - 100 TeV.

For previous VERITAS analysis on dSphs, [185] used the same dataset as we used for this thesis work, so observations on Segue1 were taken from 2007 to 2013, resulting in 184 hrs total exposure time. They, as well, applied cuts optimized for the detection of point-like sources, valid for the other VERITAS analysis reconstruction software, i.e. VEGAS[3]. A different background estimation model was used, i.e. the so-called "crescent background model", where the background is supposed to be extracted from a ring similarly to the ring background model we already saw, but in this case the ring is centered on the tracking position. The NFW profile was used from [171] too. They adopted a novel analysis method called "event weighting" [203]. According to this method, each event in the ON region is assigned a "weight", w, which depends on three variables: its reconstructed energy, its reconstructed angular distance from the center of the dSph and its FOV. The TS value they calculated was then the sum of the weights from all events.

As we can see, with our 2D analysis we did get more constrained upper limits (for some cases, even of 1 order of magnitude) with respect to other point-like analysis performed by other experiments in all the cases shown in here. For example, this happens if we compare our 2D limits with the one obtained by MAGIC, even though the exposure times are relatively similar. In the case of HAWC, it has lower effective areas compared to those of VERITAS. Also, it is a survey observatory, so that the true exposure time on the source can be lower than 507 days; i.e., HAWC covers 2/3 of the full sky every day. With these two effects, HAWC limits are much poorer than ours. Also, the upper limits we obtained with our 1D analysis are comparable to the published VERITAS ones.

[3] As already mentioned, the point-like cuts used in VEGAS and *EventDisplay* are different, because they have different PSFs from different reconstruction process.

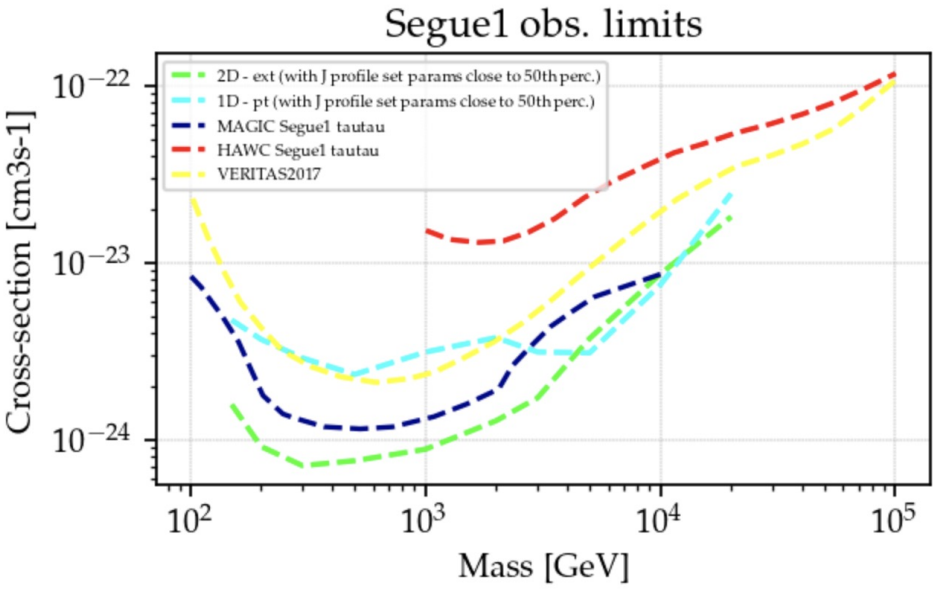

Figure 7.5: Comparing our results about $\tau\tau$ upper limits with MAGIC, HAWC and previous VERITAS limit for Segue1.

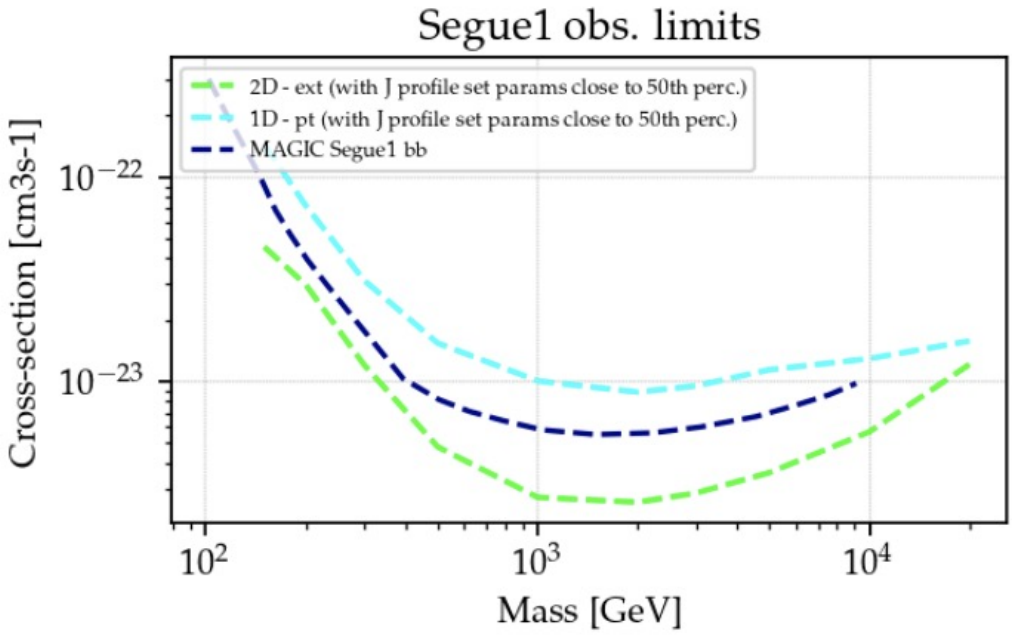

Figure 7.6: Comparing our results about $b\bar{b}$ upper limits with MAGIC for Segue1.

Chapter 8

Multi-instrument dark matter limits from dwarf spheroidal galaxies

One of the projects included in my work was to combine for the first time VERITAS dSphs data used in this work (Chap. 6 and 7) with dSphs data from other four different γ-ray instruments, i.e. MAGIC, H.E.S.S., *Fermi*-LAT and HAWC. Our goal was to maximise the sensitivity up to higher and lower energies in the DM search considering the largest mass range ever selected. The idea was that each instrument could keep its own analysis reconstruction methods, softwares, datasets and instrument response functions in order to share data among us only at the "high-level". In other words, we simply used a common DM spectral and morphological models and a common statistical analysis procedure. Each collaboration performed a likelihood analysis on its own (per each annihilation channel, DM mass and source, separately). Then, the test statistic values versus the velocity-weighted annihilation cross-section values were shared and combined into a global joint likelihood function in order to put constraints on the DM annihilation cross-sections. The methodology used for this combination is well explained and justified in [138].

The results that will be showed in this thesis are still the preliminary ones, i.e. only two channels (bb and $\tau^+\tau^-$) will be shown.

8.1 Datasets

For this combination work, data from 20 dSphs were used. Some of them were observed by more than one instrument. These data were previsouly published individually by each experiment. Tab 8.1 shows the list of dSphs used in this work and, per each observed dSph, the experiment that performed the observation, the heliocentric distance to the Earth and the J-factor measured taken from [171], truncated at the outermost star member with its $\pm 1\sigma$ uncertainty.

Source name	Experiments (exp. time)	Distance (kpc)	$\log_{10} J$ $\log_{10}(\mathrm{GeV}^2\mathrm{cm}^{-5}\mathrm{sr})$
Bootes I	*Fermi*-LAT (2.6), HAWC, VERITAS (14)	66	$18.24^{+0.40}_{-0.37}$
Canes Venatici I	*Fermi*-LAT (2.9)	218	$17.44^{+0.37}_{-0.28}$
Canes Venatici II	*Fermi*-LAT (2.9), HAWC	160	$17.65^{+0.45}_{-0.43}$
Carina	*Fermi*-LAT (3.1), H.E.S.S. (23.7)	105	$17.92^{+0.19}_{-0.11}$
Coma Berenices	*Fermi*-LAT (2.7), HAWC, H.E.S.S. (11.4), MAGIC (49.5)	44	$19.02^{+0.37}_{-0.41}$
Draco	*Fermi*-LAT (3.8), HAWC, MAGIC (52.1), VERITAS (49.8)	76	$19.05^{+0.22}_{-0.21}$
Fornax	*Fermi*-LAT (2.7), H.E.S.S. (6.8)	147	$17.84^{+0.11}_{-0.06}$
Hercules	*Fermi*-LAT (2.8), HAWC	132	$16.86^{+0.74}_{-0.68}$
Leo I	*Fermi*-LAT (2.5), HAWC	254	$17.84^{+0.20}_{-0.16}$
Leo II	*Fermi*-LAT (2.6), HAWC	233	$17.97^{+0.20}_{-0.18}$
Leo IV	*Fermi*-LAT (2.4), HAWC	154	$16.32^{+1.06}_{-1.70}$
Leo T	*Fermi*-LAT (2.6)	417	$17.11^{+0.44}_{-0.39}$
Leo V	*Fermi*-LAT (2.4)	178	$16.37^{+0.94}_{-0.87}$
Sculptor	*Fermi*-LAT (2.7), H.E.S.S. (11.8)	86	$18.57^{+0.07}_{-0.05}$
Segue I	*Fermi*-LAT (2.5), HAWC, MAGIC (158), VERITAS (92)	23	$19.36^{+0.32}_{-0.35}$
Segue II	*Fermi*-LAT (2.7)	35	$16.21^{+1.06}_{-0.98}$
Sextans	*Fermi*-LAT (2.4), HAWC	86	$17.92^{+0.35}_{-0.29}$
Ursa Major I	*Fermi*-LAT (3.4), HAWC	97	$17.87^{+0.56}_{-0.33}$
Ursa Major II	*Fermi*-LAT (4.0), HAWC, MAGIC (94.8)	32	$19.42^{+0.44}_{-0.42}$
Ursa Minor	*Fermi*-LAT (4.1), VERITAS (60.4)	76	$18.95^{+0.26}_{-0.18}$

Table 8.1: Summary of the relevant properties of the dSphs included in the combination of *Fermi*-LAT, HAWC, H.E.S.S., MAGIC, and VERITAS likelihood functions. The list of the observed dwarf galaxies is presented in column 1 with the instruments that performed the observations in column 2 (and in brackets the exposure time, in hrs, relative to the instrument, except for Fermi-LAT, whose exposure time is given times its effective area, so it is expressed in $[sm^2]$. Their heliocentric distance and J factor with their estimated $\pm1\sigma$ uncertainties are listed in columns 3 and 4 respectively. The J factors are given for a source extension truncated at the outermost observed star with their estimated $\pm1\sigma$ uncertainties. HAWC has, for all dSphs, an exposure time of 507 days for the whole sky.

8.2 Instruments involved

As already mentioned, for this combination work, the widest energy range was considered, i.e. from lower energies (few tens of GeV) thanks to the satellite experiment Fermi-LAT, up to higher energies thanks to HAWC ($\sim$ 100 TeV). The middle energy range (from 50 GeV up to 80 TeV) was covered by three IACTs: MAGIC, H.E.S.S. and VERITAS.
Let's briefly review the main properties of each of these instruments and their analysis details.

8.2.1 *Fermi*-LAT

Fermi Large Area Telescope (LAT) is a satellite instrument operating since 2008 (illustrated in Fig 8.1).

Figure 8.1: The Fermi-LAT instrument.

It is sensitive to γ rays within the energy range from 20 MeV to more than 300 GeV. Its FoV is about 2.4 sr and it surveys and scans the entire sky every 3 hours. The energy resolution of *Fermi*-LAT at 1 GeV is 10% and it reaches its minimum at 10 GeV where it is 5%. Its angular resolution for one photon is 1° at 1 GeV. More info on this instrument can be found in [204].

For this combination project, *Fermi*-LAT shared data analysed in 10 years of Pass 8 data [1], from April 8th 2008 to March 3rd 2018. They selected SOURCE class events, applying the basic quality filter cuts. The response functions used were $P8R2\_SOURCEVETO\_V2$. The energy range selected was from 0.3 to 1000 GeV, with a zenith angle cut $< 100°$ from 0.3 to 1 GeV, and with a a zenith angle cut $< 105°$ for energies higher than 1 GeV. Background was modeled after sources reported in the 8 year source catalog (4FGL), and they included also the latest released interstellar emission model (IEM)[2]. They analysed the $12° \times 12°$ regions of interest centered on the dSphs position, with a pixel size of 0.08°. They included background model sources located in a region $14° \times 14°$ in order to include also sources at most 1° outside their region of interest. Tools used were version 0.18.0 of Fermipy and 1.2.3 of the Fermitools. Fermi-LAT observed all dSphs present in Tab. 8.1. More detailed on their dSphs analysis can be found in [205, 206, 207].

8.2.2 H.E.S.S.

The High Energy Stereoscopic System (H.E.S.S.) is an array of five atmospheric Cherenkov telescopes, located in the Khomas Highland of Namibia, at an altitude of 1800 m (Fig 8.2).

[1] For more info on Pass8 data, see: https://fermi.gsfc.nasa.gov/ssc/data/analysis/documentation/Pass8_usage.html

[2] More info on: *https://fermi.gsfc.nasa.gov/ssc/data/analysis/software/aux/4fgl/Galactic_Diffuse_Emission_Model_for_the_4FGL_Catalog_Analysis.pdf*.

Figure 8.2: The H.E.S.S. array in the Khomas Highland of Namibia.

Four telescopes have a diameter of 12 m and are located at the corner of a 200 meter side square (CT1-4). The fifth telescope has a 28 diameter and it is at the center of the square. Its energy resolution is about 10% and angular resolution of 0.06 at 68% containment radius for energies higher than 200 GeV. Its FoV is of 5°. Its point-like source flux sensitivity is about $10^{-13} cm^{-2} s^{-1}$ above 1 TeV. It can get a 5σ detection in 25 hrs with a zenith angle of 20°. Data were reconstructed following a template-fitting technique explained in [208]. H.E.S.S. shared data from the following dSphs: Coma Berenices and Fornax (observed between 2010 to 2013 and in 2010, respectively), Carina and Sculptor (observed between January 2008 and December 2009), for a total observation time of 54 hrs. Data were taken with CT1-4-array requiring that at least two telescopes could detect the events. They used a wobble observation mode [125], with an offset of 0.7° from the target position. The ON region is defined as a disk centered at the nominal position of the dSph, with a radius of 0.1°. To estimate the residual background in the ON region, they used the reflected background model described in here [133]. For their statistical analysis, they used the

approach described in here [197]. Official H.E.S.S. software packages were used for the analysis, i.e. ParisAnalysis and HAP [208, 209].

8.2.3 MAGIC

The Florian Goebel Major Atmospheric Gamma-ray Imaging Cherenkov (MAGIC) telescopes is an array of two IACTs located at the Roque de los Muchachos Observatory on the Canary Island of La Palma, Spain (Fig 8.3).

Figure 8.3: The MAGIC array located at the Roque de los Muchachos Observatory on the Canary Island of La Palma.

Each telescope has diameter of 17 m and a FoV of 3.5°. MAGIC can detect γ rays with energy higher than 30 GeV. Its sensitivity above 220 GeV for 50 hrs of observations of a point-like source is $\sim 0.66\%$ of the flux of the Crab Nebula with an associated energy resolution of about 16% and an angular resolution of about 0.07°. For energies lower than 100 GeV, MAGIC has an angular resolution of 0.15° and a 5.7% differential sensitivity of the Crab Nebula flux for 50 hrs of observation below 30°. MAGIC data are from Segue1 (observed from 2011 to 2013), Ursa Major II (observed from 2014 to 2016), Draco (observed from March to September 2018) and Coma Berenices (from January to June 2019), with a total observation time of 354 hrs. For different observations epochs, different IRFs were used. The software used was MARS [210].

8.2.4 VERITAS

For a complete overview on the VERITAS observatory, we would redirect the reader to Chap. 4.

For this combination analysis, only published VERITAS data were used (published in [185]), i.e. the same dataset used as well for this thesis work. However, in [185], the *VEGAS* pipeline for analysis and reconstruction software [187] was used. On the other hand, I used exactly the same eventlists and IRFs used in the aforementioned analysis and specifically adapted to the VEGAS software.

8.2.5 HAWC

The High-Altitude Water Cherenkov observatory (HAWC) is located at Sierra Negra, Mexico, at 4100 m above the sea level (see Fig 8.4).

Figure 8.4: The HAWC observatory, located at Sierra Negra, Mexico.

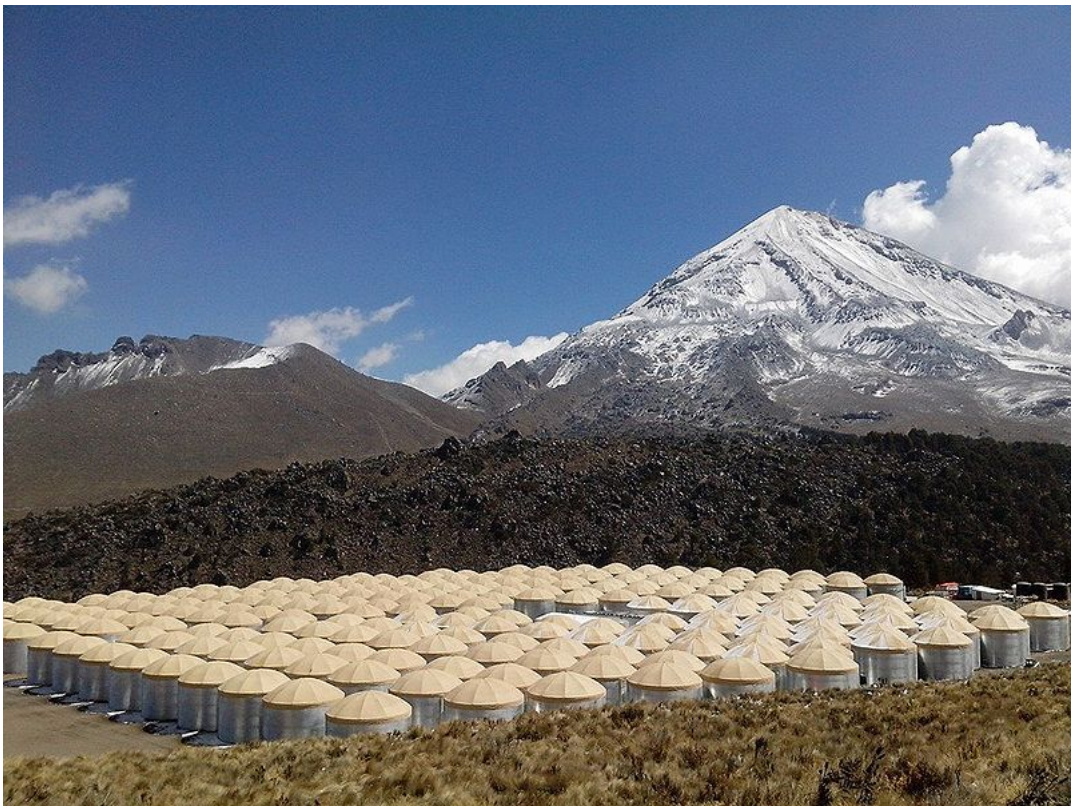

Its energy range is between 300 GeV and 100 TeV. It is composed by 300 water Cherenkov detectors (WCD) covering an area of 22000 m^2. It is operating since August 2013. Its angular reoslution varies from 1° at 1 TeV to 0.2° at $>$ 30 TeV.

For this combination work, HAWC shared data from all dSphs summarized in Table 8.1, excluding Ursa Minor (because it was expected to extend beyond HAWC FoV) and Triangulum II, due to its large uncertainties in the DM content. Its dSphs analysis was already presented in [207].

8.3 DM signal from dSphs

In Chap. 5, we already saw that the differential flux of γ rays from DM self-annihilation is described by Eq. 5.1, and it depends on the velocity-weighted cross-section σ_ν, the mass of the DM particle, the differential spectrum from DM signal per annihilation (weighted by its branching ratio per each final state) and the J-factor. In this combination work, we set limits on the annihilation cross-section using the J-factor estimation from [171] (here "GS" set). In this preliminary work, we studied only two channels ($b\bar{b}$ and $\tau^+\tau^-$) out of the seven annihilation ones planned to investigate that will be part of the future corresponding paper[3] (i.e. W^+W^-, Z^+Z^-, $b\bar{b}$, $t\bar{t}$, e^+e^-, $\mu^+\mu^-$, $\tau^+\tau^-$ and mono-energetic $\gamma\gamma$ channel). Here we also assumed a 100% branching ratio. The mass range considered was from 5 GeV to 100 TeV. The DM spectrum in Eq. 5.1 is taken from [141], including electroweak corrections.

8.4 Joint likelihood analysis

We performed a maximum likelihood analysis and, for each annihilation channel and DM mass, we computed the profile likelihood ratio λ as a function of the annihilation cross-section σ_v defined in the following way:

$$\lambda\left(\langle\sigma_v\rangle|\boldsymbol{\mathcal{D}}_{\rm dSphs}\right) = \frac{\mathcal{L}\left(\langle\sigma_v\rangle;\hat{\hat{\boldsymbol{\nu}}} \mid \boldsymbol{\mathcal{D}}_{\rm dSphs}\right)}{\mathcal{L}\left(\widehat{\langle\sigma_v\rangle};\hat{\boldsymbol{\nu}} \mid \boldsymbol{\mathcal{D}}_{\rm dSphs}\right)}, \tag{8.1}$$

[3] The results shown in this thesis are the ones already presented at ICRC2021.

where $\boldsymbol{\mathcal{D}}_{\rm dSphs}$ is our set of dSphs observations, ν is the nuisance parameters, $\widehat{\langle\sigma_v\rangle}$ and $\hat{\boldsymbol{\nu}}$ are the values that globally maximise the total joint likelihood function $\mathcal{L}$ and $\hat{\hat{\boldsymbol{\nu}}}$ is the values that maximise $\mathcal{L}$ for a fixed value of $\langle\sigma_v\rangle$.

The global joint likelihood function (i.e. summing all instruments and dSphs) $\mathcal{L}$ is defined by partial likelihood functions corresponding to each dSph l (and its corresponding J-factor whose likelihood value is $\mathcal{J}_l$) and each instrument, with the following relation:

$$\mathcal{L}\left(\langle\sigma v\rangle;\boldsymbol{\nu}\mid\boldsymbol{\mathcal{D}}_{\rm dSphs}\right)=\prod_{l=1}^{N_{\rm dSphs}}\mathcal{L}_{{\rm dSph},l}\left(\langle\sigma v\rangle;J_l,\boldsymbol{\nu_l}\mid\boldsymbol{\mathcal{D}_{l,}}_{\rm measured}\right)\times\mathcal{J}_l\left(J_l\mid J_{l,\rm obs},\sigma_{\log J_l}\right), \quad (8.2)$$

where $\boldsymbol{\mathcal{D}_{l,}}_{\rm measured}$ is the set of γ-ray observations for the l-th dSph, J_l is the total J-factor of the l-th dSph as defined in Eq. 5.2 and it has unknown value, $\boldsymbol{\nu_l}$ is the set of nuisance parameters influencing the γ-ray observations of the l-th dSph (excluding J_l), $\log_{10} J_{l,\rm obs}$ and $\sigma_{\log J_l}$ (which can be found in Tab. 8.1) are obtained by fitting a log-normal function of $J_{l,\rm obs}$ to the posterior distribution of J_l [204] and $N_{\rm dSphs}$ is the number of dSphs (in our case, 20).

The term $\mathcal{J}_l$ can be written as:

$$\mathcal{J}_l\left(J_l\mid J_{l,\rm obs},\sigma_{\log J_l}\right)=\frac{1}{\ln(10)J_{l,\rm obs}\sqrt{2\pi}\sigma_{\log J_l}}\exp\left(-\frac{\left(\log_{10}J_l-\log_{10}J_{l,\rm obs}\right)^2}{2\sigma^2_{\log J_l}}\right). \quad (8.3)$$

As can be noted in Eq. 5.1, the quantities $\langle\sigma v\rangle$ and J_l are degenerate in the calculation of $\mathcal{L}_{{\rm dSph},l}$, which depends on $\frac{d\Phi}{dE}$. Consequently, as claimed in [138], it is sufficient to compute $\mathcal{L}_{{\rm dSph},l}$ as a function of $\langle\sigma v\rangle$ for a fixed value of J_l . As $J_{l,\rm obs}$, we used $J_{l,\rm obs}(\mathcal{GS})$ reported in Tab. 8.1, to generate the profile of $\mathcal{L}$ with respect to J_l. This degeneracy

implies that for any $J'_l \neq J_{l,\mathrm{obs}}$ (where $J'_l = J_{l,\mathrm{obs}}(B \neq \mathcal{GS})$):

$$\mathcal{L}_{\mathrm{dSph},l}\left(\langle\sigma v\rangle; J'_l, \boldsymbol{\nu_l} \mid \boldsymbol{\mathcal{D}_{l,\mathrm{measured}}}\right) = \mathcal{L}_{\mathrm{dSph},l}\left(\frac{J'_l}{J_{l,\mathrm{obs}}}\langle\sigma v\rangle; J_{l,\mathrm{obs}}, \boldsymbol{\nu_l} \mid \boldsymbol{\mathcal{D}_{l,\mathrm{measured}}}\right), \tag{8.4}$$

which is a re-scaling operation that reduces the computational needs of the profiling operation, as it is:

$$\mathcal{L}\left(\langle\sigma v\rangle; \hat{\boldsymbol{\nu}} \mid \boldsymbol{\mathcal{D}}_{\mathrm{dSphs}}\right) = \prod_{l=1}^{N_{\mathrm{dSphs}}} \max_{J_l}\left[\mathcal{L}_{\mathrm{dSph},l}\left(\langle\sigma v\rangle; J_l, \hat{\boldsymbol{\nu}}_{\boldsymbol{l}} \mid \boldsymbol{\mathcal{D}_{l,\mathrm{measured}}}\right) \times \mathcal{J}_l\left(J_l \mid J_{l,\mathrm{obs}}, \sigma_{\log_{J_l}}\right)\right]. \tag{8.5}$$

Thus, we used Eq. 8.4 to combine data from different γ-ray instruments and observed dSphs via tabulated values of $\mathcal{L}_{\mathrm{dSph},l}$, or λ from Eq. 8.1 (we chose this one to be shared) versus $\langle\sigma v\rangle$. For a fixed value of J_l, the partial $\mathcal{L}_{\mathrm{dSph},l}$ was computed and profiled with respect to all instrumental nuisance parameters $\boldsymbol{\nu_l}$.

For each dSph, $\mathcal{L}_{\mathrm{dSph},l}$ can be written as the product of the likelihood terms describing the N_{exp} observations performed with any of our instruments (k):

$$\mathcal{L}_{\mathrm{dSph},l}\left(\langle\sigma v\rangle; J_l, \boldsymbol{\nu_l} \mid \boldsymbol{\mathcal{D}_{l,\mathrm{measured}}}\right) = \prod_{k=1}^{N_{\mathrm{exp}}} \mathcal{L}_{lk}\left(\langle\sigma v\rangle; J_l, \boldsymbol{\nu_{lk}} \mid \boldsymbol{\mathcal{D}_{lk,\mathrm{measured}}}\right), \tag{8.6}$$

where each $\mathcal{L}_{lk}$ term refers to an observation of the l-th dSph with the associated k-th instrument IRFs and N_{exp} depends on the dSph. Finally, values of Eq. 8.1 were computed as function of $\langle\sigma v\rangle$, whose range is defined between 10^{-28} and $10^{-18}\mathrm{cm}^3\mathrm{s}^{-1}$, with 1001 logarithmically spaced values, from 5 GeV to 100 TeV (according to [141]).

One of the biggest advantages of this combination method is that each instrument analysed separately its own data without sharing low-level information, such as event-lists tables or

IRFs. But at the same time, as many common assumptions as possible were adopted: a common statistical approach and common DM spectra.

However, given the diversity of these instruments, the general likelihood function had to be adjusted for the observations performed. On one hand, Fermi-LAT, H.E.S.S., HAWC and MAGIC used a binned likelihood analysis given by the function:

$$\mathcal{L}_{lk}\left(\langle\sigma v\rangle; J_l, \boldsymbol{\nu_{lk}} \mid \boldsymbol{\mathcal{D}_{lk}}\right) = \prod_{i=1}^{N_{\mathrm{E}'}} \prod_{j=1}^{N_{\mathrm{P}'}} \Big[\mathcal{P}(s_{lk,ij}(\langle\sigma v\rangle, J_l, \boldsymbol{\nu_{lk}}) + b_{lk,ij}(\boldsymbol{\nu_{lk}}) \mid N_{lk,ij})\Big] \times \mathcal{L}_{lk,\boldsymbol{\nu}}\left(\boldsymbol{\nu_{lk}} \mid \boldsymbol{\mathcal{D}_{\nu_{lk}}}\right), \tag{8.7}$$

where $N_{E'}$ and $N_{P'}$ are the number of bins in, respectively, reconstructed energy and arrival direction, $\mathcal{P}$ is the Poisson PDF of the γ-ray candidate events $N_{lk,ij}$ observed in the i-th energy bin and j-th arrival direction bin, s_{ij} (b_{ij}) is the expected mean number of signal (background) events (produced by DM annihilation, assuming that the expected number of $N_{lk,ij}$ is the sum of $s_{ij} + b_{ij}$) and $\mathcal{L}_{lk,\boldsymbol{\nu}}$ is the likelihood term taking into account the extra nuisance parameters ν_{lk} that vary per each instrument. This instrument-dependence comes also from the different method used in the background estimation. For example, *Fermi*-LAT and HAWC use a template fitting approach in order to model the background [211]. while the IACTs (H.E.S.S., MAGIC, VERITAS) utilize ON/OFF measurements [133] to estimate the background.

For this combination work, the combined likelihood was calculated, as cross-check, with two different public analysis software packages, i.e. `gLike` [212] and `LklCombiner` [213], that provide the same results. GLike was previously used by [138] to combine MAGIC and Fermi-LAT dSphs data. LklCombiner, instead, was created just to cross-check these multi-instrument analysis results.

Details on the VERITAS analysis

This subsection is intended to explain the VERITAS contribution to the project in details. VERITAS adopted a full unbinned likelihood approach, as the one already described in Sec. 6.2.2. As discussed in Sec. 7.3, for the published VERITAS data, [185] did not perform a MLE study, but they used a different statistical method, called "event-weighting" method. The MLE code to generate the shared VERITAS data was slightly different from the code used to cross-check the limits presented in [185].

We shared the data by using specific structured; each table, given a channel and a dSph, contains the likelihood fit result (Eq. 8.1) per each cross-section in the range of σ between 10^{-18} and 10^{-28} $cm^3 s^{-1}$, and for the masses. In addition, I contributed to build one of the two softwares (gLike) which reads properly the input tables and combines the data, together with Dr. Kerszberg and Dr. Tjark.

8.5 Results and discussion

None of the five observatories detected any significant DM emission.

However, we did set upper-limits on the annihilation cross-section $\langle \sigma v \rangle$. We used the following test statistics TS:

$$\mathrm{TS} = -2 \ln \lambda(\langle \sigma v \rangle), \tag{8.8}$$

where $\lambda(\langle \sigma v \rangle)$ is defined in Eq. 8.1. We solved Eq. 8.8 $= 2.71/2$, where $2.71/2$ corresponds to a one-sided 95% confidence level[4]. As said, this is still a preliminary study, so only two channels are presented in here, i.e. $b\bar{b}$ and $\tau\tau$.

The containment bands of 68% and 95% were generated using 300 Poisson realizations of

[4]If we assume that the TS behaves like a χ^2 distribution with one degree of freedom.

the null hypothesis for each of the combined datasets. Then, we combined them in the same way as dSph observations are combined. The median and containment bands on the null hypothesis were extracted from the distribution of resulting limits on the null hypothesis. For H.E.S.S., MAGIC, VERITAS, and HAWC, these 300 realizations were derived from fast simulations of the OFF observations or, in the case of Fermi-LAT, from true observations of empty fields of view.

Fig. 8.5 shows the annihilation cross-section upper limits obtained by each single instrument, for the two channels, by using the $\mathcal{GS}$ set of J-factors. Also, it shows the combined limit within its 68% and 95% containment bands and we do expect to see it close to the median limit when no signal is detected. We do see a pretty good agreement with the null hypothesis for all channels, within 2σ, between the observed and expected limits (the latter one given by the median value).

We can see that for energies below 500 GeV Femi-LAT is the dominant part of the DM limits for both channels. For higher energies (i.e. from 500 GeV up to 10 TeV) Fermi-LAT dominates for the hadronic DM channel, and then above 10 TeV, the IACTs and HAWC are dominant. From 1 TeV up to 100 TeV both IACTs and HAWC mainly contribute DM limit.

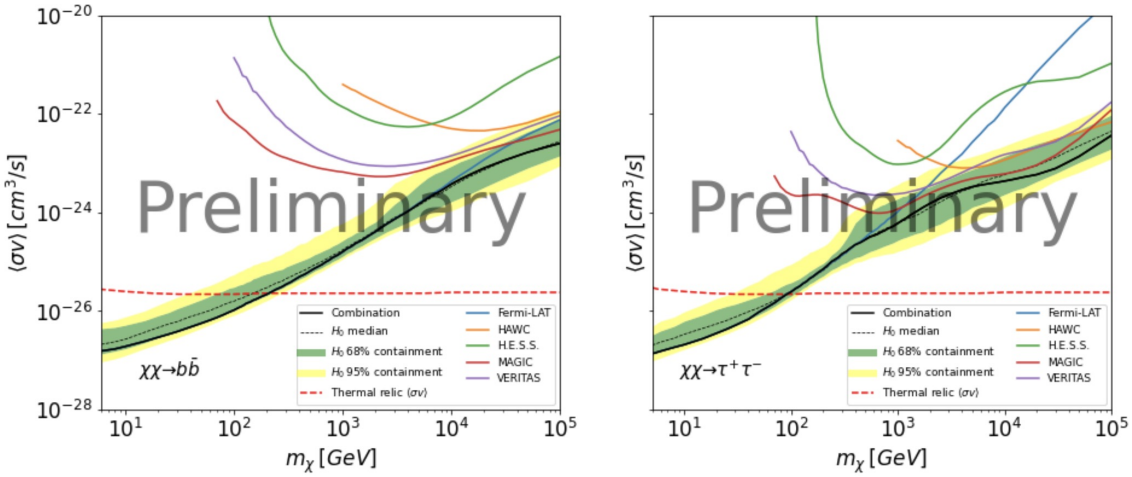

Figure 8.5: Preliminary cross-section upper limits for the two channels analysed here (on the left: $b\bar{b}$ and on the right: $\tau\tau$). This figure shows single upper limits from each instrument and also the combined limit.

It is also evident that the combined DM limits from all 5 experiments are 2-3 times stronger than the single telescope result. Surely, the choice of multiple targets did increase the statistics. It is also noticeable that the limits depend on the choice of the annihilation channel and the object with the highest J-factor leads up. Indeed the ultra-faint dSphs, can be hugely effected by systematic uncertainty for the determination of their J-factors.

8.6 Conclusions and future plans

In this work we combined data for 20 dSphs from five different experiments such as Fermi-LAT, HAWC, MAGIC, H.E.S.S. and VERITAS in order to set upper-limits on DM annihilation cross-section for two annihilation channels, i.e. $b\bar{b}$ and $\tau\tau$. The goal of this project was to boost the sensitivity to DM signal at lower and higher energies. We did not detect

DM signal so far, but we did put upper limits on the DM annihilation cross-section. As expected, Fermi-LAT dominates over the lower energies (below 1 TeV), while the IACTs dominate at intermediate energies and thanks to HAWC we got higher energies upper limits. Overall, the upper limits derived span over the widest mass range ever considered and the combined limit is 2-3 times stronger than any individual telescope. Furthermore, these results improved the sensitivity of previously published results from each detector. This is still a preliminary study, so more channels will be also included (i.e. W^+W^-, Z^+Z^-, $b\bar{b}$, $t\bar{t}$, e^+e^-, $\mu^+\mu^-$, $\tau^+\tau^-$ and mono-energetic $\gamma\gamma$ channel), and larger datasets would be essential to handle the DM search challenge.

Another interesting study would be using a different set of J-factors in order to estimate the impact of systematic uncertainties in the J-factor calculation. For example, the one from [140] has been already planned to be used. J-factors from [140] were, indeed, chosen because in their work a different (and more complete) study of the kinematic stellar data was performed, with respect to [171] work. [140] adopted the Einasto profile to describe the DM density, the Zhao-Hernquist profile [161] for the stellar distribution and a realistic anisotropy profile (i.e., the Baes & Van Hese profile [214]), which takes into account likely non-isotropic inner regions.

Also including other experiments such as LHAASO [215], CTA [92] and SWGO [216] would further boost the sensitivity. Moreover, including other data than γ rays (such as neutrinos) will be crucial. Actually, efforts in this context have already been started, adding data from IceCube and ANTARES observatories.

This combination method/technique could also be applied in fields other than DM-related fields.

Chapter 9

Conclusions

The goal of this work was to detect DM or, alternatively, to set constraints on DM properties by performing an "extended" (or "2D") analysis of four dSphs. To do so, we included the dSph angular extension information in the MLE analysis we carried out. We used good-quality data from 230 hour observations of four dSphs (i.e. Bootes, Draco, Segue1 and Ursa Minor) made by VERITAS from 2007 to 2013.

We first evaluated the effectiveness of 2D analysis, compared to the conventional spectral analysis ("1D"). We found that the suggested method would be more sensitive to detect a possible DM signal, and the analysis with an extended-source region would lead to improvement in finding and constraining DM properties, with an improvement factor of 20-30% (depending on the channel and source). In fact, the effectiveness of the 2D method does not depend on which dwarf is being considered but it can depend on the DM annihilation channel.

Next, we performed an unbinned 2D MLE, taking into account both energy and angular extension dependency in observed events and DM spectra, for two DM annihilation channels, $\tau\tau$ and $b\bar{b}$. As we did not detect any significant DM signal, we did set upper limits on

the DM annihilation cross-section. We compared these results with the ones obtained using only the energy information (1D analysis), in which cuts optimized for point-like sources were applied. We found out that, depending on the channel and on the mass, performing a 2D analysis of dSphs can lead to more constrained cross-section upper limits, with an average improvement of about 15%. However, we noticed that this was not always the case, may be due to the fact that we used different cuts (moderate NTel3 as opposite to soft NTel2) than the ones used in the 1D standard analysis. We also compared our extended results as well to the ones obtained/published by other experiments such as MAGIC and HAWC and to the previous VERITAS ones, which applied θ^2 cut optimized for a point-like source. In all cases, we got more constrained upper limits with respect to others' results. In addition, we studied the systematic uncertainty around the observed limits. This is mostly due to our poor knowledge on the DM density profile within dSphs.

We could definitely improve or constrain more on the DM properties with the following methods/technique. For example, more data can be added. In fact, more than 88 additional hrs of Ursa Minor data can be considered, taken from 2013 to 2020, as well as more than 48 hrs on Segue1 and 34 hrs on Draco. Moreover, other dSphs can also be analysed. VERITAS observed 15 more dSphs (other than the ones analysed in this work) between mid-2007 and mid-2017, for a total observation time of 368 hrs. The DM annihilation cross-section upper limits can be also combined in order to get even more constrained limits. In order to further boost the sensitivity it may be crucial to include data from other experiments as well.

Studying the impact of statistical uncertainties can be also explored; by performing a MLE assuming the background-only hypothesis, the expected limits can be calculated, just to check how consistent data are with the null hypothesis only.

We can further improve our results by optimizing IRFs. For example, each single dSphs may need a specific optimization using, e.g., BDT optimized precisely on it, or using different type of cuts, such as, for example, hard cuts rather than moderate, testing those with new (even looser) θ^2 cut values.

Another challenging improvement to apply would be to model the background distribution. As we saw, in fact, due to the limited background observation, the probability density function of background events is not continuous (for example some very-high-energy bins do not have any background events). It would be difficult then to assign the background likelihood to the events corresponding to those bins. To overcome this problem, it is possible to fit the low-energy background distributions with, e.g., a power law, and then extrapolated up to the highest energy we observed in all regions.

One more appealing change to do in the future in the analysis would be to perform the analysis using the open-source Python package for gamma-ray astronomy called "Gammapy" [1]. This one contains specific DM-oriented modules providing spatial and spectral models for indirect DM searches. A comparison with current results would be worth it too.

Results from a multi-instrument project I joined were presented here too. The goal of this project was to combine 20 dSph observational results from the Fermi-LAT, HAWC, H.E.S.S., MAGIC, and VERITAS collaborations. From the combined MLE analysis, the sensitivity of DM searches can be maximized and the current results can be improved as well. No DM signal was detected, however we derived more constraining upper limits on the WIMP DM self-annihilation cross-section as a function of DM particle mass, extending from 5 GeV to 100 TeV, thanks to the combination of these five different γ-ray instruments. As a matter of fact, this was the widest mass range ever considered for setting

[1] https://docs.gammapy.org/0.19/

DM constraints. We found 2-3 times constrained limits compared to those from any other single telescope. For future work, it may be definitely interesting to analyse more DM annihilation channels and to study the decay case as well. In addition, more dSphs could be included as well dSphs data from other experiments, such as LHAASO, CTA and SWGO.

Bibliography

[1] I. Ridpath. "A dictionary of Astronomy". In: *Oxford University Press* (2016).

[2] Lundmark K. "Über die Bestimmung der Entfernungen, Dimensionen, Massen und Dichtigkeit fur die nächstgelegenen anagalacktischen Sternsysteme". In: *Meddelande fran Lunds astronomiska Observatorium* (1930).

[3] Zwicky F. "The redshift of extragalactic nebulae". In: *Helv. Phys. Acta* (1933).

[4] F. Zwicky. "On the Masses of Nebulae and of Clusters of Nebulae". In: *Astrophysical Journal* (1937).

[5] E. L. Lokas and G. A. Mamon. "Dark matter distribution in the Coma cluster from galaxy kinematics: breaking the mass-anisotropy degeneracy". In: *Monthly Notices of the Royal Astronomical Society* (2003).

[6] N. A. Bahcall and X Fan. "The Most Massive Distant Clusters: Determining Ω and σ_8". In: *The Astrophysical Journal* (1998).

[7] Babcock H.W. "The rotation of the Andromeda Nebula". In: *Lick Observatory bulletin* (1939).

[8] M. S. Roberts. "M 31 and a Brief History of Dark Matter". In: *Frontiers of Astrophysics: A Celebration of NRAO's 50th Anniversary ASP Conference Series, Vol. 395, Proceedings of the conference held 18-21 June, 2007* (2008).

[9] C. Carignan et al. " Extended HI rotation curve and mass distribution of M31 ". In: *ApJ Letters* (2005).

[10] Rubin V. C., Ford W. K. Jr., and Thonnard N. "Rotational properties of 21 SC galaxies with a large range of luminosities and radii, from NGC 4605 (R=4kpc) to UGC 2885 (R=122kpc)". In: *Astrophysical Journal* (1980).

[11] Yoshiaki Sofue. "Rotation and mass in the Milky Way and spiral galaxies". In: *Publications of the Astronomical Society of Japan* (2016).

[12] T. S. van Albada et al. "Distribution of dark matter in the spiral galaxy NGC 3198". In: *Astrophys. J.* (1985).

[13] G. Bertone, D. Hooper, and J. Silk. " Particle Dark Matter: Evidence, Candidates and Constraints ". In: *Physics Reports* (2004).

[14] T. Kitching R. Massey and J. Richard. "The dark matter of gravitational lensing". In: *Rept. Prog. Phys.* (2010).

[15] J. Wambsganss, P. Schneider, and C. Kochanek. "Distribution of dark matter in the spiral galaxy NGC 3198". In: *Springer Science & Business Media* (2006).

[16] Mao S. "Astrophysical applications of gravitational microlensing". In: *Astron. Astrophys* (2012).

[17] Chwolson O. "Uber eine mogliche Form fiktiver Doppelsterne". In: *Astronomische Nachrichten* (1924).

[18] L. Wang et al. "SDSS J1640+1932: a spectacular galaxy-quasar strong lens system". In: *MNRAS* (2017).

[19] N. Kaiser and G. Squires. "Mapping the Dark Matter with Weak Gravitational Lensing ". In: *Astrophysical Journal* (1993).

[20] Clowe D., Gonzalez A. H., and Markevitch M. "Weak-Lensing Mass Reconstruction of the Interacting Cluster 1E 0657-558: Direct Evidence for the Existence of Dark Matter". In: *The Astrophysical Journal* (2004).

[21] K. Garrett and J. Duda. "Dark Matter: A Primer". In: *Adv. Astron.* (2011).

[22] M. Milgrom. " A Modification of the Newtonian dynamics as a possible alternative to the hidden mass hypothesis". In: *Astrophys. J* (1983).

[23] A. Einstein. "Die Grundlage der allgemeinen Relativitatstheorie". In: *Annalen der Physik* (1916).

[24] M. Lachieze-Rey and J.P. Luminet. "Cosmic topology". In: *Phys. Rept.* (1996).

[25] E. Hubble. "A relation between distance and radial velocity among extra-galactic nebulae". In: *Proc Natl Acad Sci USA* (1929).

[26] A. Friedman. "Uber die Krummung des Raumes". In: *Z. Phys.* (1922).

[27] C. Contaldi, H. Hoekstra, and A. Lewis. "Joint CMB and Weak Lensing Analysis; Physically Motivated Constraints on Cosmological Parameters". In: *Phys. Rev. Lett.* (2003).

[28] S. Weinberg. "The cosmological constant problem". In: *Rev. Mod. Phys.* (1989).

[29] Gamow G. " Expanding Universe and the Origin of Elements". In: *Physical Review* (1946a).

[30] A. Penzias and R. W. Wilson. " A Measurement of Excess Antenna Temperature at 4080 Mc/s". In: *Astrophysical Journal* (1965).

[31] P. J. E. Peebles. " Penzias and Wilson's Discovery of the Cosmic Microwave Background". In: *Astrophysical Journal* (1999).

[32] G. F. Smoot et al. "Structure in the COBE differential microwave radiometer first-year maps". In: *Astrophysical Journal* (1992).

[33] N. Aghanim et al. " Planck 2018 results. VI. Cosmological parameters". In: *A&A* (2019).

[34] J. A. Vazquez, L. Padilla, and T. Matos. "Inflationary Cosmology: From Theory to Observations". In: (2018).

[35] J. Silk and H. Bloemen. " A gamma-ray constraint on the nature of dark matter". In: *The Astrophysical Journal* (1987).

[36] A. Coc and E. Vangioni. "Primordial nucleosynthesis". In: *Int. J. Mod. Phys.* (2017).

[37] Cyburt R. H. et al. "Big Bang Nucleosynthesis: 2015". In: *Rev. Mod. Phys.* (2016).

[38] B. D. Fields. "The Primordial Lithium Problem". In: *Ann. Rev. of Nuclear and Particle Science* (2012).

[39] S. Sarkar. "Measuring the baryon content of the universe: BBN vs CMB". In: *Proceedings, XIIIth Rencontres de Blois on Frontiers of the Universe: Blois, France, June 17-23, 2001* (2001).

[40] E. O. Zavarygin and A. V. Ivanchik. "The variation of the baryon-to-photon ratio during different cosmological epochs due to decay and annihilation of dark matter". In: *Journal of Physics* (2015).

[41] G. German. "Evolution of the universe during the inflationary epoch". In: (2020).

[42] Fixsen D. J. "The Temperature of the Cosmic Microwave Background". In: *The Astrophysical Journal* (2009).

[43] R.H. Dicke. "Gravitation and the Universe: Jayne Lectures for 1969". In: *American Philosophical Society* (1970).

[44] Remmen G. N. and Carroll S. M. "How many e-folds should we expect from high-scale inflation?" In: *Phys. Rev. D* (2014).

[45] D. G. York et al. " The Sloan Digital Sky Survey: Technical Summary". In: *Astron. J.* (2000).

[46] V. Springel et al. " Simulations of the formation, evolution and clustering of galaxies and quasars". In: *Nature* (2005).

[47] Volker Springel, Carlos S. Frenk, and Simon D. M White. "The largescale structure of the Universe". In: *Nature* (2006).

[48] Audren B. et al. "Strongest model-independent bound on the lifetime of Dark Matter". In: *Journal of Cosmology and Astroparticle Physics* 1412 (2014), p. 028.

[49] N. Park et al. "Performance of the VERITAS experiment. In 34th International Cosmic Ray Conference (ICRC2015)". In: *volume 34 of International Cosmic Ray Conference* (2015).

[50] Y. B. Zel'dovich and I. D. Novikov. " The Hypothesis of Cores Retarded during Expansion and the Hot Cosmological Model". In: *Soviet Astronomy* (1966).

[51] D. P. Bennett et al. " The MACHO project dark matter search". In: *ASP Conf. Ser.* (1996).

[52] P. Tisserand et al. " Limits on the MACHO content of the Galactic Halo from the EROS-2 Survey of the Magellanic Clouds". In: *Astronomy and Astrophysics* (2007).

[53] C. Alcock et al. "The MACHO project: microlensing results from 5.7 years of large magellanic cloud observations". In: *The Astrophysical Journal* (2000).

[54] E. W. Kolb. "Inner space/outer space - The interface between cosmology and particle physics". In: *University of Chicago Press* (1986).

[55] R. N. Mohapatra et al. "Theory of neutrinos: A White paper". In: *Rept. Prog. Phys.* (2007).

[56] S. Dodelson and L. M. Widrow. "Sterile Neutrinos as Dark Matter". In: *Phys.Rev.Lett* (1994).

[57] R. D. Peccei. "The Strong CP Problem and Axions". In: *Lect.Notes Phys.* (2008).

[58] R. Essig et al. "Working Group Report: New Light Weakly Coupled Particles". In: *Proceedings, 2013 Community Summer Study on the Future of U.S. Particle Physics: Snowmass on the Mississippi (CSS2013): Minneapolis* (2013).

[59] L. F. Abbott and P. Sikivie. "A cosmological bound on the invisible axion". In: *Physics Letters B* (1983).

[60] D. J. E. Marsh. "Axion Cosmology". In: *Physics Reports* (2015).

[61] F. Chadha-Day, J. Ellis, and D. J. E. Marsh. "Axion Dark Matter: What is it and Why Now?" In: (2021).

[62] M. Kamionkowski. "WIMP and Axion Dark Matter". In: *High Energy Physics and Cosmology* (1997).

[63] K. Griest. "The Search for the Dark Matter: WIMPs and MACHOs". In: *Annals of the New York Academy of Sciences* (1993).

[64] R. Catena and L. Covi. "SUSY dark matter(s)". In: *EPJ* (2013).

[65] B. W. L. and S. Weinberg. "Cosmological Lower Bound on Heavy-Neutrino Masses". In: *Phys. Rev. Lett.* (1977).

[66] M. Cannoni. "Exact theory of freeze-out". In: *The European Physical Journal C* (2015).

[67] G. Steigman, B. Dasgupta, and J. F. Beacom. "Precise Relic WIMP Abundance and its Impact on Searches for Dark Matter Annihilation". In: *Phys.Rev.* (2012).

[68] K. Ala-Mattinen and K. Kainulainen. "Precision calculations of dark matter relic abundance". In: *JCAP* (2020).

[69] T. M. Undagoitia and L. Rauch. "Dark matter direct-detection experiments". In: *J. Phys.* (2017).

[70] S. Moriyama. "Direct Detection of Dark Matter". In: *ASP Conference Series* (2012).

[71] M. Tanabashi et al. "Review of Particle Physics". In: *Phys. Rev.* (2018).

[72] R. Bernabei et al. "First model independent results from DAMA/LIBRA-phase2". In: *Nucl. Phys. At. Energy* (2018).

[73] R. Bernabei et al. "The DAMA/LIBRA apparatus". In: *Nuclear Instruments and Methods in Physics Research Section A* (2008).

[74] Aprile E. et al. " XENON100 Dark Matter Results from a Combination of 477 Live Days". In: *Physical Review* (2016).

[75] C. Boehm et al. "How high is the neutrino floor?" In: *JCAP* (2019).

[76] P. Fox et al. "Missing Energy Signatures of Dark Matter at the LHC". In: *Phys. Rev* (2012).

[77] J. Abdallah et al. "Simplified Models for Dark Matter Searches at the LHC". In: *Phys. Dark Univ* (2015).

[78] P. J. Fox et al. "LEP Shines Light on Dark Matter". In: *Phys.Rev.D* (2011).

[79] D. Abercrombie et al. "Dark Matter Benchmark Models for Early LHC Run-2 Searches: Report of the ATLAS/CMS Dark Matter Forum". In: *Phys. Dark Univ.* (2015).

[80] A. Boveia and C. Doglioni. "Dark Matter Searches at Colliders". In: *Ann. Rev. Nucl. Part. Sci* (2018).

[81] A. Bouquet and P. Salati. "Dark matter and the suppression of stellar core convection". In: *Astrophysical Journal* (1989).

[82] G. Jungman, M. Kamionkowski, and K. Griest. "Supersymmetric Dark Matter". In: *Phys.Rept.* (1996).

[83] N.P. Topchiev et al. "High-energy gamma-ray studying with GAMMA-400". In: *In 35th International Cosmic Ray Conference (ICRC2017), Bexco, Busan, Korea* (2017).

[84] S. Profumo and P. Ullio. "Multi-wavelength Searches for Particle Dark Matter". In: *Chapter 27 of Particle Dark Matter: Observations, Models and Searches* (2010).

[85] R. Barbieri. "Electroweak Corrections". In: *contribution to The Standard Theory up to the Higgs discovery - 60 years of CERN* (2015).

[86] O.J. Arranz. "The role of the Sommerfeld enhancement in dark matter physics". In: (2018).

[87] T. R. Slatyer. "The Sommerfeld enhancement for dark matter with an excited state". In: *JCAP* (2009).

[88] M. Lattanzi and J. Silk. "Can the WIMP annihilation boost factor be boosted by the Sommerfeld enhancement?" In: *Phys.Rev.D* (2009).

[89] O. Newton et al. "The total satellite population of the Milky Way". In: *Mon. Not. Roy. Astron. Soc.* (2018).

[90] Jonathan R. Hargis, Beth Willman, and Annika H. G. Peter. "Too many, too few or just right? The predicted number and distribution of Milky Way Dwarf Galaxies". In: *The American Astronomical Society* (2014).

[91] T. E. Jeltema et al. " Gamma Rays from Clusters and Groups of Galaxies: Cosmic Rays versus Dark Matter". In: . *Phys. Rev.* (2009).

[92] J. Knodlseder. "The Cherenkov Telescope Array". In: *Proceedings of Theory meeting experiments (TMEX 2020) 16th Rencontres du Vietnam* (2020).

[93] Heaviside O. " Electromagnetic waves, the propagation of potential, and the electromagneteic effects of a moving charge". In: *The Electrician* (1888).

[94] Cherenkov P.A. " Visible emission of clean liquids by action of gamma radiation". In: *Doklady Akademil Mauk* (1934).

[95] Jelley J. V. " Cerenkov Radiation and Its Applications". In: *London: Pergamon Press* (1958).

[96] "How a particle racing through a vacuum leaves a trail of blue light". In: *Nature* (2019).

[97] Huygens C. "Traité de la Lumière". In: *Leyden by Van der Aa* (1690).

[98] E.A. Fuste. "VHE γ-ray observations of Northern sky pulsar wind nebulae with the MAGIC Telescope". In: *PhD thesis, Universitat Autnonoma de Barcelona* (2007).

[99] Sengupta P. " Classical electrodynamics". In: *New Delhi: New Age International* (2000).

[100] J. Jackson. " Classical Electrodynamics". In: *John Wiley & Sons* (1999).

[101] P. Blasi. "The Origin of Galactic Cosmic Rays". In: *A&A Reviews* (2013).

[102] A. A. Watson. "The discovery of Cherenkov radiation and its use in the detection of extensive air showers ". In: *Proceedings of CRIS2010: Cosmic Ray International Seminar on 100 years of Cosmic Rays: from Pioneering Experiments to Physics in Space* (2010).

[103] J.D. Haverhoek. "Ultra High Energy Cosmic Ray Extensive Air Shower simulations using CORSIKA". In: (2006).

[104] F. Schmidt and J. Knapp. "CORSIKA Shower Images". In: *https://www-zeuthen.desy.de/ jknapp/fs/showerimages.html* (2005).

[105] Landau L. and Rumer G. "The Cascade Theory of Electronic Showers". In: *Proceedings of the Royal Society A: Mathematical, Physical and Engineering Sciences* (1938).

[106] W. Heitler. "Quantum theory of radiation". In: *Nature* (1954).

[107] A. M. Hillas. "Cerenkov light images of EAS produced by primary gamma," in: *Proceedings from the 19th ICRC* (1985).

[108] F. Aharonian et al. "High energy astrophysics with ground-based gamma ray detectors". In: *Reports on Progress in Physics* (2008).

[109] Hillas A. M. "Differences between Gamma-Ray and Hadronic Showers". In: *Space Science Reviews* (1996).

[110] A. McCann et al. "A new mirror alignment system for the VERITAS telescopes". In: *Astroparticle Physics* (2010).

[111] Hansen P. M., Alvarez-Muniz J., and Vazquez R. A. "A comprehensive study of shower to shower fluctuations". In: *Astroparticle Physics* (2011).

[112] D. et al. Heck. " CORSIKA: a Monte Carlo code to simulate extensive air showers". In: *Forschungszentrum Karlsruhe Report FZKA* (1998).

[113] "ASTRI-Horn is first Cherenkov telescope in dual-mirror configuration to detect the Crab Nebula at TeV energies". In: *Press Release* (2019).

[114] Leinert C. et al. "The 1997 reference of diffuse night sky brightness". In: *Astron. Astrophys. Suppl. Ser.* (1998).

[115] J. et Holder. "The first VERITAS telescope". In: *Astroparticle Physics* (2006).

[116] J. M Davies and E. S Cotton. "Design of the quartermaster solar furnance". In: *J. Solar Energy* (1957).

[117] E. et al Roache. "Mirror Facets for the VERITAS Telescopes". In: *In Proc 30th ICRC* (2007).

[118] E. Gazda et al. "Photon Detection Efficiency Measurements of the VERITAS Cherenkov Telescope Photomultipliers after four Years of Operation". In: *Journal of Instrumentation* (2016).

[119] T. Nagai. " Focal Plane Instrumentation of VERITAS," in: *Proceedings from the 30th ICRC* (2007).

[120] A. Weinstein. " The VERITAS Trigger System". In: *In Proc 30th ICRC* (2007).

[121] J. et al. Hall. " Veritas CFDs". In: *Proceedings from the 28th ICRC* (2003).

[122] E. Hays. " VERITAS Data Acquisition". In: *in Proc 30th ICRC* (2007).

[123] P. F. Rebillot et al. " The VERITAS Flash ADC Electronics System". In: *in Proc 28th ICRC* (2003).

[124] Hanna et al. "An LED-based flasher system for VERITAS". In: *Nuclear Instruments and Methods in Physics Research* (2010).

[125] V. P. et al. Fomin. " New methods of atmospheric Cherenkov imaging for gamma-ray astronomy. I. The false source method". In: *Astroparticle Physics* (1994).

[126] G. Maier. "Description and application of a simple image fitting method". In: *Internal VERITAS note* (2010).

[127] J. Holder. " Exploiting VERITAS Timing Information". In: *Proceedings from the 29th ICRC* (2005).

[128] D. J. Fegan. "γ/hadron separation at TeV energies," in: *Journal of Physics G Nuclear Physics* (1997).

[129] W. et al. Hofmann. "Comparison of techniques to reconstruct VHE gamma-ray showers from multiple stereoscopic Cherenkov images". In: *Astroparticle Physics* (1999).

[130] Kohnle et al. "Stereoscopic imaging of air showers with the first two HEGRA Cherenkov telescopes". In: *Astroparticle Physics* (1996).

[131] F. A. Aharonian et al. "The potential of ground based arrays of imaging atmospheric Cherenkov telescopes. I. Determination of shower parameters". In: *Astroparticle Physics* (1997).

[132] M. Krause, E. Pueschel, and G. Maier. "Improved γ/hadron separation for the detection of faint γ-ray sources using boosted decision trees". In: *Astroparticle Physics* (2017).

[133] D. Berge, S. Funk, and J. Hinton. "Background modelling in very-high-energy γ-ray astronomy". In: *A&A* (2007).

[134] T.-P. Li and Y.-Q. Ma. "Analysis methods for results in gamma-ray astronomy, " in: *The Astrophysical Journal* (1983).

[135] K. Bechtol et al. "Eight New Milky Way Companions Discovered in First-Year Dark Energy Survey Data". In: *Astrophys. J* (2015).

[136] B. Flaugher et al. In: *International Journal of Modern Physics* (2005).

[137] J. Coronado-Blazquez and M.A. Sanchez-Conde. "Constraints to Dark Matter Annihilation from High-Latitude HAWC Unidentified Sources". In: *Galaxies* (2020).

[138] M. L. Ahnen et al. "Limits to dark matter annihilation cross-section from a combined analysis of MAGIC and Fermi-LAT observations of dwarf satellite galaxies". In: *JCAP* (2016).

[139] & Walker M. G. Mateo M. Olszewski E. W. "The Velocity Dispersion Profile of the Remote Dwarf Spheroidal Galaxy Leo I: A Tidal Hit and Run?" In: *The Astrophysical Journal* (2008).

[140] Bonnivard et al. "Spherical Jeans analysis for dark matter indirect detection in dwarf spheroidal galaxies – impact of physical parameters and triaxiality". In: *MNRAS* (2015).

[141] M. Cirelli. "Indirect searches for dark matter: a status review". In: *Pramana* (2012).

[142] A. Chatterjee and D. Das. "Right Sneutrino Dark Matter and a Monochromatic Photon Line". In: *RECAPP-HRI* (2014).

[143] Sekiguchi M. and Fukugita M. " A Study of the B-V Color-Temperature Relation". In: *The Astronomical Journal* (2000).

[144] E. Hertzsprung. " Uber die Verwendung Photographischer Effektiver Wellenlaengen zur Bestimmung von Farbenaequivalenten". In: *Publikationen des Astrophysikalischen Observatoriums zu Potsdam* (1911).

[145] E. R. Stanway and J. J. Eldridge. "Reevaluating Old Stellar Populations". In: *MNRAS* (2018).

[146] J. D. Simon et al. "Stellar kinematics and metallicities in the ultra-faint dwarf galaxy Reticulum II". In: *The Astrophysical Journal* (2015).

[147] M. G. Walker et al. "A Universal Mass Profile for Dwarf Spheroidal Galaxies". In: *Astrophys. J.* (2009).

[148] L.E. Strigari. " Dark Matter in Dwarf Spheroidal Galaxies and Indirect Detection: A Review". In: *Rept. Prog. Phys* (2018).

[149] M. Y. Wang et al. "Tidal features of classical Milky Way satellites in a ΛCDM Universe". In: *MNRAS* (2017).

[150] F. Ferrer and D. R. Hunter. " The impact of the phase-space density on the indirect detection of dark matter". In: *JCAP* (2013).

[151] L. E. Strigari, C. S. Frenk, and S. D. M. White. " Kinematics of Milky Way Satellites in a Lambda Cold Dark Matter Universe". In: *MNRAS* (2010).

[152] S. Binney J. & Tremaine. "Galactic Dynamics: Second Edition". In: *Princeton University Press* (2008).

[153] R. P. Van der Marel. In: *MNRAS* (1994).

[154] H.C. Plummer. "On the problem of Distribution in Globular Star Clusters". In: *MNRAS* (1911).

[155] G. A. Mamon, E. L. Lokas, and T. Sanchis. "Breaking the mass/anisotropy degeneracy in the Coma cluster". In: *Proceedings IAU Colloquium* (2004).

[156] H. Dejonghe and D. Merritt. "Inferring the mass of spherical stellar systems from velocity moments". In: *The Astrophysical Journal* (1992).

[157] Merrifield M. R. and Kent S. M. "Fourth moments and the dynamics of spherical systems". In: *Astronomical Journal* (1990).

[158] F. I. Diakogiannis, G. F. Lewis, and R. A. Ibata. "Resolving the mass–anisotropy degeneracy of the spherically symmetric Jeans equation I: theoretical foundation". In: *MNRAS* (2021).

[159] M. Schwarzschild. " A numerical model for a triaxial stellar system in dynamical equilibrium". In: *Astrophys J.,* (1979).

[160] J. R. Jardel et al. "Measuring Dark Matter Profiles Non-Parametrically in Dwarf Spheroidals: An Application to Draco". In: *Astrophys. J* (2013).

[161] H. Zhao. "Analytical models for galactic nuclei ". In: *MNRAS* (1996).

[162] L. Hernquist. "An analytical model for spherical galaxies and bulges". In: *The astrophysical journal* (1990).

[163] A. Schuster. "Report of the 53rd meeting of the British Association for the Advancement of Science (Southport, 1883)". In: (1884).

[164] W. Jaffe. "A simple model for the distribution of light in spherical galaxies". In: *MNRAS* (1983).

[165] C. S. Frenk and S. D. M. White. "Dark matter and cosmic structure". In: *Ann. Phys.* (2012).

[166] B. Moore et al. " Cold collapse and the core catastrophe". In: *MNRAS* (1999).

[167] J. Einasto. "On the Construction of a Composite Model for the Galaxy and on the Determination of the System of Galactic Parameters". In: *Trudy Inst. Astrofiz. Alma-A* (1965).

[168] Gao L. et al. "The redshift dependence of the structure of massive Λ cold dark matter haloes". In: *MNRAS* (2008).

[169] A. Kassiola and I. Kovner. "Elliptic mass distributions versus elliptic potentials in gravitational lenses". In: *Astrophys. J* (1993).

[170] A. Burkert. " The structure of Dark Matter Haloes in Dwarf Galaxies". In: *Astrophys J.* (1995).

[171] Geringer-Sameth A., Koushiappas S.M., and Walker M. "Dwarf galaxy annihilation and decay emission profiles for dark matter experiments". In: (2015).

[172] N. W. Evans, J. An, and M. G. Walker. "Cores and cusps in the dwarf spheroidals". In: *MNRAS* (2009).

[173] V. Bonnivard et al. "Dark matter annihilation and decay in dwarf spheroidal galaxies: The classical and ultrafaint dSphs". In: *MNRAS* (2015).

[174] S. Von Hoerner. "The internal structure of globular clusters". In: *The Astrophysical Journal* (1957).

[175] I. King. "The structure of Star clusters. I. An Empirical Density Law". In: *The astronomical Journal* (1962).

[176] P. Mollitor, E. Nezri, and R. Teyssier. "Baryonic and dark matter distribution in cosmological simulations of spiral galaxies". In: *MNRAS* (2015).

[177] R. den Hartog and P. Katgert. "On the dynamics of the cores of galaxy clusters". In: *MNRAS* (1996).

[178] M. G. Walker and J. Penarrubia. "A method for measuring (slopes of) the mass profiles of dwarf Spheroidal galaxies". In: *The Astrophysical Journal* (2011).

[179] K. Hayashi et al. "Tidal stripping and the structure of dwarf galaxies in the Local Group". In: *MNRAS* (2016).

[180] A. Pontzen et al. " Milking the spherical cow on aspherical dynamics in spherical coordinates". In: *MNRAS* (2015).

[181] D. J. R. Campbell et al. " Knowing the unknowns: uncertainties in simple estimators of galactic dynamical masses". In: *MNRAS* (2016).

[182] M. Irwin and D. Hatzidimitriou. "Structural parameters for the Galactic dwarf spheroidals". In: *MNRAS* (1995).

[183] J. Bailin and M. Steinmetz. "Internal and external alignment of the shapes and angular momenta of ΛCDM halos". In: *Astrophysical Journal* (2005).

[184] L. E. Strigari. "Galactic Searches for Dark Matter". In: *Physics Reports* (2012).

[185] Archambault S. et al. "Dark Matter Constraints from a Joint Analysis of Dwarf Spheroidal Galaxy Observations with VERITAS". In: *Physical Review* (2017).

[186] F. Calore, P. D. Serpico, and B. Zaldivar. "Dark matter constraints from dwarf galaxies: a data-driven analysis". In: *JCAP* (2018).

[187] P. Cogan. "VEGAS, the VERITAS Gamma-ray Analysis Suite". In: *30th International Cosmic Ray Conference, Merida, Mexico* (2007).

[188] Cramer H. "Mathematical Methods of Statistics". In: *Princeton University Press* (1946).

[189] James F. "Minuit: Reference Manual". In: *CERN, Geneva* (1994).

[190] Cowan G. et al. "Asymptotic formulae for likelihood-based tests of new physics". In: *Eur. Phys. J.,* (2013).

[191] C. Armand. "Dark matter searches in the direction of dwarf galaxies with H.E.S.S. and characterization of the γ-ray emission from the Galactic center and Andromeda galaxy with Fermi-LAT". In: *PhD Thesis LAPP LAPTh Annecy* (2020).

[192] Lamorte W.W. "Hypothesis Testing: Upper-, Lower, and Two Tailed Tests, Boston University School of Public Health". In: (2017).

[193] Cowan G. "Statistical Data Analysis". In: *Oxford Science Publications* (1997).

[194] J. et al. Aleksic. "Optimized dark matter searches in deep observations of Segue 1 with MAGIC". In: *JCAP* (2014).

[195] J. Aleksic, J. Rico, and M. Martinez. "Optimized analysis method for indirect dark matter searches with Imaging Air Cherenkov Telescopes". In: *JCAP* (2012).

[196] W. A. Rolke, A. M. lopez, and J. Conrad. "Limits and Confidence Intervals in the Presence of Nuisance Parameters". In: *Nucl.Instrum.Meth* (2005).

[197] T.-P. Li and Y.-Q. Ma. "Analysis methods for results in gamma-ray astronomy". In: *The Astrophysical Journal* (1983).

[198] T. Sjostrand, S. Mrenna, and P.Z. Skands. In: *Comput. Phys. Commun.* (2008).

[199] W. A. Rolke, A. M. lopez, and J. Conrad. In: *JHEP* (2010).

[200] S. E. Koposov et al. "Accurate stellar kinematics at faint magnitudes: application to the Bootes I dwarf spheroidal galaxy". In: *The Astrophysical Journal* (2011).

[201] A. Albert et al. "Dark Matter limits from Dwarf Spheroidal Galaxies with the HAWC gamma-ray observatory". In: (2017).

[202] J. Aleksic, J. Rico, and M. Martinez. "Optimized analysis method for indirect dark matter searches with imaging air Cherenkov Telescopes". In: *JCAP* (2012).

[203] A. Geringer-Sameth, S. M. Koushiappas, and M. G. Walker. "A Comprehensive Search for Dark Matter Annihilation in Dwarf Galaxies". In: *Physical review D* (2014).

[204] M. et al. Ackermann. " The Fermi Large Area Telescope On Orbit: Event Classification, Instrument Response Functions, and Calibration". In: *Astrophys. J. Suppl.* (2012).

[205] M. et al. Ackermann. "Searching for Dark Matter Annihilation from Milky Way Dwarf Spheroidal Galaxies with Six Years of Fermi Large Area Telescope Data". In: *Phys. Rev. Lett.* (2015).

[206] S. et al. Abdollahi. "Fermi Large Area Telescope Fourth Source Catalog". In: *Astrophys. J. Suppl.* (2020).

[207] A. et al. Albert. "Searching for Dark Matter Annihilation in Recently Discovered Milky Way Satellites with Fermi-LAT". In: *Astrophys. J.* (2017).

[208] M. de Naurois and L. Rolland. "A high performance likelihood reconstruction of gamma-rays for Imaging Atmospheric Cherenkov Telescopes". In: *Astropart. Phys.* (2009).

[209] R. D. Parsons and J. A. Hinton. "A Monte Carlo Template based analysis for Air-Cherenkov Arrays". In: *Astropart. Phys.* (2014).

[210] Zanin R. "MARS, the MAGIC analysis and reconstruction software". In: *in Proceedings, 33rd International Cosmic Ray Conference (ICRC2013): Rio de Janeiro, Brazil, July 2-9, 2013* (2013).

[211] R. Alfaro et al. "All-particle cosmic ray energy spectrum measured by the HAWC experiment from 10 to 500 TeV". In: *Phys. Rev. D.* (2017).

[212] J. Rico et al. "gLike: numerical maximization of heterogeneous joint likelihood functions of a common free parameter plus nuisance parameters". In: (2021).

[213] T. Miener and D. Nieto. "LklCom: Combining likelihoods from different experiments". In: (2021).

[214] M. Baes and Van Hese E. "Search for gamma-ray spectral lines from dark matter annihilation in dwarf galaxies with the High-Altitude Water Cherenkov observatory". In: *Astron. Astrophys* (2007).

[215] G. Di Sciascio. "The LHAASO experiment: from Gamma-Ray Astronomy to Cosmic Rays". In: *Nuclear Physics B Proceedings Supplement 00* (2019).

[216] U. B. de Almeida. "The Southern Wide-Field Gamma-ray Observatory (SWGO)". In: *Proceedings of the IWARA 2020 Virtual Conference, September 2020* (2020).